INTERNATIONAL ATOMIC ENERGY AGENCY
UNITED NATIONS EDUCATIONAL, SCIENTIFIC AND CULTURAL ORGANIZATION

INTERNATIONAL CENTRE FOR THEORETICAL PHYSICS
34100 TRIESTE (ITALY) - P.O.B. 586 - MIRAMARE - STRADA COSTIERA 11 - TELEPHONE: 2240-1
CABLE: CENTRATOM - TELEX 460392 - I

H4.SMR/381 - 35

COLLEGE ON ATOMIC AND MOLECULAR PHYSICS: PHOTON ASSISTED COLLISIONS IN ATOMS AND MOLECULES

(30 January - 24 February 1989)

MOLECULAR DYNAMICS

S.A. RICE

The James Franck Institute
The University of Chicago
Chicago, Illinois
U.S.A.

Picosecond CARS as a probe of ground electronic state intramolecular vibrational redistribution

David J. Tannor, Stuart A. Rice, and Peter M. Weber
Department of Chemistry and The James Franck Institute, The University of Chicago, Chicago, Illinois 60637

(Received 3 July 1985; accepted 4 September 1985)

We describe a representation of coherent anti-Stokes Raman spectroscopy (CARS) suitable to the description of time-dependent measurements. This representation includes the standard energy frame formulation as a special case when cw fields are involved. The traditional CARS cw field frequency matching condition $\omega_0 = \omega_1 - \omega_2 + \omega_3$ must be generalized for non-cw fields; in that case it refers to the Fourier component at ω_0 of the convolution of the radiation field with the wave packet recurrences. The influence of resonance, both in the ground and electronically excited states, on the decay of time delayed CARS signals is discussed. As expected, intramolecular vibrational redistribution on the ground state potential surface of a molecule causes the CARS signal to decay in time. Model calculations show that quantum beats in the CARS signal may be observed, reflecting either a small number of coupled states (strong and regular recurrences) or sequential coupling of states (weak and early recurrences).

I. INTRODUCTION

Coherent anti-Stokes Raman spectroscopy (CARS) has proved to be an exceedingly useful probe in many studies of molecular properties. The technique is characterized by intense signals, high resolution, and excellent discrimination against sample fluorescence. These properties have made CARS extremely useful for high resolution spectroscopy, combustion diagnostics, and the spectroscopy of absorbing and/or fluorescing compounds. In addition, CARS has high sensitivity and high temporal resolution. As a result, CARS is of considerable use in time-resolved spectroscopy.[1-15] Applications to date include studies of vibrational dephasing times in solution,[6] of collisional relaxation times,[13] of properties of excited electronic states,[9-11] and the identification and measurement of vibrational and rotational populations in nascent molecular fragments.[4,5] In this article we provide a theoretical description of time-resolved CARS, with emphasis on the application of CARS to the study of intramolecular vibrational redistribution (IVR) on ground state Born–Oppenheimer potential surfaces.

The CARS process involves four photons. Typically, two laser beams are employed, with frequencies ω_1 and ω_2, whose frequency difference is resonant with a vibrational transition of the ground electronic state. Photon 3 is generally of the same frequency as photon 1; photon 4 is emitted spontaneously with a frequency equal to $\omega_1 - \omega_2 + \omega_3 = 2\omega_1 - \omega_2$, i.e., such that the molecule returns to its ground vibrational state. The key to the usefulness of CARS is that, if certain momentum and energy phase-matching conditions are satisfied, the fourth photon in the process is emitted coherently. Because the signal beam is generated by a coherent mixing of three photons it is extremely intense, often several orders of magnitude greater than spontaneous Raman signals. Furthermore, the signal beam is spatially oriented in the direction of the incident beams, whereas spontaneous Raman emission is distributed over 4π solid angle.

In this paper we are interested in the case when the frequency difference $\omega_1 - \omega_2$ is resonant with a "zeroth order" state, i.e., a nonstationary state of the molecule. Examples of such states are the nominal C–H stretch overtones of benzene[16,17] and the fundamental of the ring breathing mode (vibration 12) of the alkylbenzenes.[18] Under low resolution conditions transitions to these vibrational states look like single lines. At higher resolution these "lines" are seen to consist of a tightly clustered set of transitions to molecular eigenstates. In this paper we are dealing specifically with the case where this cluster of molecular eigenstates is excited coherently; it will then evolve via intramolecular vibrational redistribution processes which transfer amplitude of excitation from one part of the molecule to another. The time scale for this evolution, and the possible existence of quantum beats, or recurrences in the vibrational energy distribution, depend both on the particular molecule and the energy range studied.

There is an important connection between the methods used in recent studies of IVR rates in large molecules and the coherence condition on the CARS signal. Smalley and coworkers,[19] and Levy and co-workers,[20] have monitored the disappearance of the Rayleigh line (and resonance fluorescence in general) as a function of mode excited in their studies of the dispersed fluorescence spectra of large molecules. The driving force for this disappearance is intramolecular energy transfer from the initially excited part of the molecule to the rest of the molecule ("the bath"). Smalley's measurement can be thought of as two photon experiments carried out in the frequency domain. However, the same intramolecular energy transfer is characterized in the time domain by a decay in the CARS signal. The coherence condition for the CARS process, which implies generation of a macroscopic third order polarization, is that emission take place to the initial vibrational state. As energy is transferred from the initially excited part of the molecule to an effectively infinite intramolecular bath, the initial vibrational state can no longer be accessed and the CARS signal decays irreversibly.

The conventional formulations of the CARS process involve either energy domain expressions,[15,21,22] or Maxwell's equations taken together with the Bloch relaxation equations.[6,7] Neither of these formulations is fully suited to the description of time-domain CARS experiments as a probe of IVR. It is the purpose of this paper to provide an expression for the CARS intensity that takes account of the general time dependence of the photon field and highlights the time dependence of the intramolecular dynamics; we examine this expression for a variety of resonance conditions.

First, we examine the time dependence of the CARS signal as the frequency difference $\omega_1 - \omega_2$ is detuned from a vibrational transition. The CARS signal is seen to decay faster as the detuning is increased, in agreement with the time-energy uncertainty principle. This important conclusion has been reached previously, using a very different formalism, by Zinth *et al.* and by Kamga and Sceats, in connection with their studies of the suppression of nonresonant background noise.

Second, we examine resonance CARS, i.e., when the first or third photon in the CARS process (or both) is resonant with an excited electronic state. Tuning photon 1 or 3 to resonance is an effective way of enhancing the CARS signal by several orders of magnitude.[23–26] Such enhancement may be necessary in order to obtain any signal at all from experiments on molecules seeded in supersonic jets. With respect to the CARS process, we note that use of a resonance condition effectively lengthens the time spent in the excited electronic state. It is then necessary to determine whether relaxation processes in the excited electronic state influence the decay in the CARS signal. It emerges from our study that there is an inequivalence of the first and third photons in this respect.

II. THEORETICAL CONSIDERATIONS

We now examine the formulation of CARS, in terms of molecular properties, for the case that the incident radiation is pulsed. In traditional treatments the amplitude of the CARS signal is proportional to E_1, E_2, E_3, via $\gamma_{\rho\sigma\tau\nu}$, the third order molecular hyperpolarizability[15]:

$$P_\rho^{(3)}(\omega_0) = \frac{6}{n!}\frac{N}{4}\gamma_{\rho\sigma\tau\nu}(-\omega_0,\omega_1,\omega_2,\omega_3)$$
$$\times E_\sigma(\omega_1)E_\tau(\omega_2)E_\nu(\omega_3)\,. \tag{1}$$

In Eq. (1), ρ,σ,τ, and ν are polarization indices and ω_1, ω_2, and ω_3 are the frequencies of photons 1, 2, 3. $\gamma_{\rho\sigma\tau\nu}$ is a fourth rank tensor, hence is comprised of 81 (3^4) Cartesian components. Each of the 81 components contains 24 terms, corresponding to the number of permutations of the four photons in the CARS process. N is the particle density and n is the number of identical frequencies.

γ is formulated in the energy representation.[15,21–23] In this representation each of the 24 terms contains a fourfold product of Franck–Condon matrix elements, formally involving all the molecular eigenstates. Clearly, if many states contribute to the scattering process, evaluation of these terms becomes prohibitively difficult. Furthermore, and more important for the present discussion, the conventional expression for γ is useful only for the case of four cw photons. If, as a consequence of using pulsed radiation, there is a significant spread in the frequencies of the three incident fields, γ must be evaluated for all combinations of the frequencies, and integrated over ω_1, ω_2, and ω_3.

In this paper we introduce a time-frame expression for the CARS amplitude, valid for pulsed or cw radiation, which avoids all the above difficulties. We deal directly with $P^{(3)}(\omega_0)$ and thereby circumvent the calculation of γ at all combinations of frequencies. Our expression can readily be used to interpret CARS experiments performed in a pump-and-probe fashion. Moreover, the expression obtained is amenable to a wave packet interpretation, where the important wave packet dynamics depend on how close to resonance each of the photons is tuned. The traditional CARS frequency matching condition $\omega_0 = \omega_1 - \omega_2 + \omega_3$ must be generalized for non-cw radiation. In that case the matching condition refers to the Fourier component at ω_0 of the convolution of the radiation field with the wave packet recurrences. The cw expression for $P_\rho^{(3)}$, including the energy frame representation for γ, may be recovered from our expression by integrating over time.

The fourth order time-dependent perturbation theory expression for $P^{(3)}(\omega_0)$ is

$$P_\rho^{(3)}(\omega_0) = k\frac{1}{\hbar^3}\int_{-\infty}^{\infty}\int_{-\infty}^{t_4}\int_{-\infty}^{t_3}\int_{-\infty}^{t_2} dt_4\,dt_3\,dt_2\,dt_1$$
$$\times \langle g|e^{i\omega_g t_4}(\mu_\rho\, e^{i\omega_0 t_4})\,e^{-iH(t_4-t_3)/\hbar}\,[\mu_\nu E_3(t_3)]\,e^{-iH(t_3-t_2)/\hbar}$$
$$\times [\mu_\tau E_2(t_2)]\,e^{-iH(t_2-t_1)/\hbar}\,[\mu_\sigma E_1(t_1)]\,e^{-i\omega_g t_1}|g\rangle$$
$$+ 23 \text{ permutation terms}\,. \tag{2}$$

In Eq. (2), μ_ρ, μ_ν, μ_τ, μ_σ are dipole moment operators and E_1, E_2, E_3 are the temporal field amplitudes corresponding to each of the incident photons. Formally, H is the full electronic–nuclear Hamiltonian. However, in practice H is the Born–Oppenheimer Hamiltonian of either the ground or excited electronic state, depending on the resonance condition satisfied by the preceding photons.

There are several different situations for which the fourfold integral in Eq. (2) can be simplified. For the common experimental situation where photons 1 and 3 are off resonance, to a very good approximation $e^{-iH(t_2-t_1)/\hbar}$ and $e^{-iH(t_4-t_3)/\hbar}$ can be replaced by $\delta(t_2-t_1)$ and $\delta(t_4-t_3)$, respectively. Substitution of these approximations yields

$$P_\rho^{(3)}(\omega_0) = k\frac{1}{\hbar^3}\int_{-\infty}^{\infty}\int_{-\infty}^{t_4} dt_4\,dt_2\langle g|e^{i\omega_g t_4}(\mu_\rho\, e^{i\omega_0 t_4})$$
$$\times [\mu_\nu E_3(t_4)]\,e^{-iH(t_4-t_2)/\hbar}\,[\mu_\tau E_2(t_2)]$$
$$\times [\mu_\sigma E_1(t_2)]\,e^{-i\omega_g t_2}|g\rangle + PT\,. \tag{3}$$

Equation (3) has the following interpretation: $\mu_\tau\mu_\sigma|g\rangle$ is an initial wave packet; $E_2(t_2)E_1(t_2)$ prepares this wave packet (or a component thereof) on the ground state Born–Oppenheimer surface and $e^{-iH(t_4-t_2)/\hbar}$ propagates it on the ground state Born–Oppenheimer surface. The projection is then taken onto $\langle g|\mu_\rho\mu_\nu$. Equation (3), with the above interpretation, is strongly reminiscent of the representation of two photon resonance Raman scattering.[27–30] In our context, it is the Fourier component at ω_0 of the convolution of the fields with the wave packet recurrences that determine $P_\rho^{(3)}(\omega_0)$.

The expression for the explicit time dependence of the

CARS amplitude can also be simplified. This time-dependent amplitude is given by

$$P_\rho^{(3)}(t_4)=\int_{-\infty}^{\infty} P_\rho^{(3)}(\omega_0)e^{-i\omega_0 t_4}\,d\omega_0\,, \tag{4}$$

which is simply the inverse Fourier transform of Eq. (2) or Eq. (3). The fourfold integral over time is seen to reduce to a threefold integral. We obtain, then, using Eq. (3) for $P_\rho^{(3)}(\omega_0)$

$$P_\rho^{(3)}(t_4)=\frac{2\pi k}{\hbar^3}\int_{-\infty}^{t_4} dt_2\langle g|e^{-i\omega_g t_4}(\mu_\rho)[\mu_\nu E_3(t_4)]$$
$$\times e^{-iH(t_4-t_2)/\hbar}[\mu_\tau E_2(t_2)]\,[\mu_\sigma E_1(t_2)]e^{-i\omega_g t_2}|g\rangle\,. \tag{5}$$

We show, in Sec. III, that Eq. (5) predicts dramatically different decay times for the resonant and nonresonant contributions to the CARS signals. This effect has been illustrated beautifully in the experiments reported by Zinth, Lauberau, and Kaiser,[7] and by Kamga and Sceats.[8]

A third set of simplifications arise when the temporal envelopes of the light pulses can be considered δ functions on the time scale of the IVR (or other dynamical process). In the case where we can approximate $E_1(t_2)E_2(t_2)$ as $\overline{E}_1\overline{E}_2\delta(t_2-t_2^*)$ and $E_3(t_4)$ as $\overline{E}_3\delta(t_4-t_4^*)$, Eq. (5) simplifies to

$$P_\rho^{(3)}(t_4)\alpha\overline{E}_1\overline{E}_2\overline{E}_3\langle g|\mu_\rho\mu_\nu$$
$$\times e^{-iH(t_4^*-t_2^*)/\hbar}\mu_\tau\mu_\sigma|g\rangle\delta(t_4-t_4^*)+PT\,. \tag{6}$$

These simplifications are valid when the time scale separation $\tau_{\rm IVR}\gg\tau_{\rm pulse}\gg\tau_{\Delta\omega}$ holds, where $\Delta\omega$ is the mismatch of the incident frequencies from an electronic transition.

Of course, in the fully general case photon 1 and photon 3 may be resonant with an excited electronic state and Eq. (2) must be used to calculate the intensity; however, under resonance conditions only a few of the 24 terms make significant contributions to the CARS amplitude.

In order to recover the formula for $\gamma_{\rho\sigma\tau\nu}$ in Ref. 15 we return to Eq. (2) and set

$$\begin{aligned}E_1(t_1)&=E_1\,e^{-i\omega_1 t_1}\,,\\ E_2(t_2)&=E_2\,e^{i\omega_2 t_2}\,,\\ E_3(t_3)&=E_3\,e^{-i\omega_3 t_3}\,.\end{aligned} \tag{7}$$

We now rewrite Eq. (2) in an expanded form:

$$P_\rho^{(3)}(\omega_0)=\frac{k}{\hbar^3}\int_{-\infty}^{\infty}\int_{-\infty}^{t_4}\int_{-\infty}^{t_3}\int_{-\infty}^{t_2} dt_4\,dt_3\,dt_2\,dt_1\,E_1\,E_2\,E_3$$
$$\times\langle g|\mu_\rho\,e^{-iH(t_4-t_3)/\hbar}\,e^{i(\omega_3-\omega_2+\omega_1+\omega_g)(t_4-t_3)}\,\mu_\nu \tag{8}$$
$$\times e^{-iH(t_3-t_2)/\hbar}\,e^{i(-\omega_2+\omega_1+\omega_g)(t_3-t_2)}\,\mu_\tau\,e^{-iH(t_2-t_1)/\hbar}\,\mu_\sigma$$
$$e^{i(\omega_1+\omega_g)(t_2-t_1)}\,|g\rangle\,e^{-i(\omega_g+\omega_1-\omega_2+\omega_3-\omega_0-\omega_g)t_4}\,.$$

[The reader may easily verify the equivalence of this equation to Eq. (2). The additional phase factors in this expression cancel out in a domino-like fashion.] We then transform to the new variables

$$\begin{aligned}W&=t_2-t_1\,,\\ X&=t_3-t_2\,,\\ Y&=t_4-t_3\,,\\ t_4&=t_4\,.\end{aligned}$$

Making use of the integral representation for the delta function, we obtain

$$P_\rho^{(3)}(\omega_0)=\frac{k}{\hbar^3}\int_0^{\infty}\int_0^{\infty}\int_0^{\infty} dW\,dX\,dY$$
$$\times\langle g|\mu_\rho e^{-iHY}\,e^{i(\omega_3-\omega_2+\omega_1+\omega_l)Y}\mu_\nu\,e^{-iHX}$$
$$\times e^{i(-\omega_2+\omega_1+\omega_l)X}\mu_\tau e^{-iHW}\,e^{i(\omega_1+\omega_l)W}\mu_\sigma|g\rangle$$
$$\times E_1E_2E_3\delta(\omega_g+\omega_1-\omega_2+\omega_3-\omega_0-\omega_g)+PT\,. \tag{9}$$

Inserting three complete sets of states ($|j\rangle,|k\rangle,|l\rangle$) and integrating over W, X, and Y we obtain

$$P_\rho^{(3)}(\omega_0)$$
$$=\left(\frac{k}{\hbar^3}\int_{j,k,l}\frac{\langle g|\mu_\rho|l\rangle\langle l|\mu_\nu|k\rangle\langle k|\mu_\tau|j\rangle\langle j|\mu_\sigma|g\rangle}{(\omega_{jg}-\omega_1)(\omega_{kg}-\omega_1+\omega_2)(\omega_{lg}-\omega_0)}+PT\right)$$
$$\times E_1E_2E_3\delta(\omega_1-\omega_2+\omega_3-\omega_0) \tag{10a}$$
$$=k\gamma_{\rho\sigma\tau\nu}E_\sigma(\omega_1)E_\tau(\omega_2)E_\nu(\omega_3)\delta(\omega_1-\omega_2+\omega_3-\omega_0)\,. \tag{10b}$$

The first term in parentheses in Eq. (10a) is precisely the second term in Eq. (37) of Ref. 15. The other terms may be obtained by permutation of ω_1, $-\omega_2$, ω_3, and $-\omega_0$. Note the δ function condition on ω_0, which represents the conventional CARS frequency matching condition.

III. NUMERICAL CALCULATIONS

In this section we demonstrate some of the great variety of behavior that arises from different choices for resonance conditions for each of the incident radiation fields and different possible intramolecular energy transfer pathways. First we consider the intensity and decay time of the CARS signal as a function of detuning $\omega_1-\omega_2$ from resonance with a low lying vibrational level of the ground electronic surface. Then we specialize to the case where this frequency difference is resonant with such a level. We consider several different forms for the decay of the CARS signal, arising from the "small," "intermediate," and large molecule cases. We observe strong beat patterns for the two-state case, with the regularity and intensity of the beats decreasing as the "size" of the molecule is increased. The limiting case of an infinite number of coupled states can be described analytically, and is approached arbitrarily closely for increasingly large but finite numbers of states.

It is instructive to examine the behavior of $P_\rho^{(3)}(t_4)$ without including $E_3(t_3)$ in order to obtain a global picture for a variety of different delay times of photon 3 relative to photon 2. We therefore examine the quantity

$$P_\rho'(t_4)\int_{-\infty}^{t_4} dt_2\langle g|\mu_\rho\mu_\nu\,e^{-iH(t_4-t_2)/\hbar}$$
$$\times\mu_\tau\mu_\sigma|g\rangle E_2(t_2)E_1(t_2)\,e^{-i\omega_g t_2}\,. \tag{11}$$

$P_\rho^{(3)}(t_4)$ may be obtained from P_ρ' (for photon 3 nonresonant with an excited electronic state) by simply multiplying P' by a narrow envelope in time at the desired delay. For definiteness we suppose that $E_2(t_2)E_1(t_2)$ has the form

$$E_2(t_2)E_1(t_2)=a(t_2)e^{-i(\omega_1-\omega_2)t_2}, \tag{12}$$

where the envelope function $a(t_2)$ is given by

$$a(t_2)=\frac{1}{(2\pi\sigma^2)^{1/4}}\exp(-t_2^2/2\sigma^2)\,. \tag{13}$$

We are interested in a product pulse which is narrow in time (of order 1 ps) while at the same time relatively narrow in

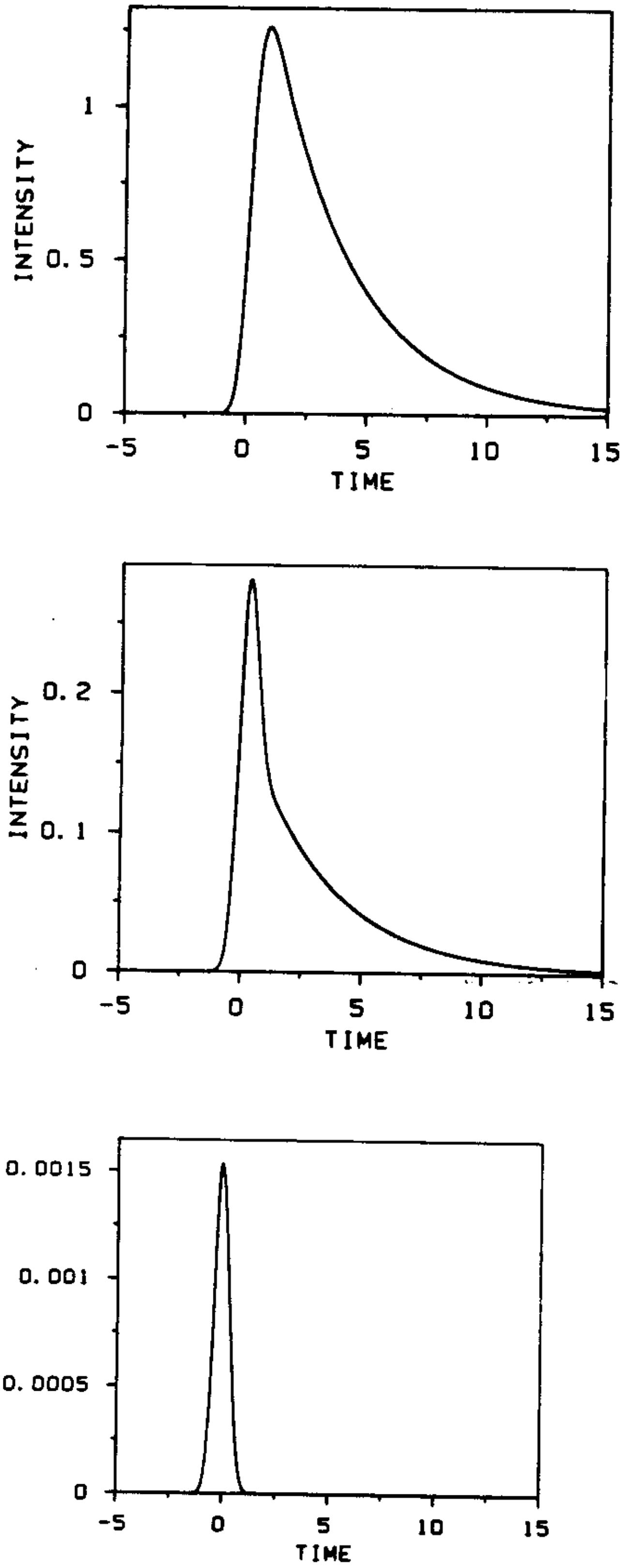

FIG. 1(a). The intensity of the CARS signal vs delay time for photon 3 (ps). The pulse shapes are Gaussian with time constant $\sigma = 0.5$ ps and $\Gamma_{\rm IVR} = 0.15\ {\rm ps}^{-1}$. The frequency difference $\Delta\omega = \omega_g + \omega_1 - \omega_2 - \omega_s = 0$. The decay of the CARS signal is determined by the time constant for the IVR. (b) Same as Fig. 1(a) but $\Delta\omega = 3\ {\rm ps}^{-1}$. The overall intensity is greatly reduced, and the decay time is now much faster than the IVR time constant. (c) Same as Figs 1(a) and 1(b) but $\Delta\omega = 30\ {\rm ps}^{-1}$. The overall intensity is two orders of magnitude smaller than in Fig. 1(b) and the CARS signal vanishes when the initial excitation is finished.

frequency (of order ten wave numbers), with a central frequency $\omega_1 - \omega_2$. Furthermore, we assume that

$$C(t) = \langle g|\mu_\rho \mu_\nu\, e^{-iHt/\hbar} \mu_\tau \mu_\sigma |g\rangle$$

$$\simeq e^{-\Gamma_{\rm IVR} t} e^{i\omega_s t}. \tag{14}$$

The exponential decay of IVR on the ground state potential surface is a crude but useful description of that process in many molecules. It may be justified on theoretical grounds by considering the Bixon–Jortner level coupling scheme.[31] In Eq. (14), ω_s is the central frequency for the vibrational feature s.

Equation (11) may now be rewritten in the form

$$P'_\rho(t_4) = \int_{-\infty}^{t_4} a(t_2)\, e^{-\Gamma_{\rm IVR}(t_4 - t_2)}\, e^{i\Delta\omega(t_4 - t_2)}\, dt_2, \tag{15}$$

where $\Delta\omega = \omega_g + \omega_1 - \omega_2 - \omega_s$ represents the detuning of the difference frequency from the vibrational transition.

Figure 1 displays a plot of $|P'_\rho(t_4)|^2$ vs t_4 when $\Gamma_{\rm IVR} = 0.15\ {\rm ps}^{-1}$, $\sigma = 0.5$ ps, and $\Delta\omega = 0$, 3, and 30 ps^{-1}. The CARS signal is observed to decay much more quickly as the detuning is increased, and the overall intensity of the nonresonant signal is much lower than the resonant signal. These observations are in agreement with the results of Zinth, Laubereau, and Kaiser[7] who demonstrate the effects mentioned both experimentally and numerically. Kamga and Sceats[8] used the effect gainfully to eliminate nonresonant background from the CARS signal from two component liquids.

In Figs. 2–4 we again consider $|P'_\rho(t_4)|^2$ as a function of t_4. We specialize to the case $\Delta\omega = 0$, and we now consider a different model for the IVR on the ground state surface. The zeroth order level s is coupled to its "nearest neighbor" zeroth order level only. This second zeroth order level is in turn coupled to its nearest neighbor level, and so on. The energy of each of the zeroth levels is taken to be the same, as is the coupling between levels. This is a crude model of a long chain molecule, or of a set of normal modes that are coupled in sequence. The number of coupled levels is varied from two

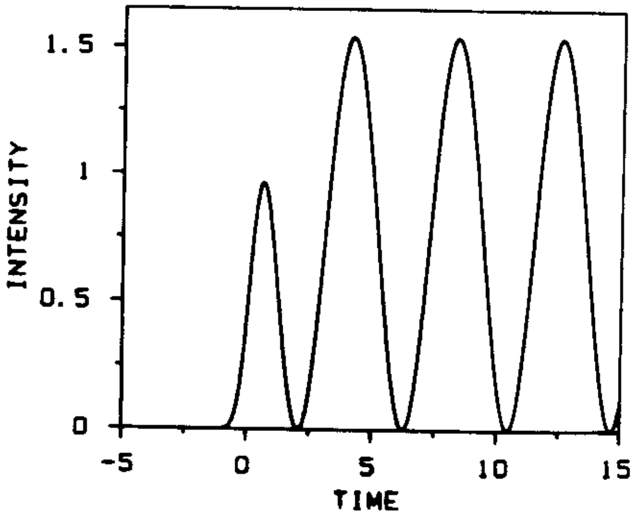

FIG. 2. CARS intensity vs delay time. The pulse shapes are Gaussian with time constant $\sigma = 0.5$ ps. IVR is that of a two-level system ($N = 2$) resulting in quantum beats with complete and regular recurrences. The coupling parameter, $v = 0.75\ \hbar\text{-ps}^{-1}$.

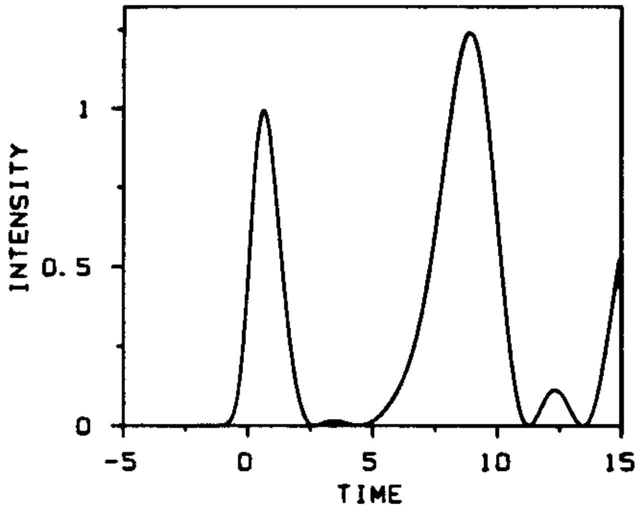

FIG. 3. Same as Fig. 2 but for $N = 5$. The quantum beats are still strong but irregular.

to 5 to 10, simulating small, intermediate, and large molecules. Mathematically, the coupling matrix is tridiagonal, with all diagonal elements equal and all near-diagonal elements equal. The eigenvectors and eigenvalues for this matrix can be evaluated analytically; furthermore, the form of the decay for N coupled levels is an N-point quadrature approximation to another analytic function, which represents the limiting decay for an infinite number of coupled levels. Interestingly, this limiting decay shows early time recurrences in the CARS signal despite irreversible long time decay.

The eigenvalue equation for the tridiagonal matrix is

$$\begin{pmatrix} E_s & v & & & & \\ v & \cdot & & & & \\ & & \cdot & & & \\ & & & \cdot & & \\ & & v & E_s & v & \\ & & & v & \cdot & \\ & & & & & \cdot \end{pmatrix} \begin{pmatrix} a \\ \cdot \\ \cdot \\ \cdot \\ b_i^n \\ \cdot \\ \cdot \\ \cdot \end{pmatrix} = E_n \begin{pmatrix} a \\ \cdot \\ \cdot \\ \cdot \\ b_i^n \\ \cdot \\ \cdot \\ \cdot \end{pmatrix}. \tag{16}$$

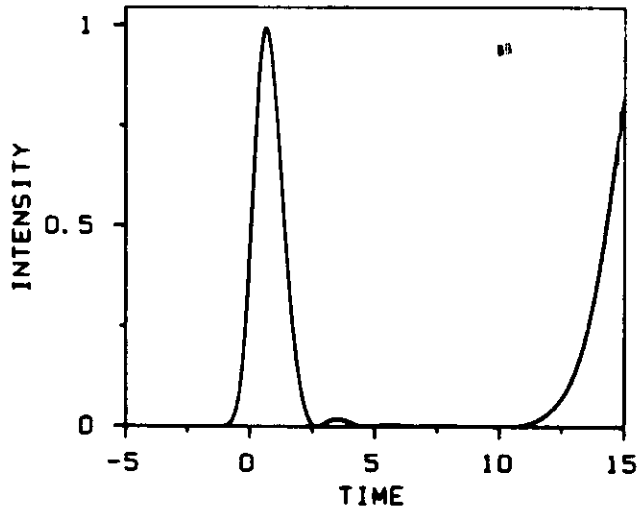

FIG. 4. Same as Fig. 2 but for $N = 10$. Note the weak, early recurrences as well as the (truncated) strong, later recurrence.

We assume $E_i = E_s$. The solution to the eigenvalue equation is

$$\begin{aligned} E_n &= E_s - 2v \cos\left(\frac{n\pi}{N+1}\right), \\ a_n &= \sin\left(\frac{n\pi}{N+1}\right)B, \\ b_i^n &= \sin\left(\frac{in\pi}{N+1}\right)B, \\ B &= \left[\sum_{k=1}^{N} \sin^2\left(\frac{k\pi}{N+1}\right)\right]^{-1/2}, \end{aligned} \tag{17}$$

and the autocorrelation function of the initial level $C(t) = \langle s|e^{-iH_et}|s\rangle$ is given by

$$\begin{aligned} C(t) &= \sum_n a_n^2 \, e^{-iE_nt/\hbar}, \\ &= \sum_{n=1}^{N} \sin^2\left(\frac{n\pi}{N+1}\right) \exp\left[2iv \cos\left(\frac{n\pi}{N+1}\right)t/\hbar\right] \\ &\quad \times B^2 e^{-iE_st/\hbar}. \end{aligned} \tag{18}$$

Figure 2 shows the time dependence of $|P_\rho'(t_4)|^2$ for the two-level case. Note the complete recurrences at times $n\tau = 2\pi n/\omega$. It is remarkable that the first feature ($t = 0$) has less amplitude than the others; this is because it represents the convolution of the waveform $a(t)$ with the one-sided function $C(t)$, $t > 0$. Figure 3 shows the five-level case. The initial decay is very similar to that in Fig. 2 but the recurrences are on a longer time scale and more irregular in the five-level case. Figure 4 shows the ten-level case. The strong recurrences are, relative to those in Figs. 2 and 3, pushed farther out in time. There is, however, a weak sequence of recurrences at short times ($t = 3.5$, 7 ps), which persist in position and intensity as N increases further.

As one might expect, $C(t)$ approaches a limiting form as N goes to infinity. In fact, we now show that $C(t)$ for finite N represents an N-point quadrature approximation to the infinite N case. We may rewrite Eq. (18) as

$$\frac{\sum_{n=1}^{N} \omega_n \frac{(N+1)}{\pi} e^{(i/\hbar)2vx_nt}}{\sum_{k=1}^{N} \omega_n \frac{(N+1)}{\pi}}, \tag{19}$$

where

$$\begin{aligned} \omega_n &= \frac{\pi}{N+1} \sin^2\left(\frac{n\pi}{N+1}\right), \\ x_n &= \cos\left(n\frac{\pi}{N+1}\right). \end{aligned} \tag{20}$$

We note that Eq. (19) is approximately equal to

$$\begin{aligned} &[(N+1)/\pi] \int_{-1}^{+1} e^{(i/\hbar)2vxt} (1-x^2)^{1/2}\, dx \\ &\quad [(N+1)/\pi] \int_{-1}^{+1} (1-x^2)^{1/2}. \end{aligned} \tag{21}$$

The integrals in Eq. (21) can be performed analytically, yielding

$$C(t) = \frac{\hbar}{vt} J_1\left(\frac{2vt}{\hbar}\right) \tag{22}$$

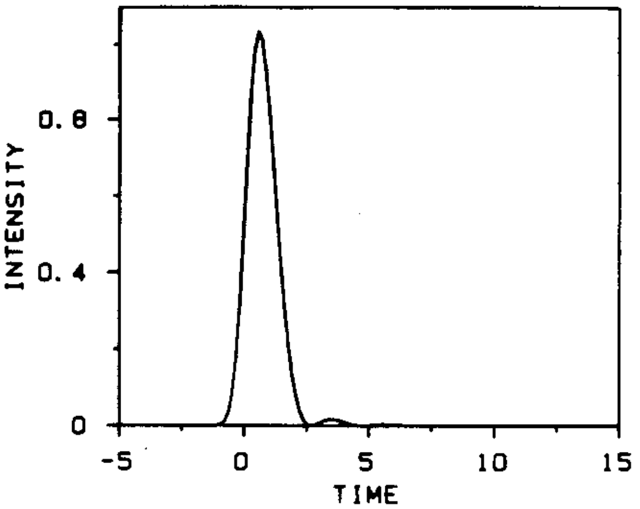

FIG. 5. Same as Fig. 2 but for $N = \infty$. The correlation function $C(t)$ was determined analytically as the limit of an N-point quadrature approximation as $N \rightarrow \infty$, and is given by $(\hbar/vt)J_1(2vt/\hbar)$ (see the text). Note that the weak, early recurrences persist while the strong, late recurrences are absent.

which is the limiting form for the decay of the autocorrelation function as $N \rightarrow \infty$. Figure 5 shows the function $|P'_p(t_4)|^2$ vs t_4 corresponding to Eq. (22). Note that short time recurrences persist while long time, strong recurrences, do not.

Figures 6 and 7 show

$$\left| \int_{-\infty}^{t_4} \int_{-\infty}^{t_2} dt_1\, dt_2 \times \langle g | e^{-iH_g(t_4 - t_2)} b(t_2) e^{-iH_{ex}(t_2 - t_1)} a(t_1) e^{-i\omega_g t_1} | g \rangle \right|^2 \quad (23)$$

as a function of t_4. In both figures the overlap function is taken to have the functional form $C(t) = [J_1(2\Gamma t)/\Gamma t]$ on the excited *and* the ground state potential surfaces, as motivated above. Γ is taken to be 0.75 ps^{-1} on the ground state surface in both plots while it is 0.7 ps^{-1} on the excited surface for Fig. 6 and 0.07 ps^{-1} on the excited state surface for Fig. 7. Comparison of Figs. 6 and 7 yields the interesting result that the decay of the CARS signal is insensitive to the rate of decay of IVR in the excited electronic state. This conclusion holds whether the IVR is much faster, comparable to, or much slower than the time envelope of the waveforms a and b. Indeed, the only assumption required for this conclusion to be valid is that the centers of the waveforms a and b are coincident in time, for the following reasons. The convolution

$$\tilde{\gamma} = \int_{-\infty}^{t_2} \langle g | e^{-iH_{ex}(t_2 - t_1)/\hbar} a(t_1) | g \rangle dt_1 \quad (24)$$

is very sensitive to the IVR rate on the excited state potential surface: if Γ is very large $\tilde{\gamma}$ will be very sharply peaked in time; if Γ is very small $\tilde{\gamma}$ will be very broad in time. However, the convolution will have a minimum width equal to the width of $a(t_1)$. Since b has the same width as a, and its center is coincident with the center of a, the product of b with the convolution is just the width of b. It is interesting to note that one may insert an adjustable delay between photons 1 and 2, now taking care that photon 2 is coincident with photon 3. Then the IVR from a vibrational level in the excited electronic surface is probed with no complications arising from ground electronic state IVR. This small change in experimental setup allows, in principle, a ready comparison of IVR rates of the corresponding vibrational levels in the excited and the ground electronic states.

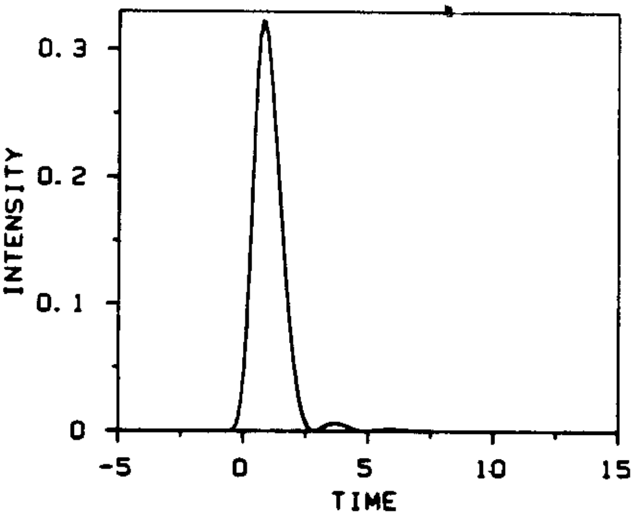

FIG. 6. Resonant CARS intensity vs delay time. $\Gamma_{ex} = 0.7$ ps^{-1}, $\Gamma_g = 0.75$ ps^{-1}.

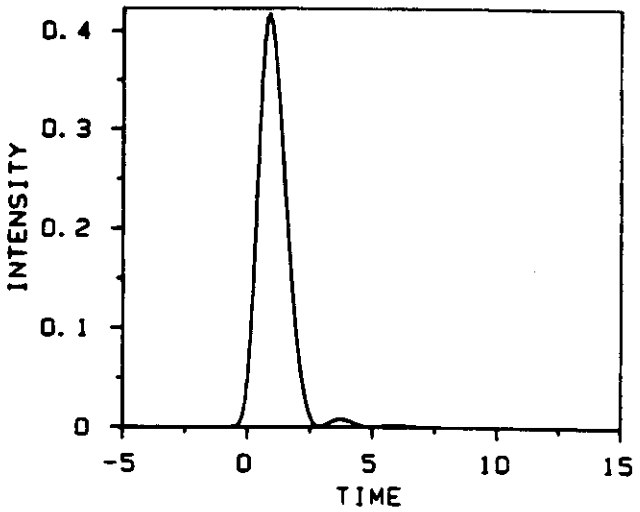

FIG. 7. Resonant CARS intensity vs delay time. $\Gamma_{ex} = 0.07$ ps^{-1}, $\Gamma_g = 0.75$ ps^{-1}. Comparison with Fig. 6 shows that the resonant CARS signal is insensitive to the rate of IVR on the excited state potential surface.

It is important to note that the above arguments do not apply to photons 3 and 4. When photon 3 is resonant the emission of photon 4 may be significantly delayed, because photon 4 is emitted spontaneously. Hence, the quasicoincidence of the waveforms of photons 3 and 4, which was assumed above, is no longer guaranteed. Excited state IVR may now contribute to the decay of the CARS signal, and no simple interpretation in terms of ground state IVR will be possible.

IV. CONCLUSIONS

In this paper we have demonstrated the fruitfulness of formulating CARS in terms of a time-frame quantum mechanical expression, i.e., fourth order time-dependent perturbation theory. This formulation includes the standard energy frame formula as a special case, when there are four cw photons, but is also valid for arbitrary waveforms for the photons. Our expression is required to properly describe picosecond CARS experiments when an adjustable delay is introduced between any pair of the photons. It emerges from our treatment that the traditional CARS frequency matching condition $\omega_0 = 2\omega_1 - \omega_2$ must be generalized for non-cw fields; in that case it refers to the Fourier component at ω_0 of the convolution of the radiation field with the wave packet recurrences.

We have discussed the role of resonance, both in the ground electronic state (generated by photons 1 and 2) and in the excited electronic state (generated by photons 1 or 3 or both), and have calculated how resonance conditions affect the decay of the CARS signal. Although many different uses for time-dependent CARS techniques can be envisaged, we have dealt mainly with some questions related to using CARS as a probe of ground electronic state IVR. The disappearance of the Rayleigh line in frequency space experiments is a signature of IVR, and may be understood in terms of the decay of wave packet recurrences.[32] The same IVR process manifests itself also in the decay of the CARS signal in time. Model calculations show that quantum beats in the decay of the CARS signal may occur, reflecting either a small number of coupled states (strong and regular recurrences) or a sequential coupling mechanism for a large number of states (weak and early recurrences).

ACKNOWLEDGMENTS

This research has been supported by grants from the NSF and the AFOSR.

[1] K. P. Gross, D. M. Guthals, and J. W. Nibler, J. Chem. Phys. **70**, 4673 (1979).

[2] W. M. Hetherington, III, G. M. Korenowski, and K. B. Eisenthal, Chem. Phys. Lett. **77**, 275 (1981).

[3] P. L. Holt, K. E. McCurdy, R. B. Weisman, J. S. Adams, and P. S. Engel, J. Chem. Phys. **81**, 3349 (1984).

[4] J. J. Valentini, D. S. Moore, and D. S. Bomse, Chem. Phys. Lett. **83**, 217 (1981).

[5] D. P. Gerrity and J. J. Valentini, J. Chem. Phys. **81**, 1298 (1984).

[6] A. Laubereau and W. Kaiser, Rev. Mod. Phys. **50**, 607 (1978).

[7] W. Zinth, A. Laubereau, and W. Kaiser, Opt. Commun. **26**, 457 (1978).

[8] F. M. Kamga and M. G. Sceats, Opt. Lett. **5**, 126 (1980).

[9] R. Konig, A. Lau, and H. J. Weigmann, Chem. Phys. Lett. **69**, 87 (1980).

[10] P. L. Decola, J. R. Andrews, R. M. Hochstrasser, and H. P. Trommsdorff, J. Chem. Phys. **73**, 4695 (1980).

[11] K. Luther and W. Wieters, J. Chem. Phys. **73**, 4131 (1980).

[12] D. D. Dlott, C. L. Schosser, and E. L. Chronister, Chem. Phys. Lett. **90**, 386 (1982).

[13] A. M. Brodnikovsky, S. M. Gladkov, and N. I. Koroteev, Opt. Commun. **40**, 312 (1982).

[14] H. Graener, A. Laubereau, and J. W. Nibler, Opt. Lett. **9**, 165 (1984).

[15] For an excellent recent review see J. J. Valentini, in *Spectrometric Techniques* (Academic, New York, 1985), Vol. 4.

[16] K. V. Reddy, D. F. Heller, and M. J. Berry, J. Chem. Phys. **76**, 2814 (1982).

[17] E. L. Sibert, III, W. P. Reinhardt, and J. T. Hynes, Chem. Phys. Lett. **92**, 455 (1982).

[18] J. B. Hopkins, P. R. R. Langridge-Smith, and R. E. Smalley, J. Chem. Phys. **78**, 3410 (1983).

[19] A complete review is given by R. E. Smalley, J. Phys. Chem. **86**, 3504 (1982).

[20] C. A. Haynam, D. V. Brumbaugh, and D. H. Levy, J. Chem. Phys. **81**, 2282 (1984).

[21] J. A. Armstrong, N. Bloembergen, J. Ducuing, and P. S. Pershan, Phys. Rev. **127**, 1918 (1962).

[22] J. H. Christie and D. J. Lockwood, J. Chem. Phys. **54**, 1141 (1971).

[23] I. Chabay, G. K. Klauminzer, and B. S. Hudson, Appl. Phys. Lett. **28**, 27 (1976).

[24] J. Nestor, T. G. Spiro, and G. Klauminzer, Proc. Natl. Acad. Sci. USA **73**, 3329 (1976).

[25] B. Attal, O. O. Schnepp, and J.-P. E. Taran, Opt. Commun. **24**, 77 (1978).

[26] S. A. J. Druet, B. Attal, T. K. Gustafson, and J. P. Taran, Phys. Rev. A **18**, 1529 (1978).

[27] S. Y. Lee and E. J. Heller, J. Chem. Phys. **71**, 4777 (1979).

[28] E. J. Heller, R. L. Sundberg, and D. J. Tannor, J. Phys. Chem. **86**, 1822 (1982).

[29] D. J. Tannor and E. J. Heller, J. Chem. Phys. **77**, 202 (1982).

[30] R. L. Sundberg and E. J. Heller, Chem. Phys. Lett. **93**, 586 (1982).

[31] M. Bixon and J. Jortner, J. Chem. Phys. **48**, 715 (1968).

[32] D. J. Tannor, M. Blanco, and E. J. Heller, J. Phys. Chem. **88**, 6240 (1984).

Control of selectivity of chemical reaction via control of wave packet evolution

David J. Tannor and Stuart A. Rice
Department of Chemistry and The James Franck Institute, The University of Chicago, Chicago, Illinois 60637

(Received 21 July 1985; accepted 9 August 1985)

A time-dependent formulation of two-photon spectroscopy is employed to show that selectivity of reactivity can be achieved via coherent two-photon processes. The problem of finding the optimum waveform (i.e., coherent pulse sequence) that will maximize the formation of a desired chemical species is formulated as a problem in the calculus of variations, and solved for two different cases.

I. INTRODUCTION

Is it possible, by control of the nature of the excitation process, to control the selectivity of a chemical reaction? Previous attempts to answer this question have focused attention on the free evolution of an excited molecule, treating the excitation and the evolution processes as separable. These analyses, and the various experiments carried out to date, lead to the conclusion that, because of rapid intramolecular vibrational redistribution, laser induced selectivity of reaction is not, in general, feasible.[1] In this short paper we show that, despite dephasing of a prepared vibrational state distribution, selectivity of chemical reactivity can be achieved by use of coherent two-photon processes.

II. GENERAL CONCEPTS

Our procedure for controlling reaction selectivity is based on an inversion of the usual interpretation of two-photon spectroscopy. The probability of a two-photon transition between states ϕ_i and ϕ_f is proportional to[2]

$$\left|\int_{-\infty}^{\infty}\int_{-\infty}^{t_2}\langle\phi_f|b(t_2)e^{-iH(t_2-t_1)/\hbar}a(t_1)|\phi_i\rangle dt_1\,dt_2\right|^2, \tag{1}$$

where $a(t_1)$ and $b(t_2)$ are the forms of the first and second electromagnetic field pulses and H is the Hamiltonian for propagation of the coupled molecule and radiation field. In Eq. (1), $|\phi_i\rangle = \mu|\chi_i\rangle$ and $\phi_f = \mu|\chi_f\rangle$, where μ is the transition dipole moment and χ_i and χ_f are the initial and final vibrational state functions (with energies ω_f and ω_i in units of $\hbar$). The phase factors $\exp(-i\omega_i t_1)$ and $\exp(i\omega_f t_2)$ associated with χ_i and χ_f have been subsumed into $a(t_1)$ and $b(t_2)$, respectively. In the conventional interpretation, $a(t_1)$ and $b(t_2)$ are thought of as "given." The probability of transition (1) determines the distribution of intensity observed in, e.g., an absorption fluorescence or absorption-stimulated fluorescence experiment, the result being an accepted consequence of selection rules and molecular parameters. We, instead, ask the question: what are the waveforms and/or pulse sequences that optimize the probability of transition to a specified final state from a specified initial state? This question can be formulated as a variational problem for the functions $a(t_1)$ and $b(t_2)$. That formulation leads to equations that can be solved analytically in simple cases, e.g., stimulated fluorescence emission, but in general must be solved numerically.

It is important to note that Eq. (1) refers to the case of transition between a specified initial state and a specified final state. We shall be concerned with the case when transitions to several final states or a continuum of final states must be considered, as when only the chemical identities and not the internal levels of a set of products of a reaction define the result of interest. For ease of comprehension we present our analysis in terms of a simple example.

Consider the hypothetical ground electronic state Born–Oppenheimer potential surface shown in Fig. 1. The surface has a central minimum and two different exit channels, each separated from the minimum by a saddle point. The minimum corresponds to a stable form for the reactant molecule ABC, whereas the exit channels correspond to formation of products via the reactions (i) ABC→AB + C and (ii) ABC→A + BC. There are several ways, in general, to promote one or both of these reactions. We explore whether one can maximize the probability of a desired pathway, e.g., favoring ABC→AB + C over ABC→A + BC. We are not concerned with individual final states of the products of the reaction, but only with the fraction of each fundamentally different chemical species produced. For the potential surface shown in Fig. 1, there is a qualitative and quantitative distinction between the two exit channels. We define a projection operator that includes the coordinate space associated with each exit channel, and form the following analog of Eq. (1):

$$\begin{aligned}\lim_{T\to\infty}&\int_{-\infty}^{T}\int_{-\infty}^{t_2}\int_{-\infty}^{T}\int_{-\infty}^{t_2'}dt_1'\,dt_2'\,dt_1\,dt_2\\&\times\langle\phi_i|e^{iH_{ex}(t_2-t_1)/\hbar}\mu e^{iH_g(T-t_2)/\hbar}P_{1,2}e^{-iH_g(T-t_2')/\hbar}\\&\times\mu e^{-iH_{ex}(t_2'-t_1')/\hbar}|\phi_i\rangle a(t_1)b(t_2)a(t_1')b(t_2')\,.\end{aligned}\tag{2}$$

In Eq. (2), P_1 and P_2 are projection operators corresponding to channels (i) and (ii), respectively. P_1 is defined by

$$P_1=\int_{\text{allspace}}|x\rangle\langle x|H(|x-x_1|)dx\,, \tag{3}$$

where $H(x)$ is the Heaviside function,

$$\begin{aligned}&H(x)=1,\quad x>0,\\&H(x)=0,\quad x<0.\end{aligned}\tag{4}$$

P_2 is defined similarly. In practice, we have identified x with the angle (0 to $\pi/2$) that measures progress along the reaction path [see Eq. (11)].

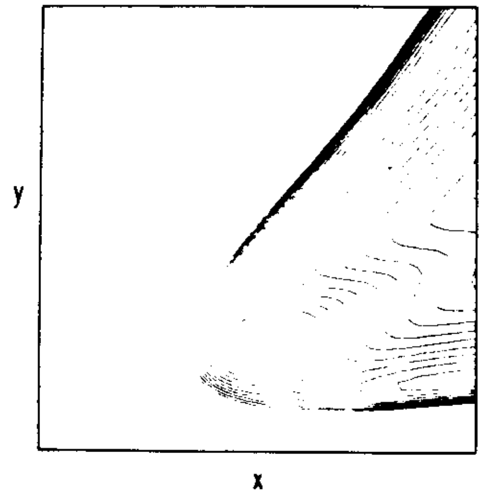

FIG. 1. Ground electronic state potential surface. This surface supports a stable triatomic, ABC, which may dissociate to A + BC [channel (i)] or AB + C [channel (ii)].

III. OPTIMIZATION

The two different expressions for the intensity of interest, Eqs. (1) and (2), are optimized in different ways, but in both cases with respect to $b(t_2)$. We choose for a constraint the condition

$$\int_{-\infty}^{\infty} |b(t_2)|^2 dt_2 = 1 . \tag{5}$$

Since $|b(t_2)|^2$ is proportional to the intensity of the second light pulse, the constraint fixes the total number of photons at our disposal.

Using a variational procedure, along with the method of Lagrange multipliers, we obtain the following result for the optimization of Eq. (1) (see Appendix A):

$$b^*(t_2) \propto \int_{-\infty}^{t_2} \langle \phi_f | e^{iH(t_2 - t_1)/\hbar} | \phi_i \rangle a(t_1) dt_1 . \tag{6}$$

The interpretation of Eq. (6) is straightforward: The stimulating waveform should be "matched" to the convolution of the excitation pulse shape with the wave packet as it evolves subject to the dynamics on the excited state potential surface. This result has analogs in electrical engineering and information theory, where it is part of matched filter theory.[3]

Using the same procedure with respect to Eq. (2) yields the following result (see Appendix B):

$$\int_{-\infty}^{\infty} b(t_2') A'(t_2', t_2) dt_2' + \lambda b(t_2) = 0 , \tag{7}$$

where

$$A'(t_2', t_2) = \int_{-\infty}^{t_2} dt_1 \int_{-\infty}^{t_2'} dt_1' \, A(t_2, t_1, t_2', t_1',) a(t_1') a^*(t_1) \tag{8}$$

and

$$A = \lim_{t\to\infty} \langle \phi_i | e^{i\omega_i t_1} e^{iH_{ex}(t_2 - t_1)/\hbar} \mu e^{iH_g(T - t_2)/\hbar} | P_1 | e^{-iH_g(T - t_2')}$$
$$\times \mu e^{-iH_{ex}(t_2' - t_1')/\hbar} e^{i\omega_i t_1'} | \phi_i \rangle . \tag{9}$$

Equation (7) must be solved iteratively for $b(t_2)$ unless

$$A'(t_2, t_1) = A_2'(t_2) \times A_1'(t_1) , \tag{10}$$

in which case it reduces to the matched filter result for the single state projection.

IV. SELECTIVITY OF REACTIVITY

We now show that selectivity of reactivity is possible if an excited electronic state is used as an intermediary to "assist" chemistry on the ground electronic state surface. Our scheme supposes that the excited state surface that plays the role of an intermediary has both a displaced minimum and normal coordinates which are rotated relative to those of the ground state surface.

Consider, first, the classical trajectory that originates at the minimum of the ground state surface ($x = 0$, $y = 0$, $p_x = 0$, $p_y = 0$), and imagine this trajectory projected vertically onto the excited state surface. The trajectory now propagates along x as a result of a large Franck–Condon displacement in this coordinate. After several vibrational periods, because the excited state normal coordinates are not parallel to those of the ground state, the trajectory begins to wind around and oscillate along y (Lissajous motion). If the trajectory is now projected vertically down, back to the ground state surface, depending on when and where along the Lissajous motion on the excited state surface the projection starts, the new trajectory on the ground state surface may exit from channel (i), or channel (ii), or remain trapped in the well.

The quantum mechanical theory of two-photon processes is amenable to an interpretation very similar to the classical mechanical description given above. The "instant" of arrival of the first photon t_1 marks the vertical transition to the excited state surface and the instant of emission of the second photon t_2 marks the vertical transition back to the excited ground state surface, in conformity with the Franck–Condon principle. Quantum mechanically, the initial state ϕ_i is a localized wave packet; the motion of the center of this wave packet $\phi_i(t) = e^{-iHt/\hbar}\phi_i(0)$ is the analog of the classical trajectory discussed above. Under favorable conditions the wave packet remains narrow and will track its corresponding classical trajectory for many vibrational periods. This description has been advocated by Heller and co-workers[2,4] in discussing a variety of molecular spectroscopies. However, the available analyses refer to the case of continuous wave (cw) light, i.e., the use of the one or two photons with δ-function frequency distributions. Our interest is in arbitrary waveforms and, in particular, in coherent pulse sequences that will enhance the fraction of a desired reaction product. Still using Eq. (1) or its generalization (2), our scheme posits a shift in outlook from passive to active. Indeed, we are no longer referring to spontaneous emission, but to stimulated emission with carefully tailored waveforms.

One must distinguish clearly between the achievable control of wave packet propagation, phase of the wave packet, and production of the composite wave function. The wave packet propagation is only partially under experimental control. It is governed, first and foremost, by the forms of the ground and excited state potential surfaces; the experimenter can affect the wave packet propagation insofar as he/she selects the instant to change surfaces. Similarly, the phase of the wave packet is only partially under experimental control. There is a coordinate-dependent phase factor (which reflects the momentum of the wave packet) which is determined by the properties of the potential surfaces. However, there is also a coordinate-independent phase factor, which plays a vital role in determining the nodal patterns set up by several interfering wave packets, and which can be manipulated via control of the phase of the pulse. Finally, the composite waveform produced may be thought of as a superposition of some number of individual wave packets. The extension of the composite wave function, its component segments and the relative phases of these component segments are under experimental control, since these features are determined by the overall duration of the waveform of the light, the component pulse sequences and the relative phases of the component pulses, respectively.

Consider the two potential surfaces

$$V_g = D(\theta)\{(1 - e^{\beta(\theta)[l - l_{eq}(\theta)]})^2 - 1\}, \qquad (11)$$

where

$$D(\theta) = [0.170 - 0.019\{(72/\pi)^2(\theta - \pi/4)^2 - 2\} \times \exp\{-\tfrac{1}{2}(36/\pi)^2(\theta - \pi/4)^2\}] \text{ hartree}, \qquad (12)$$

$$\beta(\theta) = [1.058 - 0.333 \times \exp - \{\tfrac{1}{2}(15/\pi)^2(\theta - \pi/4)^2\}] \text{ bohr}^{-1}, \qquad (13)$$

$$l_{eq}(\theta) = [8.045 + 2.823 \times \exp\{-\tfrac{1}{2}(12/\pi)^2(\theta - \pi/4)^2\}] \text{ bohr}, \qquad (14)$$

and

$$V_{ex} = \tfrac{1}{2} m\omega_{x'}^2(x' - x_0')^2 + \tfrac{1}{2} m\omega_{y'}^2(y' - y_0')^2, \qquad (15)$$

where

$$\begin{aligned} m &= 1823\, m_e, \\ x_0' &= 1.1 \text{ bohr}, \\ y_0' &= 1.2 \text{ bohr}, \\ \omega_{x'} &= 0.010 \text{ a.u.}, \\ \omega_{y'} &= 0.0082 \text{ a.u.}, \\ x &= (2)^{-1/2}(x' + y') + 3.4727 \text{ bohr}, \\ y &= (2)^{-1/2}(x' - y') + 1.637 \text{ bohr}. \end{aligned} \qquad (16)$$

The contour plot for the ground state potential surface, shown in Fig. 1, uses (equal) mass skewed coordinates with $x = R_2 + \frac{1}{2} R_1$ and $y = (2)^{-1/2} R_1$, where $R_1 = -l \cos\theta + 10$ and $R_2 = -l \sin\theta + 10$, all distances in a.u.

Figure 2(a) shows the time dependence of AB-C→AB + C [exiting out of channel (i)], while Fig. 2(b) shows the time dependence for ABC→A + BC [exiting out of channel (ii)], as determined in a purely classical calculation. Note that vibrations on the excited state surface are assumed to be purely harmonic. The ground state surface is modeled after that for the reaction D + H_2→HD + H in the asymptotic regions of the potential surface, but a well with bound states is artificially introduced in the interaction region. The

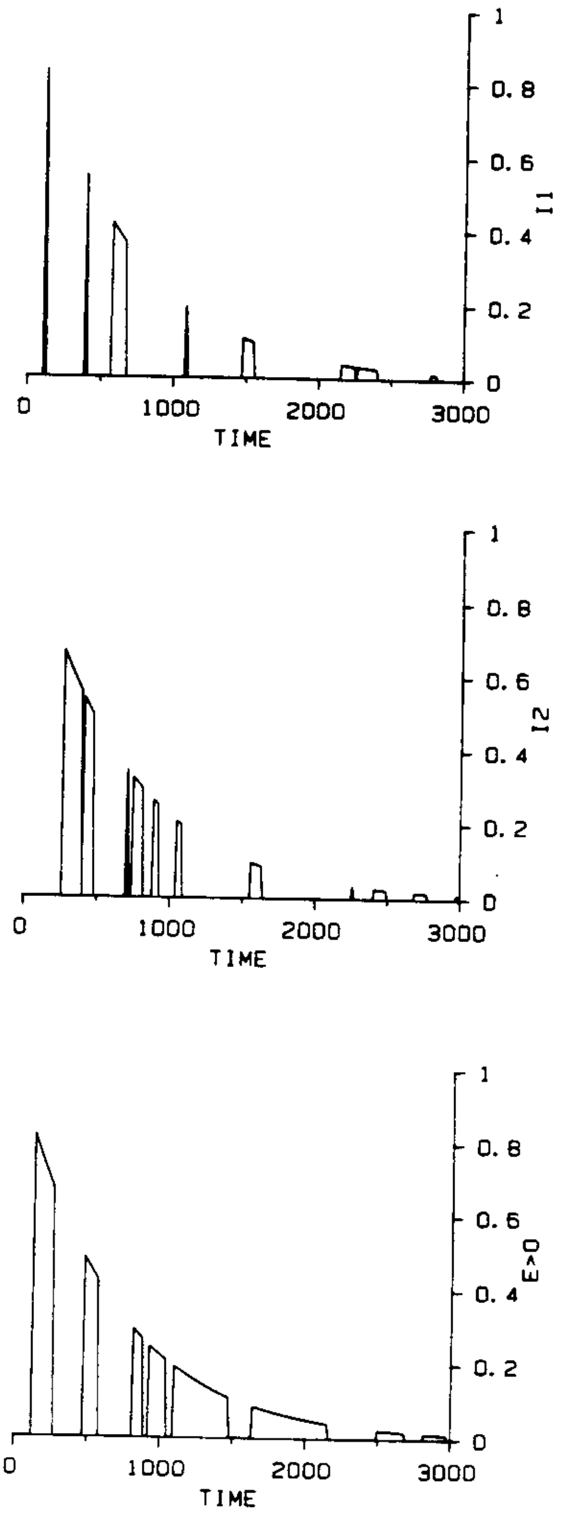

FIG. 2. (a) Probability of exit from channel (i), as a function of propagation time on the excited electronic state potential surface. After propagating on the excited state surface the trajectory makes a vertical transition back to the ground state surface, and is propagated until it reacts, or is deemed unreactive after 200 time steps (2000 a.u.). Because the propagation is classical, the probability for exit is a step function. The overall decay simulates a radiationless process, say intramolecular redistribution to other vibrational modes, as well as the effect of a finite radiative lifetime. (b) Probability of exit from channel (ii), as a function of propagation time on the excited state potential surface. (c) Probability of finding energy $E > 0$ on the ground state potential surface vs propagation time on the excited state potential surface. $E = 0$ is the energy for dissociation to A + B + C on the ground state potential surface.

coordinates of the well minimum are $x = 3.4727, y = 1.637$. The time axis refers to the delay of the vertical transition down relative to the vertical transition up (or equivalently, the propagation time on the excited state surface). Following projection from the excited state surface, the trajectories were propagated on the ground state surface until reaction occured. Reaction was defined in a transition state theory sense—crossing one or the other saddle point ($\theta > \theta_{\max}$, $\theta < \theta_{\min}$) with momentum in the direction of the exit ($p_\theta > 0$, $p_\theta < 0$, respectively),—or until 200 time steps (2000 a.u.) transpired, in which case the trajectory was deemed unreactive. Furthermore, trajectories with $E > 0$ (enough energy to dissociate to A + B + C) were considered as a separate class. The time dependence corresponding to these trajectories is shown in Fig. 2(c). Calculations using this breakdown were compared with one in which all trajectories were propagated 200 time steps on the ground state potential surface; agreement between the results with and without the transition state approximation mentioned was satisfactory. Figure 3(a) shows the probability of exit out of channel (i) assuming short Gaussian pulses for the pump and "probe" waveforms ($\sigma = 10$ a.u.). Figure 3(b) shows the analogous probability for exit from channel (ii). Note the dramatic selectivity for channel (i) at delay time $t \simeq 125$, and the selectivity for channel (ii) at delay time $t \simeq 300$. It is expected that the quantum mechanical effects of wave packet spreading and interference will alter the quantitative predictions for this (and any other) pair of potential surfaces, but that the qualitative extent of selectivity demonstrated here will persist.

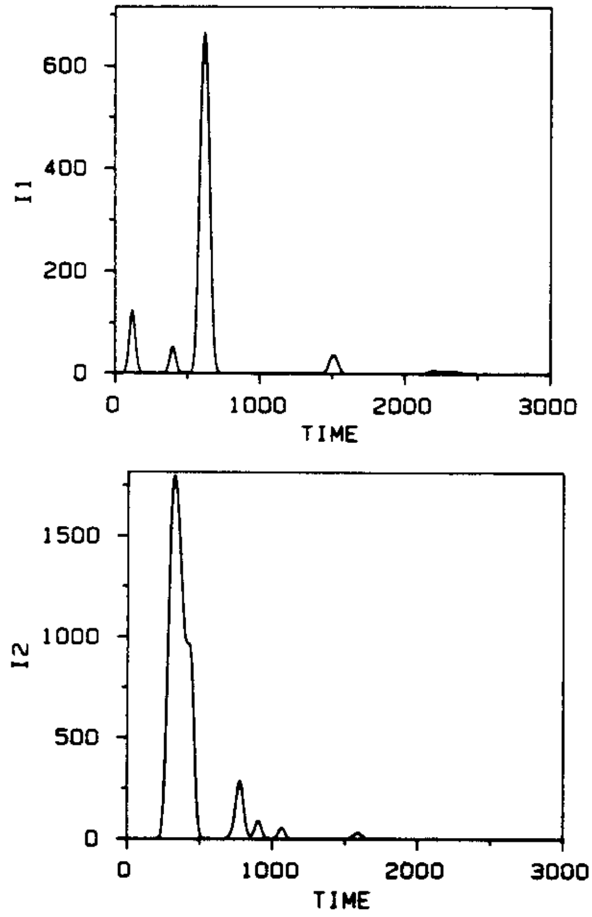

FIG. 3. (a) Square of the convolution of function displayed in Fig. 2(a) with narrow incident and stimulating Gaussian pulses $\sigma = 10$. a.u.). The time axis refers to the delay of the second pulse relative to the first. (b) Convolution of Fig. 2(b) with narrow incident and stimulating Gaussian pulses ($\sigma = 10$ a.u.).

Our method of controlling the selectivity of a reaction depends on the coherence of the dephasing of the wave packet prepared on the excited state potential energy surface. By virtue of its preparation, that wave packet can by thought of as a superposition of component eigenstates each of which has a nonvanishing transition dipole matrix element with the initial state on the ground state surface. Of course, each of the eigenstate components of the wave packet evolves deterministically, under an evolution operator defined by its energy, so at any time following absorption of the first photon the relative phases of the components of the wave packet are well defined and known. Then our optimization of the second pulse waveform achieves the best stimulated emission from all of the components of the prepared wave packet, i.e., the effects of intramolecular vibrational redistribution on the excited state potential surface are used to best advantage.

However, for many molecules of interest there exist radiationless transitions which couple the levels of an electronically excited surface to a dense manifold of quasidegenerate levels on one or more other electronic surfaces, and these latter levels have vanishingly small transition dipole matrix elements with the initial level on the ground state surface. This process depletes the prepared state and, therefore, competes with stimulation of emission to an extent that depends on the time delay between pumping and stimulating pulses. We have shown elsewhere, in a study of time delayed coherent anti-Stokes Raman spectroscopy,[5] that exponential decay of the amplitude of a wave packet on an excited state surface via, say, a radiationless process, reduces the amplitude of a coherent emission signal but does not destroy the coherence necessary to create the emission signal. Provided the quantum yield of fluorescence of 0.01 or greater, the rate of the radiationless process is less than 100 times greater than the rate of spontaneous emission. For a radiative lifetime of 100 ns there is a time window of the order of 1 ns or longer in which the method described in this paper should work.

In a forthcoming report we will describe several extensions of our analysis, in particular the effects of wave packet spreading and interference. Our analysis of the variational problem will be expanded and the role of $a(t_1)$ will be discussed. We call attention to, and we will deal with, the fact that the definition of optimization (e.g., as the ratio or the difference in product fluxes) is a boundary condition that influences the solution of the variational problem.

ACKNOWLEDGMENTS

This research has been supported by grants from the NSF and the AFOSR. D. J. T. thanks Professor Jerry Bona for helpful conversations on the optimization problem.

APPENDIX A

In this Appendix we derive the optimum waveform for the stimulating pulse when there is a single final state ϕ_f of interest.

The second order amplitude for a transition from i to f, α_{fi}, is given by

$$\alpha_{fi} = \int_{-\infty}^{\infty}\int_{-\infty}^{t} \langle\phi_f|b(t)e^{-iH(t-s)/\hbar}a(s)|\phi_i\rangle ds\,dt\,. \quad (A1)$$

We wish to maximize $|\alpha_{fi}|^2$ with respect to the function $b(t)$, subject to the constraint

$$\int_{-\infty}^{\infty}|b(t)|^2dt = 1\,. \quad (A2)$$

Using the method of Lagrange multipliers, we rewrite Eq. (A1) as

$$I = |\alpha_{fi}|^2 = \left|\int_{-\infty}^{\infty}\int_{-\infty}^{t}\langle\phi_f|b(t)e^{-iH(t-s)/\hbar}a(s)|\phi_i\rangle ds\,dt\right|^2 + \lambda\left(\int_{-\infty}^{\infty}|b(t)|^2dt - 1\right), \quad (A3)$$

and we write

$$b(t) = \bar{b}(t) + \delta b(t)\,,$$
$$I = \bar{I} + \delta I\,, \quad (A4)$$

where $\bar{b}$ is the allowed functional form for b that optimizes I, namely $I = \bar{I}$. Substituting Eq. (A4) into Eq. (A3), and neglecting the second order terms in the variation δb, yields

$$\delta I = \alpha_{fi}^{*}\int_{-\infty}^{\infty}\int_{-\infty}^{t}\langle\phi_f|\delta b(t)e^{-iH(t-s)/\hbar}a(s)|\phi_i\rangle ds\,dt + \text{C.C.} + \lambda\int_{-\infty}^{\infty}(\bar{b}\delta b^{*} + \bar{b}^{*}\delta b)dt = 0\,. \quad (A5)$$

Equating the integrands of the integral over t and separating real and imaginary contributions, we obtain

$$\alpha_{fi}^{*}\int_{-\infty}^{t}\langle\phi_f|e^{-iH(t-s)/\hbar}a(s)|\phi_i\rangle ds = \alpha_{fi}^{*}f(t) = -\lambda b^{*}(t)\,, \quad (A6)$$

where we have defined

$$f(t) = \int_{-\infty}^{t}\langle\phi_f|e^{-iH(t-s)/\hbar}a(s)|\phi_i\rangle ds\,. \quad (A7)$$

Using the constraint (A2) we obtain

$$\bar{b}^{*} = \frac{\alpha_{fi}^{*}f(t)}{\left[|\alpha_{fi}|^2\int_{-\infty}^{\infty}|f(t)|^2dt\right]^{1/2}} = \frac{f(t)}{\left[\int_{-\infty}^{\infty}|f(t)|^2dt\right]^{1/2}}\,. \quad (A8)$$

This result states that the optimal stimulating waveform is matched to the convolution of the incident waveform with the dynamics on the excited state potential surface. Analogous conditions for optimization play an important role in communication theory where they form a part of matched filter theory.[3]

APPENDIX B

In this Appendix we solve for the optimal stimulating waveform when there is a sum or integral over final states of interest. Interference between different final states gives rise to a more interesting expression for the optimal waveform.

The expression we would like to maximize is

$$I_1 = \lim_{T\to\infty}\int_{-\infty}^{T}\int_{-\infty}^{t_2}\int_{-\infty}^{T}\int_{-\infty}^{t_2'} dt_2\,dt_1\,dt_2'\,dt_1' \times\langle g|e^{i\omega_g t_1}a(t_1)\mu e^{iH_{\text{ex}}(t_2-t_1)}b(t_2)\mu e^{-iH(T-t_2)}|P_1| \times e^{-iH(T-t_2')}b(t_2')\mu e^{-iH_{\text{ex}}(t_2'-t_1')}a(t_1')\mu e^{-i\omega_g t_1'}|g\rangle\,. \quad (B1)$$

The operator P_1 projects out of the total second order amplitude produced on the ground state potential surface that part which is located in exit channel (i). A similar projection operator can be defined for exit channel (ii). The phase factor $e^{i\omega_f t_2}$, which plays a trivial role when only a single final state is involved, must be replaced by the propagator corresponding to the ground state potential surface when many states are involved. This replacement accounts for the difference between the present expression and the single final state expression in Appendix A. It also motivates propagating classical trajectories on the ground state potential surface, as we do in the text.

We choose the same constraint as in Appendix A, namely,

$$\int_{-\infty}^{\infty}|b(t)|^2dt = 1\,. \quad (B2)$$

For ease of notation we define the function A by

$$A(t_2, t_1, t_2', t_1') = \lim_{T\to\infty}\langle g|e^{i\omega_g t_1}\mu e^{iH_{\text{ex}}(t_2-t_1)}\mu e^{-iH(T-t_2)}|P_1| \times e^{-iH(T-t_2')}\mu e^{-iH_{\text{ex}}(t_2'-t_1')}\mu e^{i\omega_g t_1'}|g\rangle\,, \quad (B3)$$

and

$$I_1 = \bar{I}_1 + \delta I_1\,,$$
$$b = \bar{b} + \delta b\,. \quad (B4)$$

Substituting Eq. (B3) and (B4) into Eq. (B1), and using the method of Lagrange multipliers, yields

$$\delta I_1 = \int_{-\infty}^{T}dt_2\int_{-\infty}^{t_2}dt_1\int_{-\infty}^{T}dt_2'\int_{-\infty}^{t_2'}dt_1'\,A(t_2, t_1, t_2', t_1') \times a^{*}(t_1)\delta b^{*}(t_2)a(t_1')\bar{b}(t_2') + \text{C.C.} + \lambda\int_{-\infty}^{T}dt_2[\bar{b}(t_2)\delta b^{*}(t_2) + \text{C.C.}]\,. \quad (B5)$$

Equating the integrands of the integrals over t_2, and separating real and imaginary components, gives the following equation for $\bar{b}(t)$:

$$\int_{-\infty}^{t_2}dt_1\int_{-\infty}^{T}dt_2'\int_{-\infty}^{t_2'}dt_1'\,A(t_2, t_1, t_2' t_1') \times a(t_1')\bar{b}(t_2')a^{*}(t_1) + \lambda\bar{b}(t_2) = \int_{-\infty}^{\infty}\bar{b}(t_2')A'(t_2', t_2)dt_2' + \lambda\bar{b}(t_2) = 0\,, \quad (B6)$$

where

$$A'(t_2', t_2) = \int_{-\infty}^{t_2} dt_1 \int_{-\infty}^{t_2'} dt_1' \, A(t_2, t_1, t_2', t_1') \times a(t_1') a^*(t_1) \,. \tag{B7}$$

Equation (B6) is an example of a Fredholm integral equation of the second kind. The eigenvalues of this equation are related to the Lagrange multiplier λ and the eigenfunctions are the desired optimal waveforms $\bar{b}(t)$.

[1] A. H. Zewail and N. Bloembergen, J. Phys. Chem. **88**, 5459 (1984).
[2] S. Y. Lee and E. J. Heller, J. Chem. Phys. **71**, 4777 (1979); **76**, 3035 (1982); E. J. Heller, Acc. Chem. Res. **14**, 368 (1981); J. Chem. Phys. **68**, 2066 (1978).
[3] See, for example, R. M. Fano, *Transmission of Information* (MIT, Cambridge, MA 1961).
[4] E. J. Heller, R. L. Sundberg, and D. J. Tannor, J. Phys. Chem. **86**, 1822 (1982).
[5] D. J. Tannor, S. A. Rice, and P. Weber, J. Chem. Phys. (to be published).

Coherent pulse sequence induced control of selectivity of reactions: Exact quantum mechanical calculations

David J. Tannor
The Department of Chemistry and The James Franck Institute, The University of Chicago, Chicago, Illinois 60637
Ronnie Kosloff
Fritz Haber Institute for Molecular Dynamics, Hebrew University, Jerusalem, Israel 91904
Stuart A. Rice
The Department of Chemistry and The James Franck Institute, The University of Chicago, Chicago, Illinois 60637

(Received 13 March 1986; accepted 3 July 1986)

We present a novel approach to the control of selectivity of reaction products. The central idea is that in a two-photon or multiphoton process that is resonant with an excited electronic state, the resonant excited state potential energy surface can be used to assist chemistry on the ground state potential energy surface. By controlling the delay between a pair of ultrashort (femtosecond) laser pulses, it is possible to control the propagation time on the excited state potential energy surface. Different propagation times, in turn, can be used to generate different chemical products. There are many cases for which selectivity of product formation should be possible using this scheme. We illustrate the methodology with numerical application to a variety of model two degree of freedom systems with two inequivalent exit channels. Branching ratios obtained using a swarm of classical trajectories are in good qualitative agreement with full quantum mechanical calculations.

I. INTRODUCTION

In a previous report we proposed a novel approach to achieving control of selectivity of reaction products.[1] The cases considered involved reaction on the ground electronic state potential energy surface, but mediated by excitation to, evolution on, and stimulated deexcitation from, an excited electronic state. In particular, our proposed methodology exploits the coherence properties of exciting and stimulating ultrashort pulses (femtosecond time scale), and the dynamics of wave packet evolution between exciting and stimulating pulses. The pulse shapes, durations, and separations required to achieve selectivity of product formation depend on the properties of the excited state potential energy surface. In the relevant time domain, which is defined by the shape of the excited state potential energy surface, it is possible to take advantage of the localization in phase space of the time dependent quantum mechanical amplitude and thereby carry out selective chemistry.

Our proposed method for achieving selectivity of reactivity owes a great debt to the pioneering work of Heller and co-workers,[2-8] who have reformulated the descriptions of a wide range of spectroscopies using an illuminating representation in terms of the evolution of wave packets. These descriptions have the advantage of avoiding explicit use of molecular eigenstates and Franck–Condon factors. The fact that the center of a wave packet evolves along a classical mechanical trajectory provides us with a valuable conceptual and calculational tool.

This paper reports the results of quantum mechanical calculations of the selectivity of reactivity possible with the Tannor–Rice scheme. Briefly put, it is assumed that the ground electronic state Born–Oppenheimer potential energy surface has two or more exit channels corresponding to the formation of two or more distinct chemical species.

It is also assumed that there exists an excited state potential energy surface whose minimum is displaced from that of the ground state surface and whose normal coordinates are rotated from those of the ground state surface (Duschinsky effect). This excited state potential energy surface is used to assist the chemistry on the ground state potential energy surface. The time spent on the excited state surface is used to select the desired chemical species. To see how this works, it is instructive to begin with a classical mechanical description of the dynamics. Consider the hypothetical potential energy surface shown in Fig. 1; it has a central minimum and two inequivalent exit channels separated from the minimum by saddle points. The trajectory that begins at rest at the minimum of the ground state surface is projected vertically up to the excited state surface (Fig. 2). It now evolves for some time on the excited state surface, after which it projected vertically back down to the ground state surface. The time spent on the excited state surface is one of the controllable variables in the Tannor–Rice scheme. The trajectory is now propagated on the ground state surface long enough to determine its ultimate fate, i.e., whether it leads to A + BC, AB + C, or ABC. Figure 3(a) shows a trajectory that exits from channel 1 (A + BC; excited state propagation time is 600 a.u.). Figure 3(b) shows a trajectory that exits from channel 2 (AB + C; excited state propagation time is 2100 a.u.). As may be seen in Figs. 4 and 5, in the classical mechanical description there are windows of 50–100 a.u. width for exit out of a desired channel.

The quantum mechanical description of the dynamics follows a very similar pattern. At the instant that the first photon is incident the ground state wave function makes a vertical (Franck–Condon) transition to the excited state surface. The ground state wave function is not a stationary state on the excited state potential energy surface, so it must evolve as t increases. There are some interesting analytical properties of this time evolution if the excited state surface is harmonic. In that case a Gaussian wave packet remains Gaussian for all time, the center of the Gaussian wave packet follows the classical trajectory for harmonic oscillation, both in coordinate and momentum space, and the Gaussian wave packet develops a phase equal to the classical action integral for the same motion, namely $\phi = \int_0^t (p\dot{q} - E)dt$. These properties are retained to a good approximation for smooth anharmonic potential energy surfaces. Moreover, Ehrenfest's theorem[9] ensures that the center of the wave packet will obey the classical equations of motion for any potential surface, provided the wave packet remains sufficiently localized. The duration of the propagation on the excited state surface can be regulated by the delay of a second pulse relative to the initial pulse of light. The second pulse leads to a vertical (Franck–Condon) transition down to the ground state surface. Note that the wave function amplitude is unchanged in the Franck–Condon transition. If the delay and width of the second pulse is chosen on the basis of the position and width of the windows in Fig. 2 it is plausible to expect the wave packet amplitude on the ground surface to select one channel over the other. In this paper we report the results of quantum mechanical calculations of wave packet propagation on the excited state and ground state potential energy surfaces, for a variety of different excited state potential energy surfaces and a range of pulse delays.

II. THEORY AND NUMERICAL TECHNIQUES

A. Second order time-dependent perturbation theory

The Hamiltonian we adopt is a 2×2 matrix of operators. It represents the ground and the excited electronic states within the Born–Oppenheimer approximation, coupled by the radiation field interacting with the transition dipole operators ($\mu = \mu_{ab} = \mu_{ba}$):

$$H = \begin{pmatrix} H_a & \mu E(t) \\ \mu E(t) & H_b \end{pmatrix}. \tag{1}$$

The time-dependent Schrödinger equation reads

$$i\hbar \frac{\partial}{\partial t} \begin{pmatrix} \psi_a \\ \psi_b \end{pmatrix} = \begin{pmatrix} H_a & \mu E(t) \\ \mu E(t) & H_b \end{pmatrix} \begin{pmatrix} \psi_a \\ \psi_b \end{pmatrix}. \tag{2}$$

At $t = 0$, $\psi_0 = \psi_a$, the ground vibrational state of H_a, so that

$$H_a \psi_0 = E_a \psi_0. \tag{3}$$

Also, $\psi_b = 0$ (we are assuming the system is at 0 K).

The two coupled differential equations in Eq. (2) can be transformed to two coupled integral equations, namely

$$\psi_a(t) = e^{(-iH_a t)/\hbar}\psi_a(0) - \frac{i}{\hbar}\int_{-\infty}^{t} e^{-i[H_a(t-t')]/\hbar}\mu E(t')\psi_b(t')dt', \tag{4a}$$

$$\psi_b = \frac{-i}{\hbar}\int_{-\infty}^{t} e^{-iH_b[(t-t')/\hbar]}\mu E(t')\psi_a(t')dt'. \tag{4b}$$

The reader may easily verify that Eqs. (4) are formal solutions of Eq. (2) by differentiation. We consider first the weak field regime.

The time-dependent perturbation theory expression for the second order amplitude on the ground state surface, $\psi_a^{(2)}(t)$, is

$$\psi_a^{(2)}(t) = \frac{-1}{\hbar^2}\int_{-\infty}^{t}\int_{-\infty}^{t_2} e^{-iH_a(t-t_2)/\hbar}\mu E(t_2)e^{-iH_b(t_2-t_1)/\hbar} \times \mu E(t_1)\psi_a(0)e^{-i\omega_a t_1}\,dt_1\,dt_2, \tag{5}$$

which expression may be obtained from Eqs. (4a) and (4b) by setting

$$\psi_b(t_2) = \frac{-i}{\hbar}\int_{-\infty}^{t_2} e^{-iH_b(t_2-t_1)/\hbar}\mu E(t_1)\psi_a(0)e^{-i\omega_a t_1}\,dt_1. \tag{6}$$

Note that Eq. (5) contains the field strength to second order only. Equation (5) has the following simple interpretation: $\psi_a(0)$ evolves on the ground state surface from $t = 0$ until $t = t_1$. At time t_1 it makes a vertical transition to the excited state surface. The wave function propagates on the excited state surface from time t_1 until time t_2. At time t_2 the wave function makes a vertical transition back to the ground state surface. The wave function then evolves on the ground state surface from time t_2 until time t. In general, the waveforms $E(t_1)$, $E(t_2)$ are extended; therefore we must integrate over t_1 and t_2, all the instants at which the transition up and the transition down may take place. The probability S for exit from channel 1 is

$$S_1 = \lim_{t\to\infty} \langle \psi_a(t)|P_1|\psi_a(t)\rangle, \tag{7}$$

where P_1 is a projection operator in coordinate space corresponding to channel 1 and S_2 is given similarly.

B. Numerical wave packet propagation

The wave packet propagation procedure used is an adaptation of several existing grid methods.[10–12] The wave functions on the ground and excited state surfaces are discretized: They are represented by their values at a set of 64×64 or 128×128 grid points. The grid we use is a rectangular lattice in bond length coordinates R_1 and R_2 and chosen to encompass the coordinate space region of interest: The bound region and the adjacent portion of the two exit channels on the ground state surface. The region on the excited state surface involves the identical portion of coordinate space. This propagation method is in principle exact, as the grid is allowed to extend to infinity and the grid point spacing and time step (see below) are reduced to zero.

To calculate the time evolution of the wave function, it is first necessary to evaluate $H\psi$. In Eq. (2), for example, the diagonal part of the matrix multiplication is given by

$$H_a\psi_a = \left[-\frac{\hbar^2}{2m}\left(\frac{\partial^2}{\partial x^2} + \frac{\partial^2}{\partial y^2}\right) + V_a(x,y)\right] \times \psi_a(x,y) = [T + V_a]\psi_a, \tag{8}$$

and similarly for $H_b\psi_b$. $V_a\psi_a$ is evaluated simply by multiplication at each of the discrete grid points. $T\psi_a$ is evaluated by the Fourier transform method. $\psi_a(x,y)$ is Fourier transformed to $\psi_a(k_x,k_y)$, then multiplied by $-\hbar^2/2m(k_x^2+k_y^2)$, and the product is inverse Fourier transformed. This procedure has several distinct advantages over the finite difference method for evaluating $T\psi$, as described in Ref. 11. In particular, it preserves the quantum mechanical commutation relation

$$[p,f(x)] = i\hbar f(x). \tag{9}$$

Moreover, the error in calculation decreases exponentially with the number of grid points for Gaussian wave functions. The grid spacing Δx is chosen such that (atomic units)

$$\Delta x < 1/p_{x,\max}. \tag{10}$$

Our $\Delta x = 0.1$, $\Delta y = 0.05$, where x and y are mass-skewed coordinates. Convergence of the branching ratio (see below) with respect to grid size, was spot checked and found to be $\sim 1\%$. $H_b\psi_b$ is evaluated in the same way. The off-diagonal elements, $\mu E(t)\psi_a$ for example, are evaluated simply by multiplication. It is clear that a coordinate dependence to $\mu\,[\mu = \mu(x,y)]$ could be introduced easily. However, in our calculation μ is taken to be a constant (Condon approximation).

Given $H\psi$ how do we construct $e^{-iH\Delta t/\hbar}\psi(t)$? We have used the method of second order differencing, which starts from

$$\psi(t+\Delta t) = e^{-iH\Delta t}/\hbar = \left(1 - \frac{iH\Delta t}{\hbar} + \cdots\right)\psi(t). \tag{11a}$$

$$\psi(t-\Delta t) = e^{iH\Delta t}/\hbar = \left(1 + \frac{iH\Delta t}{\hbar} + \cdots\right)\psi(t). \tag{11b}$$

and by addition generates

$$\psi(t+\Delta t) \simeq \psi(t-\Delta t) - 2\,\frac{i\Delta tH}{\hbar}\,\psi(t). \tag{12}$$

This procedure preserves norm and energy. The error is of order Δt^3. The stability limit for Δt is

$$\Delta t_{\text{stab}} = 1/E_{\max}, \tag{13}$$

where

$$E_{\max} = V_{\max} + \frac{p_{\max}^2}{2m}. \tag{14}$$

In practice $\Delta t_{\text{stab}}/5$ is used. Our Δt was 0.4 a.u. Convergence of the branching ratio with respect to time step was spot checked and found to be $\sim 1\%$. The equations actually used in our calculation are [cf. Eq. (2)]

$$\psi_a(t+\Delta t) = \psi_a(t-\Delta t) - \frac{2i}{\hbar}\,\Delta t H_a\psi_a(t) - \frac{2i}{\hbar}\,\Delta t\mu E\cos\omega t\psi_b(t), \tag{15a}$$

$$\psi_b(t+\Delta t) = \psi_b(t-\Delta t) - \frac{2i}{\hbar}\,\Delta t H_b\psi_b(t) \times \frac{-2i}{\hbar}\,\Delta t\mu E\cos\omega t\psi_a(t), \tag{15b}$$

with $H\psi$ evaluated as described above.

III. RESULTS

We show below results for four different model systems. All the systems use the same ground state potential energy surface (Fig. 1), but different excited state potential energy surfaces. All the surfaces are models for the coupled symmetric and asymmetric stretch vibrations in a collinear molecule. The masses for the system are 1823, 1823, and 3646 a.u., corresponding to HHD. Although the ground state potential energy surface of true HHD is not bound there are excited electronic states which are bound. Our primary reason for choosing hydrogenic masses was to facilitate the quantum mechanical calculations, which are substantially more difficult for heavier masses. In general, one expects the classical–quantum correspondence, upon which our selectivity scheme is based, to improve for larger masses.

Excited surface I is harmonic and Duschinsky rotated relative to the ground state surface. In this case, because the potential energy surface is harmonic, the wave packet on the excited state will not break up. Indeed, we observe excellent selectivity for this model: For one choice of delay time between pulses we generate an exit from channel 1, while with a second delay time we generate an exit from channel 2.

The second through fourth examples include a variety of anharmonic excited state potential energy surfaces.

Model II has a very broad and shallow excited state potential energy surface. It was initially believed that use of this surface as an intermediary would favor slow alternation (as a function of pulse delay) in the flux out of channel 1 or channel 2 because of the low antisymmetric stretch frequency. We find, instead, that wave packet spreading is particularly dramatic in this example because of the flatness of the surface.

Model III has a "typical" anharmonic potential energy surface, with frequencies approximately commensurate with those on the ground state surface. This model was intended to represent the case in which the wave packet stays close to the harmonic region of the excited state potential energy surface, and thus reasonably well localized. In fact, as will be seen, the wave packet spreading is pronounced. In model IV the excited state potential energy surface is taken to have shorter bond lengths than the ground state surface. The difference in bond lengths leads to a variety of effects not seen with the other potential energy surfaces since the initial transition is to the soft part of Morse potential, while the second transition (depending on the instant) is to the strongly repulsive part of the Morse potential. This model was designed to explore the possibility of the wave packet returning to the original potential energy surface with a great deal of potential energy, which could be converted to the kinetic energy required for dissociation. A related feature is that there is dramatic wave packet contraction, or focusing, as the wave packet evolves on the excited state surface from the soft to the hard part of the potential.

An excited state potential energy surface with shorter equilibrium bond lengths, deeper wells, and/or higher barriers than those the ground state potential energy surface proved to be the most useful intermediary for this selectivity of reactivity scheme. Although these changes in molecular parameters on excitation are not common, there are cases for

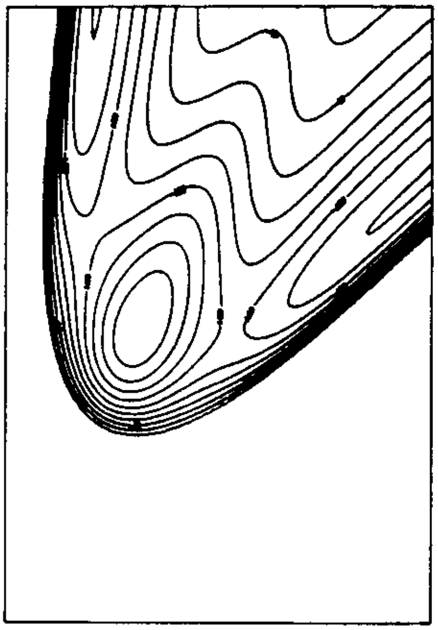

FIG. 1. Model ground state Born–Oppenheimer potential energy surface.

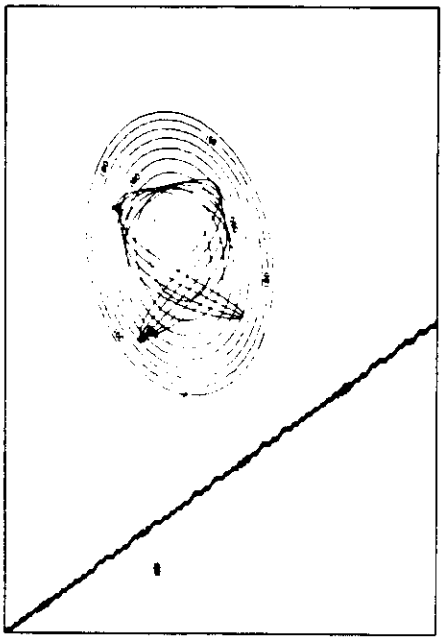

FIG. 2. Harmonic excited state Born–Oppenheimer potential energy surface. The classical trajectory that originates at rest from the ground state equilibrium geometry is shown superimposed.

which they occur. Alternatively, one may use our scheme with the roles of excited state and ground state reversed. Consider starting out in the ground vibrational state of the excited electronic state. This is the initial condition for ordinary emission spectroscopy. Then one may use a two pulse sequence to stimulate amplitude down to the ground electronic state and back up to the original electronic state. Now the steepness of the *ground* state surface barriers accelerate the nuclear motion so that enough kinetic energy is acquired for dissociation on the *excited* state surface; also the tighter bonds on the ground state serve to focus the wave packet. In short, vibrational energy acquired on the steeper of the two potential energy surfaces may be used to break a bond on the flatter of the two potential energy surfaces.

Figure 1 shows the ground state potential energy surface, which is of the Wall–Porter form,[13]

$$V_g = D(\theta)\{(1 - e^{\beta(\theta)[l - l_{eq}(\theta)]})^2 - 1\}. \qquad (16)$$

This potential energy surface is common to models I–IV. The variables l and θ are the polar coordinate counterparts of R_1 and R_2, the bond length coordinates; l is the length from a remote "swing point" and θ the "swing angle" about this swing point. The three parameters of the Morse potential—the dissociation energy, the equilibrium position, and the force constant—are taken to be functions of θ. This form makes adjustment of local features of the potential energy surface very easy, and was conducive to the systematic study of the influence of particular features of the potential energy surface on selectivity of reactivity. The details of the transformation between coordinate systems and the functional forms for $D(\theta)$, $l_{eq}(\theta)$, and $\beta(\theta)$ may be found in Table I.

TABLE I. $V(l,\theta) = D(\theta)(1 - e^{+\beta(\theta)(l - l_{eq}(\theta))})^2 + V_0$, $D(\theta) = D_0 - D_1 H_2(\theta) e^{-(\theta - \pi/4)^2/2\sigma_D^2}$, $\beta(\theta) = \beta_0 - \beta_1 e^{-(\theta - \pi/4)^2/2\sigma_\beta^2}$, $l_{eq}(\theta) = l_0 + l_1 e^{-(\theta - \pi/4)^2/2\sigma_l^2}$, $H_2(\theta) = 4(\theta - \pi/2)^2/\sigma_D^2 - 2$.

Surface	D_0	D_1	σ_D^2	β_0	β_1	σ_β^2	l_0	l_1	σ_l^2	V_0
Ground	0.1705	0.019 12	0.007 615	1.0584	0.3334	0.043 86	8.045	2.823	0.0685	0
II	0.1705	0.019 12	0.42	1.0584	0.6334	0.343 86	7.295	2.823	0.0685	0.06
III	0.1705	0.019 12	0.035	1.0584	0.3334	0.043 86	7.295	2.823	0.0685	0.06
IV	0.1705	0.019 12	0.035	1.0584	0.3334	0.043 86	8.670	2.823	0.0685	0.06

$0 < \theta < \pi/2$
$R_1 = -l\cos\theta + 10$
$R_2 = -l\sin\theta + 10$
$x = 2^{-1/2}R_1$
$y = R_2 + \frac{1}{2}R_1$
All units atomic units

Surface I (harmonic) is given by $V(x,y) = \frac{1}{2}(x,y)\begin{pmatrix} V_{xx} & V_{xy} \\ V_{yx} & V_{yy} \end{pmatrix}\begin{pmatrix} x \\ y \end{pmatrix} + V_0$

$V_{xy} = 0.3898$
$V_{xy} = 0.0430 = V_{yx}$
$V_{yy} = 0.18$
$V_0 = -0.14$

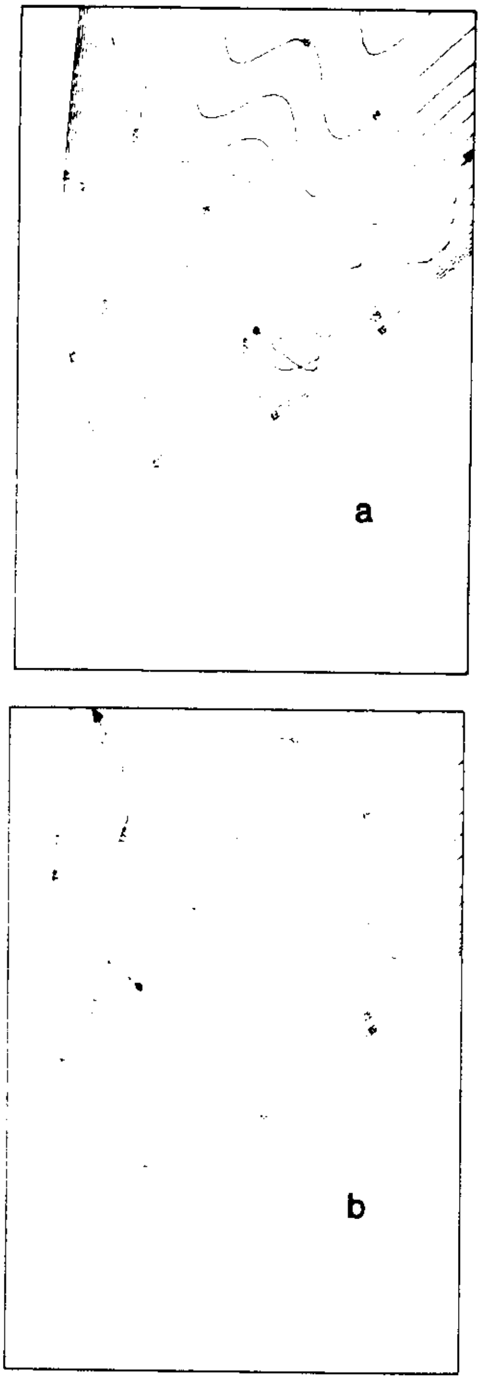

FIG. 3. Classical trajectories on the ground state surface that arise from a vertical transition down (coordinates and momentum unchanged) after propagation time $t_2 - t_1$ on the excited state potential energy surface. (a) $t_2 - t_1 = 600$ a.u., (b) $t_2 - t_1 = 2100$ a.u.

The well depth is -0.208 a.u. and the two frequencies about the center of the well are $\omega_1 = 0.009$ a.u. and $\omega_2 = 0.016$ a.u. The heights of the two saddle points are -0.1480 a.u. The well depths of the exit channels are -0.1705 a.u. and the asymptotic vibrational frequencies, based on H_2 and HD, are $\omega_{H_2} = 0.020$ a.u. and $\omega_{HD} = 0.017$. The coordinates of the ground state minimum are $x_0 = 1.63$, $y_0 = 3.47$.

In model I the excited state potential energy surface is taken to be harmonic. The parameters for this surface are also given in Table I. The excited state frequencies are given by

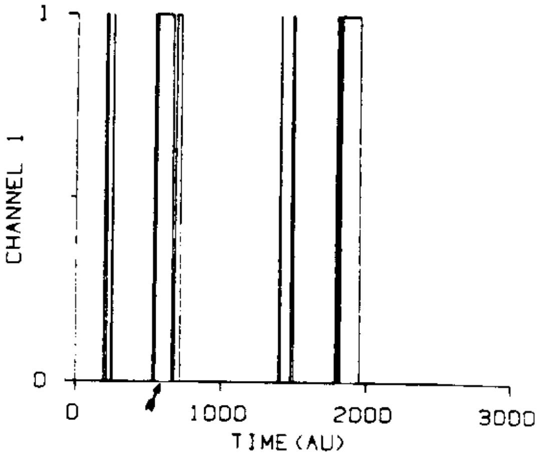

FIG. 4. Probability (0 or 1) of exit from channel 1 as a function of excited state potential energy surface propagation time.

$$\omega_1' = 0.0148 \text{ a.u.}, \quad \omega_2' = 0.0097 \text{ a.u.} \tag{17}$$

The coordinates of the excited state minimum are $x_0 = 2.02$ and $y_0 = 4.30$. The excited state potential energy surface is shown in Fig. 2. In accord with the Franck–Condon principle (and assuming a coordinate independent transition moment) the wave function is identical in position and shape with the wave function in Fig. 1. Figure 2 also displays the unique classical trajectory on the excited state that originates at rest from the ground state equilibrium geometry. Note the Lissajous motion that arises from the Duschinsky rotation. Figures 3(a) and 3(b) show the classical trajectories on the ground state potential energy surface that arise from a vertical transition down (coordinates and momenta unchanged) after propagation times of 600 and 2100 a.u. on the excited state surface, respectively. The trajectory in Fig. 3(a) dissociates out channel 1, and that in Fig. 3(b) dissociates out channel 2. Clearly, there is a continuum of trajectories, on the ground state potential energy surface, corresponding to the continuum of instants at which the vertical

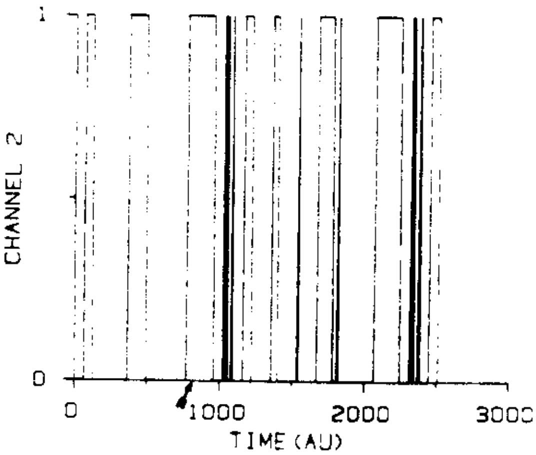

FIG. 5. Same as Fig. 4 only for channel 2. Note that there is no overlap between the windows in Figs. 4 and 5, but there are time intervals that correspond to bound trajectories on the ground state potential energy surface that appear as zero amplitude in both plots.

TABLE II. $\mu E(t) = A(t)\cos(\omega_e t) + B(t)\cos(\omega_d t) = A\, e^{-(t-t_e)^2/2\sigma_e^2} \times \cos(\omega_e t) + B\, e^{-(t-t_d)^2/2\sigma_d^2} \cos(\omega_d t)$.

Surface		A	B	t_e	t_d	σ_e	σ_d	ω_e	ω_d
I	(i)	0.125	0.125	30	630	10	10	0.1618	0.1618
	(ii)	0.125	0.125	30	855	10	30	0.1618	0.0618
II		0.125	0.125	30	1000	10	10	0.10	0.10
III		0.125	0.125	30	760	10	10	0.180	0.180
IV	(i)	0.125	0.125	30	610	10	10	0.10	0.10
	(ii)	0.125	0.125	30	1010	10	10	0.10	0.10

transition down takes place, and Figs. 3(a) and 3(b) simply are meant to be illustrative. The fate with respect to dissociation of the entire continuum of trajectories is displayed in Figs. 4 and 5. Figure 4 shows the probability (0 or 1) of exiting from channel 1 as a function of propagation time on the excited state potential energy surface. Figure 5 is the corresponding plot referred to channel 2. Dissociation is defined as $\theta < 0$, $p_\theta < 0$ for channel 1 and $\theta > \pi/2$, $p_\theta > 0$ for channel 2. It is clear that Figs. 4 and 5 have no overlap with each other; the definitions of dissociation are exclusive. Those time intervals that take on the value of 0 for both exit channels correspond to trajectories trapped in the bound region of the potential energy surface.

We now exploit the dissociation windows in Figs. 4 and 5 to choose a suitable pulse sequence for quantum mechanical calculations. We choose

$$\mu E(t) = A(t)\cos(\omega_e t) + B(t)\cos(\omega_d t), \tag{18}$$

where $A(t)$ and $B(t)$ are Gaussian pulses, with a delay between them chosen on the basis of the classical windows. The parameters of the pulse sequence are given in Table II. The pulse delay $t_d - t_e = 600$ a.u. was chosen to correspond to the broad window in Fig. 4 of $t_2 - t_1 = 600$ a.u. The first pulse was deliberately chosen to be very narrow in time so the wave function on the excited state closely approximates the initial state. The values for A and B were chosen so that

$$\int_{-\infty}^{\infty} A(t)dt = \pi \tag{19a}$$

and

$$\int_{-\infty}^{\infty} B(t)dt = \pi. \tag{19b}$$

Figures 6(a)–6(c) represent the excited state wave function at $t = 200$, 400, and 600 a.u., before the second pulse. (In this figure, as in all subsequent figures, it is the magnitude of the wave function which is plotted.) Note how the wave packet tracks the classical trajectory [Fig. 3(a)]. Figures 7(a)–7(c) show the ground state wave function at $t = 0$, 800, and 1000 a.u. Although not all the amplitude exits to form product, that amplitude which does exit leaves virtually completely from channel 1. Apparently, as long as the vertical transition back to the ground state surface is timed to be close enough to a classical exit window, much of the wave packet amplitude on the ground state will exit.

We now want to establish that use of a different delay time from that cited in the last paragraph will lead to amplitude exiting exclusively from channel 2. The new delay and width were suggested by the exit window in Fig. 5 centered at $t = 825$ a.u. Parameters for the second pulse sequence are given in Table II. Figure 8 shows the excited state wave function at $t = 800$ a.u., before the second pulse. As before, the wave packet motion tracks the classical trajectory that has propagated for the same length of time.

Figures 9(a)–9(c) show the ground state wave function at $t = 0$, 1000, and 1200 a.u. As before, although most of the amplitude remains in the bound region, the amplitude that does exit does so exclusively from channel 2.

Results very similar to those displayed in Figs. 6–9 were obtained by implementing the perturbation theory formula, Eq. (5), valid for $A, B < 0.01$. Contour plots of $\psi_0^{(2)}(t)$, the second order perturbation to the ground state wave function,

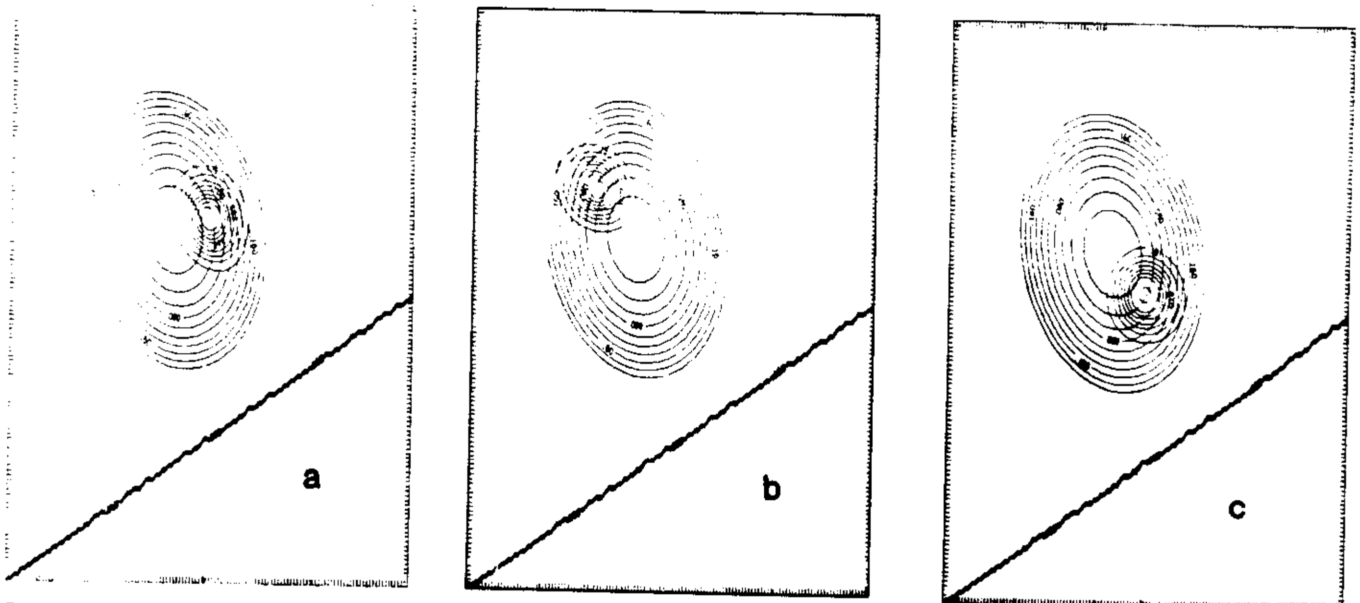

FIG. 6. Magnitude of the excited state wave function for the pulse sequence described in the text (pulse delay = 600 a.u., $A = B = 0.125$). (a) $t = 200$ a.u., (b) $t = 400$ a.u., (c) $t = 600$ a.u. Note the agreement with the results obtained for the classical trajectory (Fig. 2).

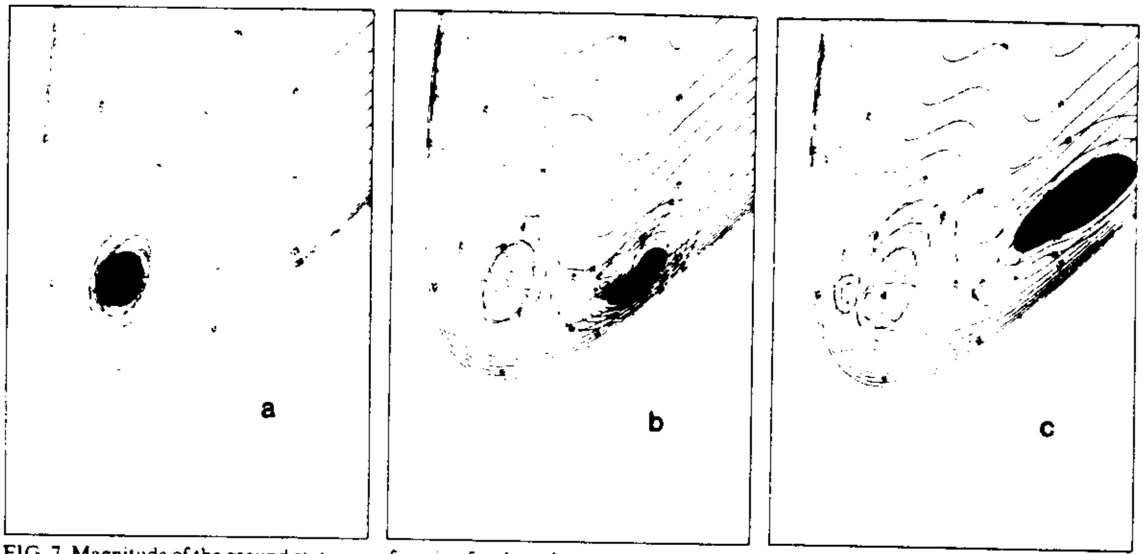

FIG. 7. Magnitude of the ground state wave function for the pulse sequence in Fig. 6. (a) $t = 0$, (b) $t = 800$ a.u., (c) $t = 1000$ a.u. Note the agreement with the results obtained for the classical trajectory [Fig. 3(a)]. Although some of the amplitude remains in the bound region, that which does exit does so exclusively from channel 1.

look remarkably similar to the contour plots of $\psi_a(t)$ in the case of stronger fields (Figs. 7 and 9). However, the plot of the exact $\psi_a(t)$ in the weak field case is not very dramatic; it is hard to see the amplitude which is exiting unless the bound amplitude is filtered. Nevertheless, the amplitude can be detected and the weak field case may be experimentally more accessible than is the strong field case.

The second example (surface II) shows that the simple pump–stimulate sequence does not always work. We use the same ground state potential energy surface as previously (Fig. 1). The excited state potential energy surface is anharmonic and, like the ground state surface, of the Wall–Porter form [Eq. (16)]. The parameters for the surface are given in Table I.

Equipotential contours for the excited state surface are shown in Fig. 10(a). As before, we show the initial vibrational wave function as well as the classical trajectory on the excited state surface which originates from rest on the ground state surface. Figures 10(b) and 10(c) summarize the ground state trajectory dissociation times in the form of window plots. As before, the window plots are based on a unique classical trajectory on the excited state potential energy surface.

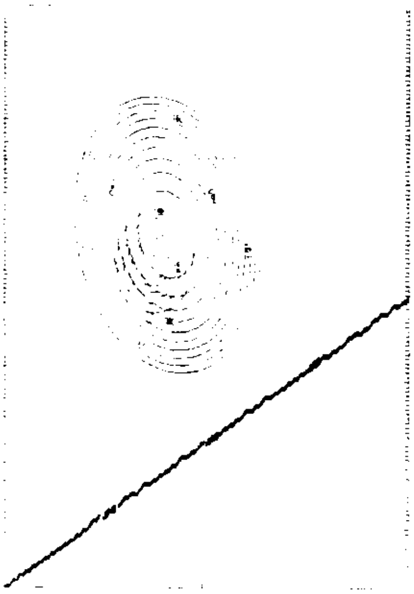

FIG. 8. Magnitude of the excited state wave function at $t = 800$ a.u., for the second pulse sequence described in the text (pulse delay = 825 a.u., $A = B = 0.125$). The excited state wave function at $t = 200$, 400, and 600 a.u. is virtually identical to that in Figs. 6(a)–6(c).

The parameters for the pulse sequence are given in Table II. The delay time was chosen to coincide with the broad classical window for channel 1 at $t = 1000$ a.u. Figures 11(a)–11(c) show the excited state wave function at $t = 200$, 600, and 800 a.u., respectively, before the second pulse. Clearly, the quantum mechanical amplitude is spreading severely. Figure 11(d) shows the amplitude on the ground state surface at $t = 1200$ a.u., after the second pulse. The poor selectivity is apparent from the figure.

The failure to achieve selectivity in this model system can be traced to the dynamics on the anharmonic excited state surface, and in particular the wave packet bifurcation. This observation motivated us to explore systematically the features of the excited potential energy state surface and excited state wave packet dynamics that are compatible with the proposed selectivity scheme. The next several examples explore the behavior induced by a variety of anharmonic excited state potential energy surfaces.

Model III has a "typical" excited state potential energy surface. Specifically, the excited state minimum is displaced to larger distance relative to the ground state minimum, the frequencies in the symmetric and asymmetric stretch coordinates are roughly equal, and the force constants are in the same range as their ground state values. The excited state surface is of the Wall–Porter form [Eq. (16)]; the parameters are given in Table I.

Equipotential contours for the excited state surface shown in Fig. 12(a). Figures 12(b)–12(c) summarize the ground state trajectory dissociation times in the form of window plots, based on a unique trajectory on the excited state potential energy surface.

Parameters for the pulse sequence are given in Table II.

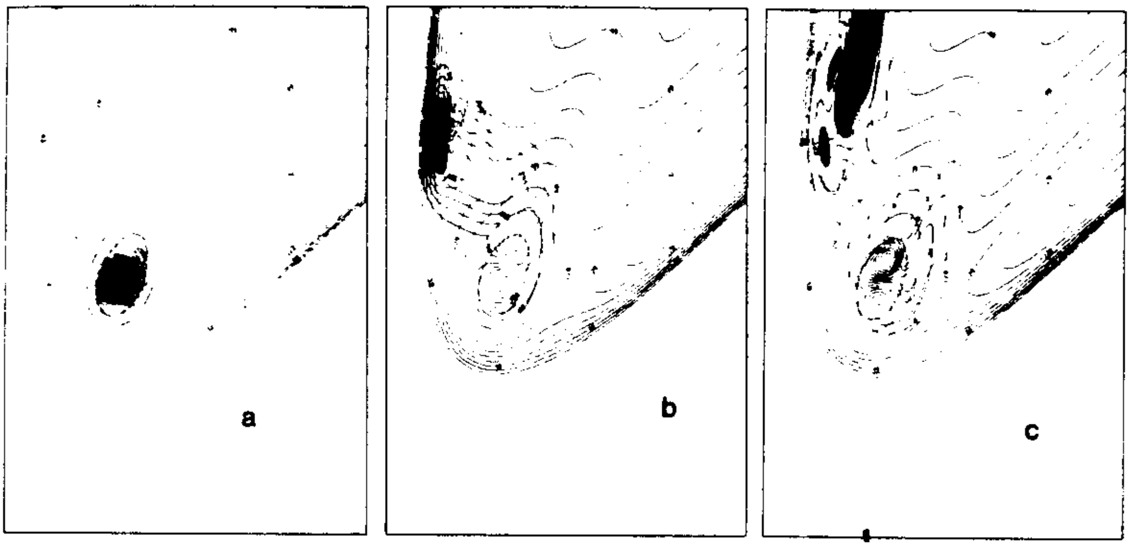

FIG. 9. Magnitude of the ground state wave function for the pulse sequence in Fig. 8. (a) $t = 0$, (b) $t = 1000$ a.u., (c) $t = 1200$ a.u. That amplitude which does exit does so exclusively from channel 2.

The delay time was chosen to coincide with the classical window for channel 1 at $t = 730$ a.u. Figures 13(a)–13(c) show the excited state wave function at $t = 200$, 400, and 600 a.u., respectively, before the second pulse. Again, the quantum mechanical amplitude is spreading severely, as the wave packet migrates toward the soft part of the Morse potential. Figure 13(d) shows the amplitude on the ground state surface at $t = 1000$ a.u., after the second pulse. The selectivity out of channel 2 is virtually complete (no amplitude exits from channel 1). This result was unexpected: The classical window predicts an exit from channel 1.

Model IV also has an anharmonic excited state potential energy surface of the Wall–Porter form; the parameters are given in Table I. The special feature of this excited state surface is that the excited state minimum is displaced to *smaller* distance than the ground state minimum.

Equipotential contours for the excited state surface are shown in Fig. 14(a). As before, we show the initial vibrational wave function as well as the unique classical trajectory on the excited state surface which originates from rest on the

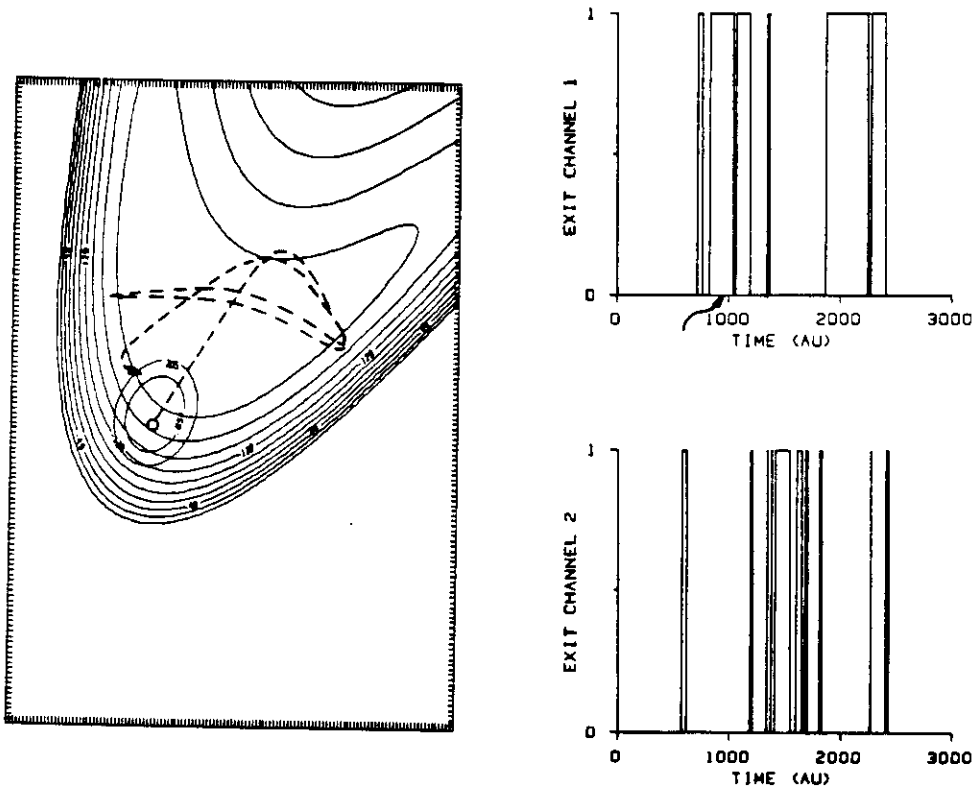

FIG. 10. (a) Anharmonic excited state potential energy surface (II in the Table). The classical trajectory that originates from rest from the ground state equilibrium geometry is shown superposed. (b) Probability (0 or 1) of exit from channel 1 as a function of excited state propagation time. (c) Same as (b) only for exit channel 2.

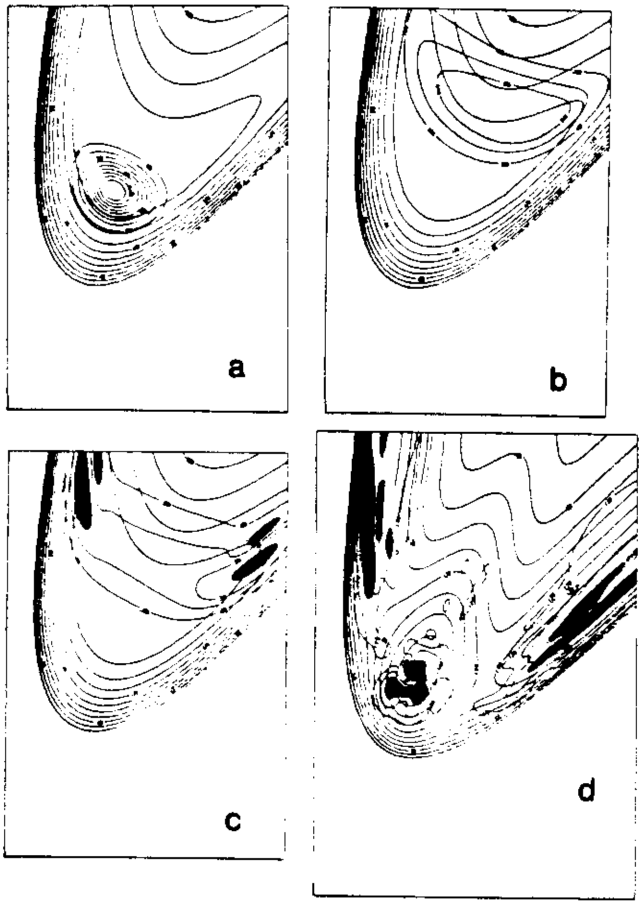

FIG. 11. Magnitude of the excited state wave function before the second pulse. (a) $t = 200$ a.u., (b) $t = 600$ a.u., (c) $t = 800$ a.u. Note the extensive wave packet spreading because the surface is so flat. This spreading will undermine the selectivity of products. (d) Ground state wave function at $t = 1200$ a.u., after the second pulse. The poor selectivity of products is apparent.

ground state surface. The first pulse sequence examined was at $t = 30$, 610 a.u. Additional parameters for the pulse sequence are given in Table II. Figures 15(a)–15(c) show the excited state wave function at $t = 200$, 400, and 600 a.u., respectively, before the second pulse. The wave packet begins on the soft part of the Morse potential, and initially begins to spread. However, as the wave packet migrates to the hard part of the Morse it contracts very dramatically. Figures 15(d)–15(f) show the amplitude on the ground state surface at $t = 800$, 1000, and 1200 a.u., respectively, after the second pulse. It is apparent that a substantial fraction of wave packet amplitude exits from channel 2, while virtually no amplitude exits from channel 1.

The next pulse sequence examined was at $t = 30$, 1010 a.u. Additional parameters for the pulse sequence are given in Table II. Figures 16(a) and 16(b) show the excited state wave function at $t = 800$ and 1000 a.u., respectively, before the second pulse. Figures 16(c)–16(e) show the amplitudes on the ground state surface at $t = 1200$, 1400, and 1600 a.u., respectively, after the second pulse. The wave packet breaks up on the ground state surface with roughly equal amplitudes escaping from channel 1 and channel 2.

Figure 17 shows the quantum branching ratio as a function of stimulation time, for stimulating pulses centered 200 a.u. apart, from 210 to 1010 a.u. The branching ratio was defined as the magnitude squared of the normalized wave function which was beyond a critical value of θ: (channel 1: $\theta > 1.17$, channel 2: $\theta < 0.4$). Note the dramatic differences between the branching ratios at different times relative to each other as well as relative to the amplitude that remains bound.

It was necessary to make some qualitative judgments to obtain the values of the branching ratios shown in Fig. 17. Typically, the probabilities of reaction to form products

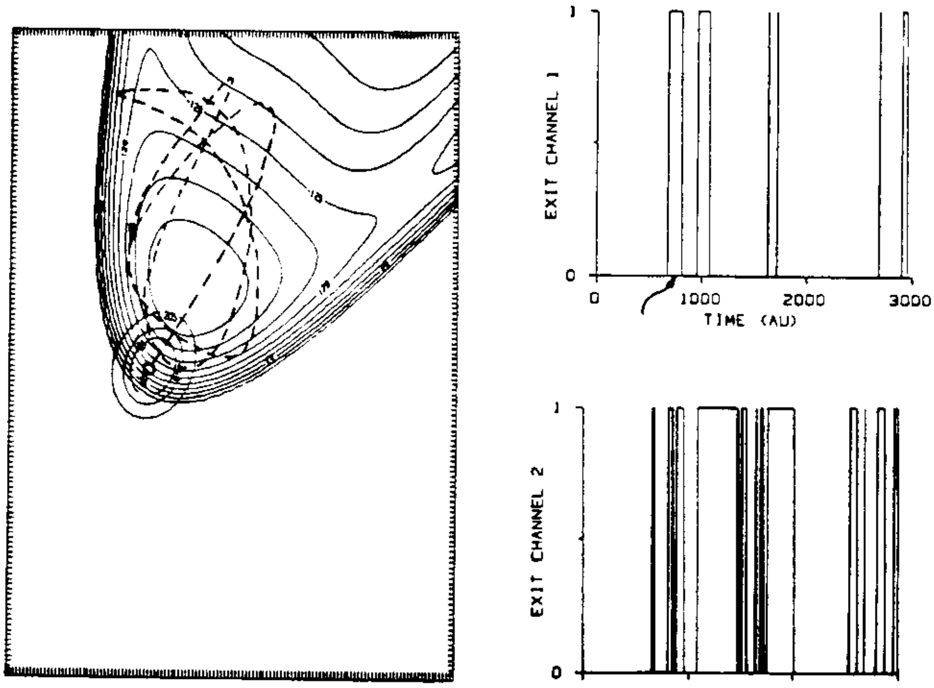

FIG. 12. (a) Anharmonic excited state potential energy surface (III in the Table). The classical trajectory that originates from rest from the ground state equilibrium geometry is shown superposed. (b) Probability (0 or 1) of exit from channel 1 as a function of excited state propagation time. (c) Same as (b) only for exit channel 2.

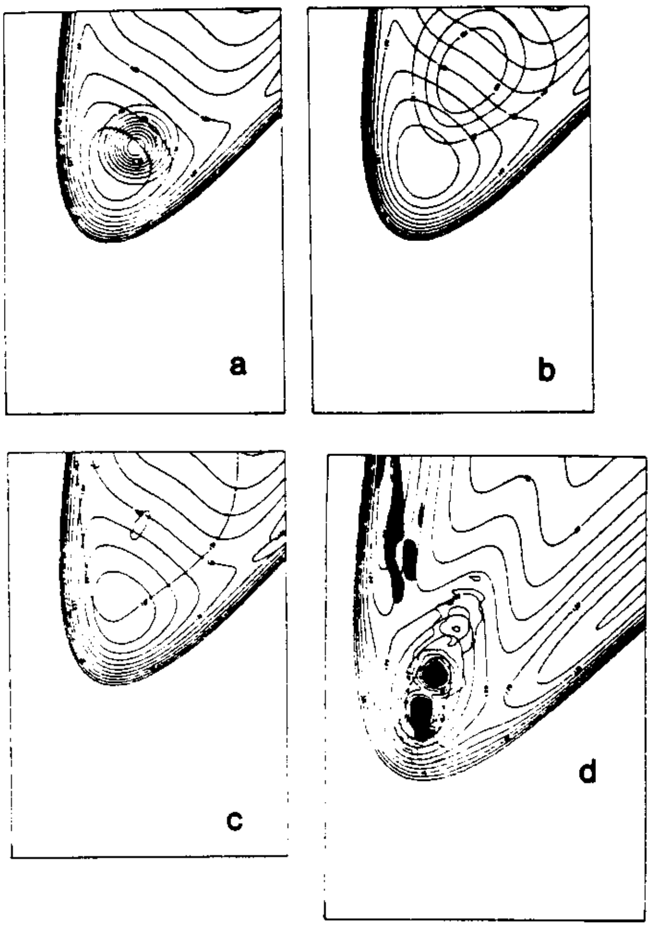

FIG. 13. Magnitude of the excited state wave function before the second pulse. (a) $t = 200$ a.u., (b) $t = 400$ a.u., (c) $t = 600$ a.u. Note the wave packet spreading is still significant, as the wave packet approaches the soft part of the Morse potential. (d) Ground state wave function at $t = 1000$ a.u., after the second pulse. There is complete selectivity out of channel 2, while the classical mechanics predicts selectivity for exit out of channel 1.

achieve a sensibly constant value 1000 to 2000 a.u. after the stimulated emission pulse. For longer time the calculated probabilities of reaction slowly decreased, which is an artifact due to reflection off the boundaries of our grid. The time at which the decrease starts can be different for the different products, so the asymptotic branching ratio was sometimes evaluated by picking values for the two "asymptotic" probabilities of product formation at somewhat different times. In a few cases the probabilities of reaction had not yet reached constant values when the calculation was stopped, possibly because for these pulse sequences dynamical tunneling contributes to the reaction. In each such case the branching ratio is marked with an asterisk.[14]

An initial classical study of this system using the unique classical trajectory on the excited state surface failed to reproduce many of the qualitative features of Fig. 17. A single classical trajectory cannot exhibit the tendency of the quantum wave packet to bifurcate. Moreover, the single trajectory we used had no zero point energy. We, therefore, examined a swarm of trajectories with an initial Gaussian distribution in p and x:

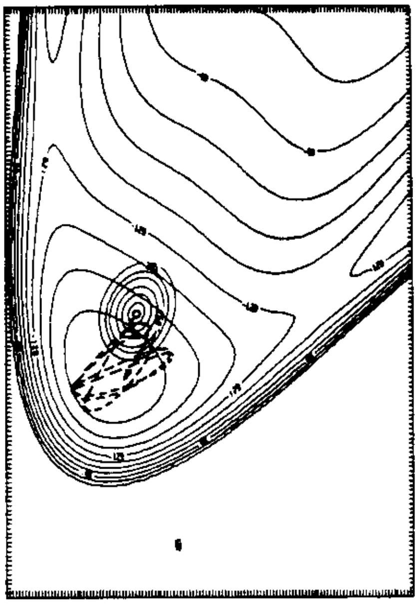

FIG. 14. Anharmonic excited state potential energy surface (IV in the Table). The classical trajectory that originates from rest from the ground state equilibrium geometry is shown superposed.

$$P(\mathbf{x},\mathbf{p}) = \left(\frac{1}{\pi\hbar}\right)^2 \exp\left(-\left[\frac{m\omega_1 x_1^2}{\hbar} + \frac{m\omega_2 x_2^2}{\hbar} + \frac{p_1^2}{m\omega_1\hbar} + \frac{p_2^2}{m\omega_2\hbar}\right]\right). \tag{20}$$

This distribution corresponds to the Wigner transform of the ground vibrational state of the ground state potential energy surface[14] where the ground state surface is expanded up to quadratic terms about the equilibrium geometry. This distribution was discretized with 81 sets of $\mathbf{p},\mathbf{x}$ initial conditions in the following way:

$$p_{1,0} = -(m\omega_1)^{1/2}(j_1 - 2)/1.2,$$
$$p_{2,0} = -(m\omega_2)^{1/2}(k_1 - 2)/1.2,$$
$$x_{1,0} = (m\omega_1)^{-1/2}(j_2 - 2)/0.25,$$
$$x_{2,0} = (m\omega_2)^{-1/2}(k_2 - 2)/0.25,$$
$$j_1,k_1,j_2,k_2 = 1,3,$$
$$m = 1823 \text{ a.u.},$$
$$\omega_1 = 0.016\,155 \text{ a.u.},$$
$$\omega_2 = 0.009\,281 \text{ a.u.}$$

x_1,x_2 are the ground state normal mode coordinates, p_1,p_2 the conjugate momenta, and ω_1,ω_2 the normal mode frequencies. The initial distribution in coordinate space is shown in Fig. 18. There are nine initial values for $\mathbf{p}$ corresponding to each initial value for $\mathbf{x}$. We point out that since the initial conditions for $\mathbf{p}$ and $\mathbf{x}$ are independent there is a range of zero point energies in the swarm. Several swarms of 625 trajectories were propagated and the branching ratios compared with those for swarms of 81 trajectories. The results agreed to ~5% in units of product formed.

Figures 19(a)–19(c) shows the swarm on the excited state potential energy surface, for the same pulse sequence as Fig. 15 (second pulse at 610 a.u.). The swarm mimics close-

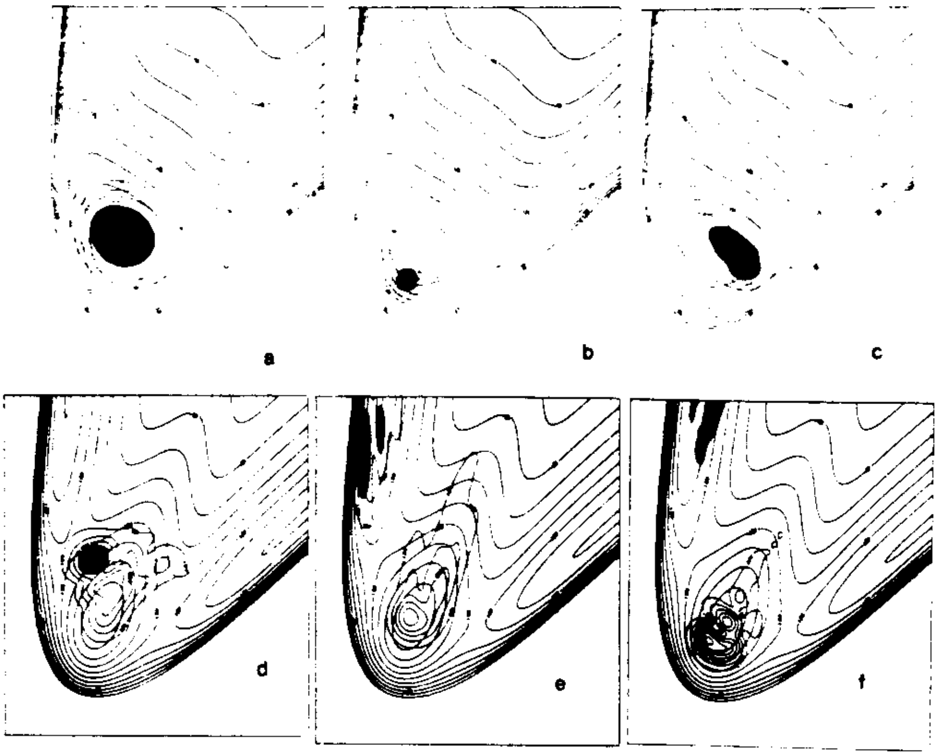

FIG. 15. Magnitude of the excited state wave function before the second pulse at $t = 610$. (a) $t = 200$ a.u., (b) $t = 400$ a.u., (c) $t = 600$ a.u. Note the dramatic wave packet contraction as the wave packet approaches the hard part of the Morse potential. (d) Ground state wave function at $t = 800$ a.u., after the second pulse. (e) Ground state wave function at $t = 1000$ a.u. (f) Ground state wave function at $t = 1200$ a.u. A significant fraction of the wave packet amplitude is exiting from channel 2 while virtually no amplitude exits from channel 1.

ly the quantum wave packet, including the sequence of contraction and spreading. Figures 19(d)–19(f) shows the swarm on the ground state potential energy surface, after the second pulse. Those trajectories that do exit do so from channel 2. Note the strong resemblance of the swarm to the quantum wave function, shown in Fig. 15.

Figures 20 (a) and 20(b) show the swarm on the excited state potential energy surface for the same pulse sequence as Fig. 16 (second pulse at $t = 1010$ a.u.). The swarm continues to mimic the quantum wave packet. Figures 20(c)–20(e) show the swarm on the ground state potential energy surface after the second pulse. The swarm breaks up on the ground state surface with a substantial number of trajectories exiting from channel 1, followed by an approximately

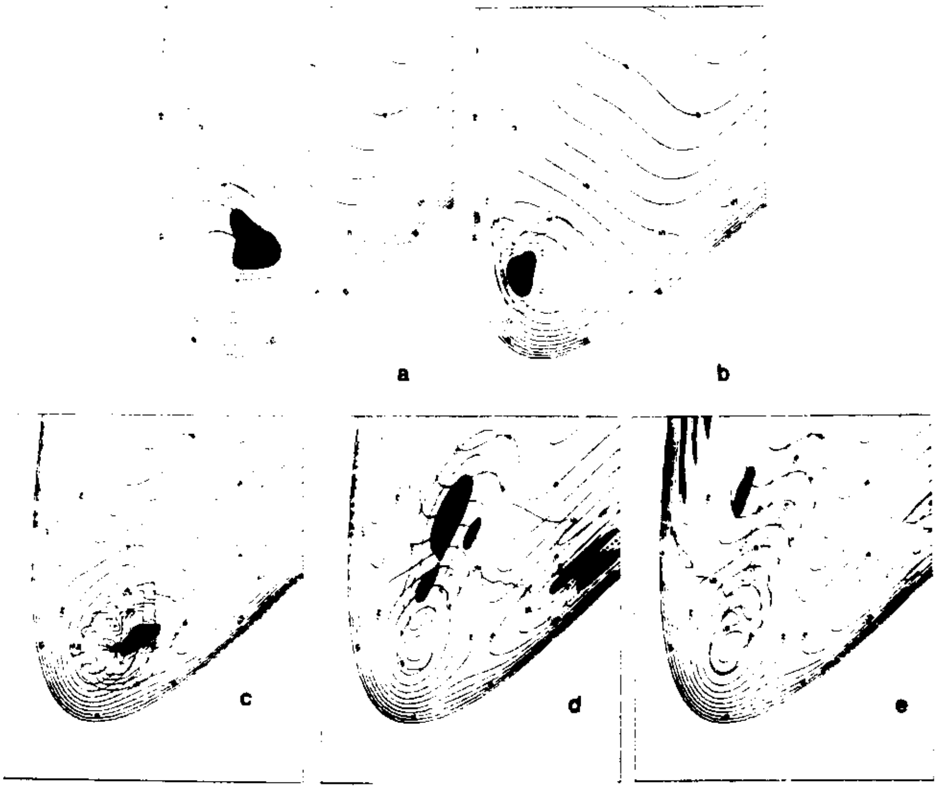

FIG. 16. Magnitude of the excited state wave function before second pulse at $t = 1010$. (a) $t = 800$ a.u., (b) $t = 1000$ a.u. (c) Ground state wave function at $t = 1200$. (d) Ground state wave function at $t = 1400$ a.u. (e) Ground state wave function at $t = 1600$ a.u. Note the wave packet breakup on the ground state surface, with roughly equal amplitudes exiting from channel 1 and channel 2.

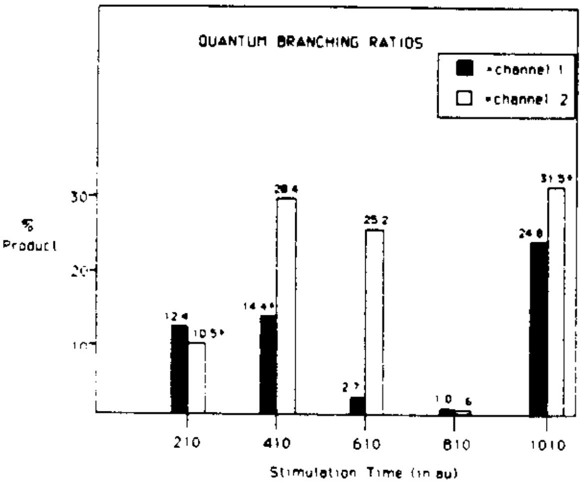

FIG. 17. Quantum mechanical branching ratio as a function of stimulation time. Note the dramatic differences between the branching ratios at different times, relative to each other as well as relative to the amplitude that remains bound.

equal number exiting from channel 2. The entire sequence is in close agreement with the quantum wave function behavior, Figs. 16(a)–16(e).

Figure 21 shows the classical branching ratio as a function of stimulation time, for the same stimulation pulses as in Fig. 17. The trajectories are weighted using the Gaussian distribution Eq. (20), and the same critical values of θ are used as for the quantum branching ratios. Note the qualitative agreement with the quantum mechanical results in both a relative and absolute sense. This is consistent with the analysis of the Wigner swarm presented in Ref. 15. The classical–quantum correspondence is particularly good provided the time evolving state has no nodes. If there are nodes, the classical propagation neglects interference terms which are likely to be significant.[15]

We therefore conclude that a Wigner swarm of classical trajectories is a valuable exploratory tool for estimating quantum mechanical branching ratios. The computer times involved were more than 100 times shorter than for the quantum calculations. For heavier masses and more degrees of freedom the difference in computer times between the classical and quantum calculations will become even more pronounced. Fortunately, for heavier mass systems, the classical–quantum correspondence should be even better than for the hydrogenic mass systems illustrated here.

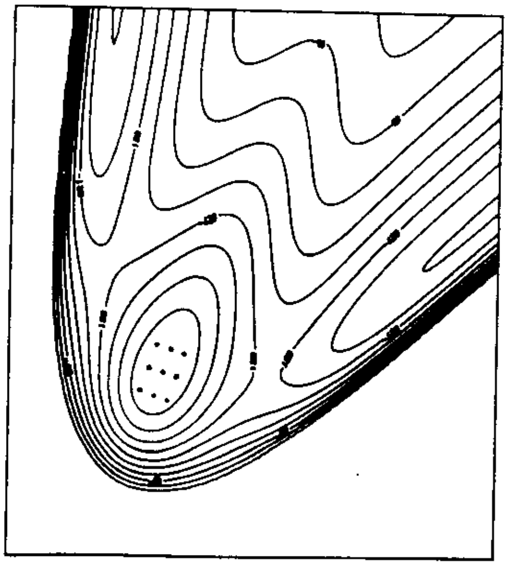

FIG. 18. Initial swarm of classical trajectories on the ground state potential energy surface. The swarm consists of 81 trajectories (there are nine different momentum combinations for each of the coordinate combinations).

However, one must be somewhat cautious about using classical mechanics to model branching ratios that originate from excited vibrational states, and more important for our purposes, for pulse sequences lasting a significant fraction of a vibrational period. In the latter case the convolution of the pulse with the propagating wave function [see Eq. (5)] has nodes. During the free evolution stage following the pulse the classical swarm may not be faithful to the subsequent quantum interference effects.

IV. PHOTON LOCKING

Sleva and Zewail have recently reported "photon locking" in a system that ordinarily undergoes pure dephasing (T_2 type processes).[16] In a single π-pulse experiment their observed T_2 is ~ 1 ns. If a second pulse, phase shifted by $\pi/2$ from the original pulse, is applied continuously after the initial π pulse, the phases of the ensemble of systems are "locked." The dephasing time is now $\gtrsim 1\ \mu$s. Mukamel and Shan recently reported a calculation with essentially the same message, i.e., that intramolecular vibrational redistribution (IVR) can be suppressed by application of suitable fields to a system.[17] In particular, Mukamel and Shan show that if the Rabi frequency Ω is large compared with the energy spread of states that have a component of the optically allowed state,

$$\Omega \gg V_{sl} \tag{21}$$

and if a strong field is allowed to operate continuously, IVR will be suppressed on a time scale much longer than characteristic of IVR in the absence of the strong field.

We have applied the above ideas to the case described in Figs. 10 and 11, where wave packet spreading on the broad, anharmonic, excited state potential energy surface destroys the selectivity. A square pulse was used for excitation:

$$\begin{aligned} \mu E(t) &= A \cos(\omega_e t), \\ A &= 0.125, \quad 20 < t < 40, \\ A &= 0, \quad t < 20, t > 40, \\ \omega_e &= 0.10. \end{aligned} \tag{22}$$

An additional continuous pulse was applied, namely

$$\begin{aligned} C(t) &= C \cos(\omega_c t + \pi/2), \\ C &= 0.125, \quad 40 < t < 1000, \\ C &= 0, \quad t < 40, t > 1000, \\ \omega_c &= 0.10. \end{aligned} \tag{23}$$

Figures 22(a) and 22(b) show the wave function on the excited state potential surface at $t = 200$ a.u. and $t = 400$ a.u. The motion of the center of the wave packet is greatly reduced. More important, with respect to selectivity, there is

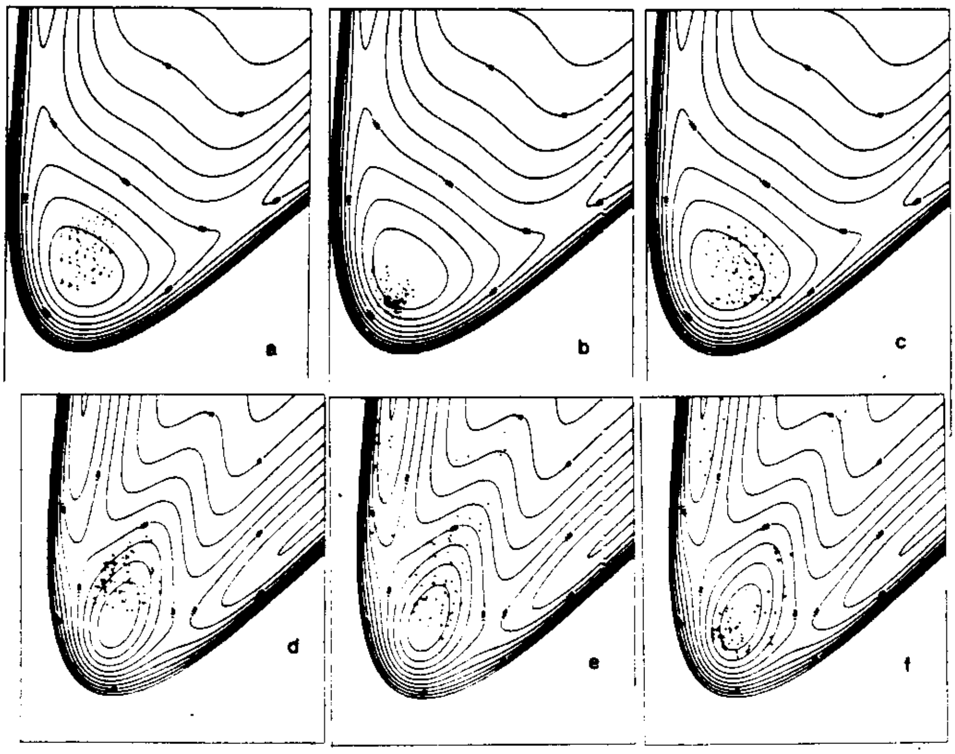

FIG. 19. Swarm of classical trajectories on the excited state potential energy surface, before the second pulse at $t = 610$. (a) $t = 200$ a.u., (b) $t = 400$ a.u., (c) $t = 600$ a.u. (d) Swarm on the ground state potential energy surface at $t = 800$ a.u., after the second pulse. (e) Swarm on the ground state at $t = 1000$ a.u. (f) Swarm on the ground state at $t = 1200$ a.u. Note the strong resemblance of the entire sequence (a)–(f) to the quantum wave function shown in Figs. 15(a)–15(f).

almost no wave packet spreading. This example suggests that strong fields may be used in conjuction with the carefully tailored waveforms we have described above to achieve selectivity of reaction.

V. CONCLUSIONS

We have proposed a novel approach to the control of selectivity of reaction products. The central idea is that in a two-photon, or multiphoton process that is resonant with an excited electronic state, the resonant excited state potential energy surface can be used to assist chemistry on the ground state potential energy surface. By controlling the delay between a pair of ultrashort (femtosecond) laser pulses, it is possible to control the propagation time on the excited state potential energy surface. Different propagation times, in turn, can be used to generate different products. Some selectivity of reactivity should be possible using this scheme. Our examples show a variety of behavior ranging from virtually 100% selectivity to poor selectivity.

In this paper we have shown how an excited electronic

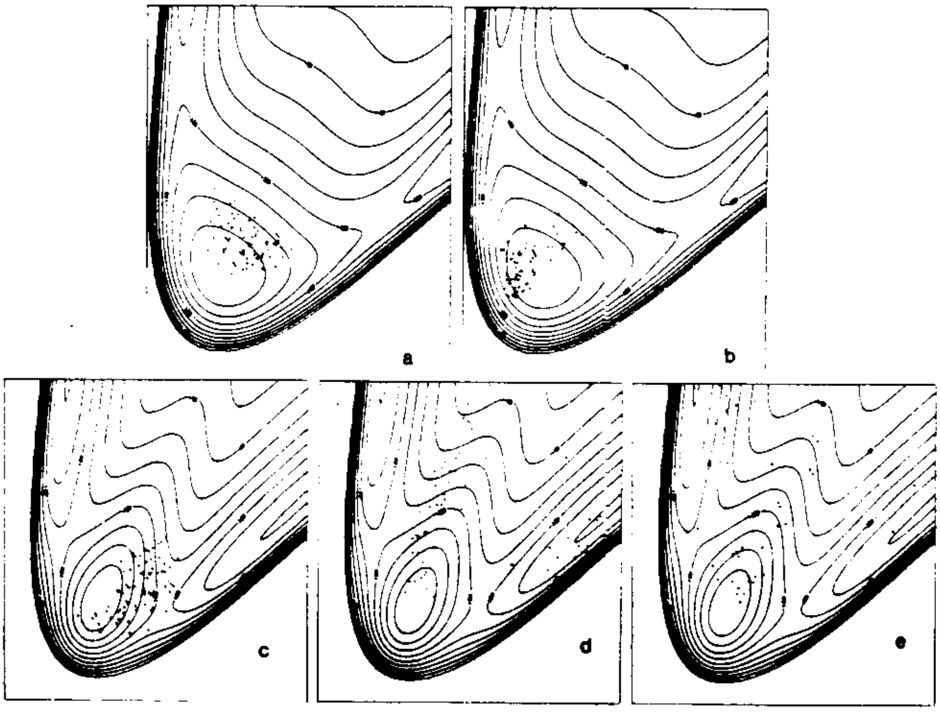

FIG. 20. Swarm of classical trajectories, on the excited state potential energy surface, before the second pulse at $t = 1010$. (a) $t = 800$ a.u., (b) $t = 1000$ a.u. (c) Swarm on the ground state potential energy surface at $t = 1200$. (d) Swarm on the ground state at $t = 1400$ a.u. (e) Swarm on the ground state at $t = 1600$ a.u. Note the breakup of the swarm on the ground state surface. The entire sequence (a)–(e) is in close agreement with the quantum wave function. Figs. 16(a)–16(e).

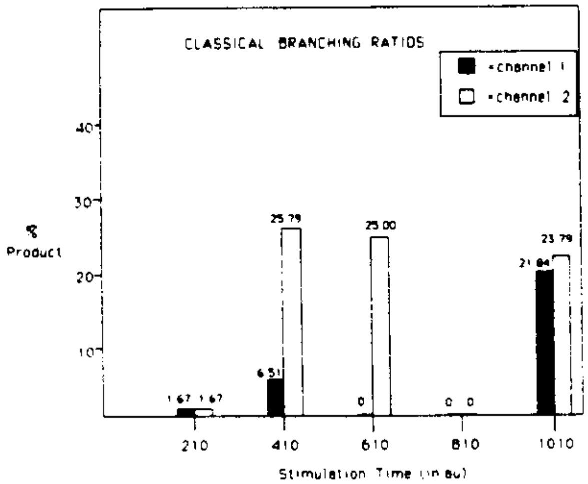

FIG. 21. Classical mechanical branching ratio as a function of stimulation time. Note the qualitative agreement with the quantum branching ratio, Fig. 17.

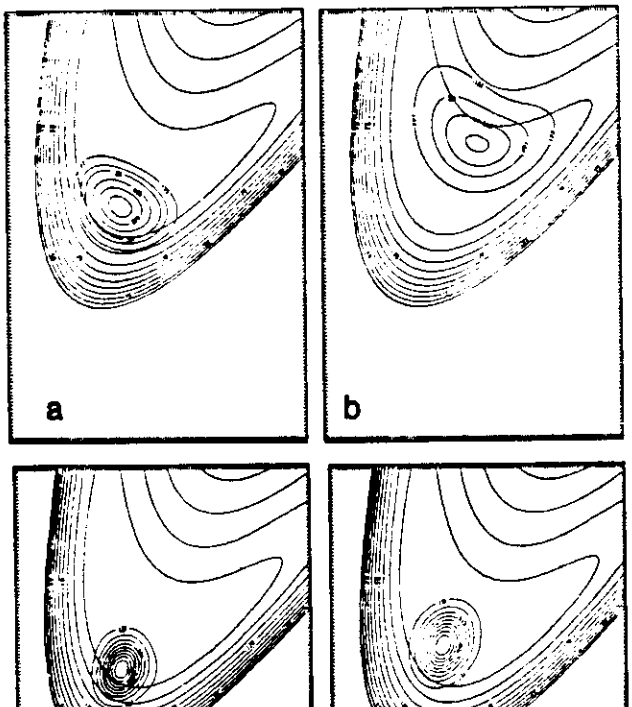

FIG. 22. Excited state wave function for the photon locking sequence described in the text. The wave function for the pulse sequence without locking is presented for comparison. The potential energy surface is the same as in Figs. 12 and 13 (surface II). (a) $t = 200$ a.u., without locking, (b) $t = 400$ a.u., without locking, (c) $t = 200$ a.u., with locking, (d) $t = 400$ a.u., with locking. Note that the locking pulse curbs the wave packet spreading.

state can be used to assist selectivity of product formation on the ground electronic state potential energy surface. We have also argued that for some molecular systems it should be possible to use the ground electronic state to assist selectivity of product formation on an excited electronic state potential energy surface, i.e., that the roles of reactive surface and intermediary assisting surface can be interchanged. The two choices mentioned can be thought of as examples from a spectrum of possibilities inherent in a more general scheme for achieving selectivity of reactivity. That more general scheme involves use of some electronic state to assist selectivity of product formation but allows the initial and final states to be different. Imagine a Franck–Condon transition from some initial state to an intermediate electronic state followed, after a controlled delay, by a transition to a third electronic state (which could be the initial state). If the final state potential energy surface and the intermediate state potential energy surface have the right properties, use of shaped pulses and control of pulse separation will permit selectivity of reactivity on the final state potential energy surface. It is also possible to imagine the use of detuning from resonance with the intermediate electronic state as a tool to augment control of the time scale for evolution in that state.

Recently, several independent theoretical studies have concluded that two-photon processes may afford some selectivity in the preparation of an initial state or the resulting product distributions.[18,19] These studies differ from the present study in three major ways:

(1) Those authors describe the preparation of a superposition of precisely two vibrational states. Implicitly, the wave packet we have described consists of a superposition of a multitude of vibrational levels.

(2) In the above approaches the emphasis is on controlling the electronic state of photochemical products—I vs I^* in Ref. 17 and CS singlet vs triplet states in Ref. 18—rather than on obtaining products with different nuclear constituents.

(3) Finally, the above approaches do not exploit the classical–quantum correspondence principle. This principle plays a central role in our approach.

Clearly, there are many ways in which the ideas we have proposed must be extended. Among the more important extensions we cite variational optimization of the shape, duration, and separation of the pulses used to generate the selectivity of reactivity, and analysis of the changes induced by inclusion of all degress of freedom of the molecule (say in the sense of a reaction path Hamiltonian, or a dynamical path Hamiltonian). For studies involving more degrees of freedom a swarm of classical trajectories should be an indispensible tool.

The shortest pulses available at the present time are on the order of 10–30 fs. The classical windows shown in the examples (which refer to model systems with hydrogenic masses) are on the order of a few fs. We expect the overall time scales to become longer by about a factor of 5 for somewhat larger masses than assumed in the model systems studied to date. Thus the experiments we are proposing are at the very edge of the existing technology. Nevertheless, as the technology improves we expect there will be many applications and variations on the ideas suggested in this paper.

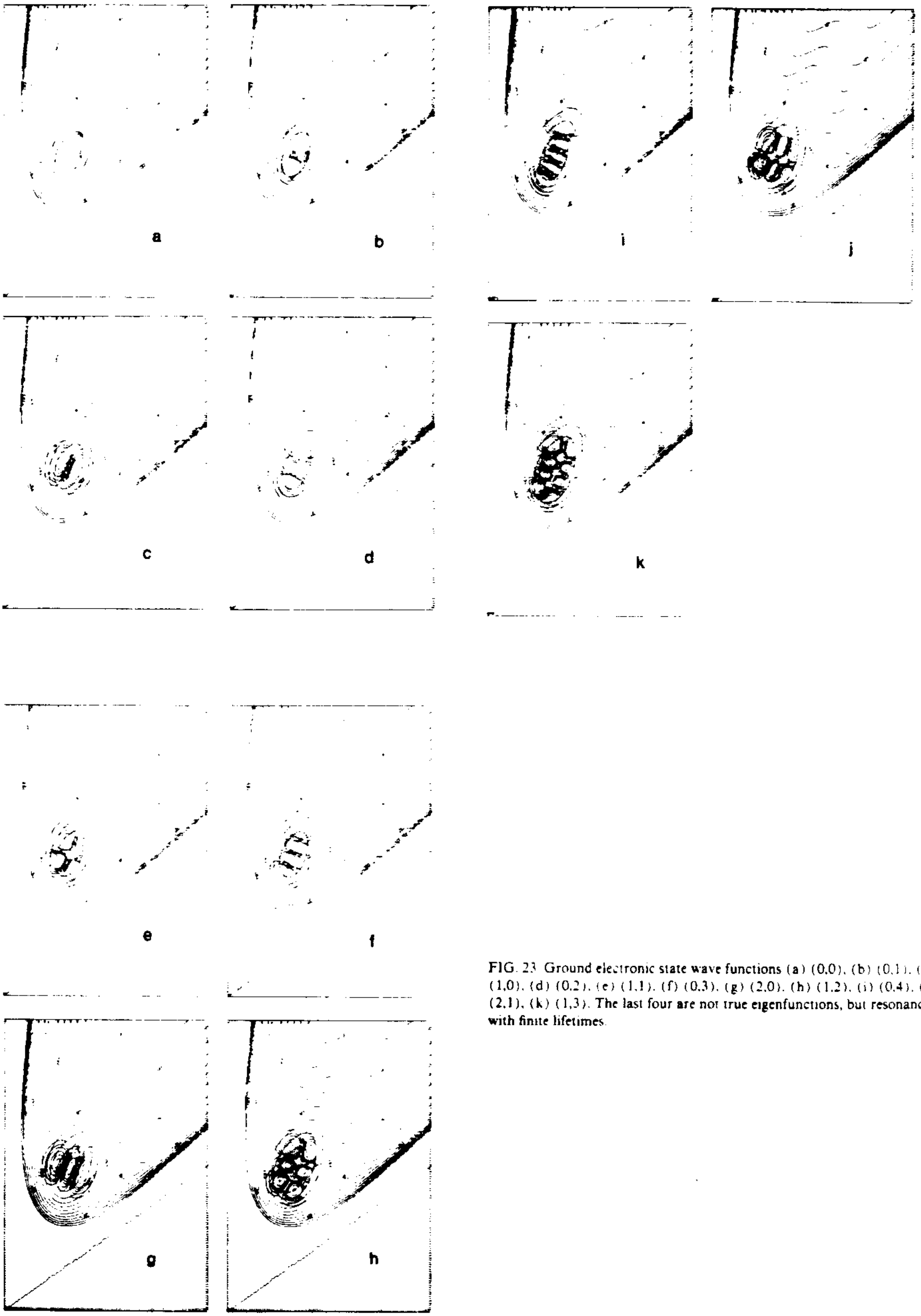

FIG. 23. Ground electronic state wave functions (a) (0,0), (b) (0,1), (c) (1,0), (d) (0,2), (e) (1,1), (f) (0,3), (g) (2,0), (h) (1,2), (i) (0,4), (j) (2,1), (k) (1,3). The last four are not true eigenfunctions, but resonances with finite lifetimes.

ACKNOWLEDGMENTS

This research was supported by grants from the National Science Foundation and the AFOSR. D. J. T. wishes to thank Professor Eric Heller and Professor Dan Imre for helpful suggestions, and Dr. Stephen Gray for introducing him to the Wall–Porter potential.

APPENDIX

In this Appendix we describe how the exact bound state wave functions for the potential energy surface shown in Fig. 1 were obtained. The second derivative matrix,

$$V'' = \begin{pmatrix} V_{xx} & V_{xy} \\ V_{yx} & V_{yy} \end{pmatrix}, \tag{A1}$$

is calculated for the potential energy surface, at its minimum. These second derivatives determine a harmonic fit to the potential energy surface, and the ground vibrational state wave function of the harmonic surface, χ_0^h is used as a first guess to the true ground vibrational state wave function, χ_0. In fact χ_0^h contains a component of all the true vibrational states wave functions,

$$\chi_0^h = \sum_n c_n \chi_n. \tag{A2}$$

χ_0^h is then propagated in imaginary time τ, $\tau \equiv it$, using an expansion in a set of grid points and the Fourier method for evaluating $H\psi$, as described in Sec. II of the text. That is

$$e^{-H\tau/\hbar}\chi_0^h = \sum_n c_n e^{-E_n\tau/\hbar}\chi_n. \tag{A3}$$

Because of the exponential decay, the components of all excited wave functions χ_n vanish quickly compared with the component of χ_0. After waiting a sufficient amount of time (see below) and renormalizing, one obtains χ_0. The energy of the ground vibrational state may then be obtained from

$$E_0 = \langle \psi_0 | H \; \psi_0 \rangle. \tag{A4}$$

To obtain $\chi_{0,1}$ one begins with $\chi_{0,1}^h$, the first excited vibrational state of the harmonic surface fit. (The subscripts refer to the high and low frequency normal coordinates, in that order.) This trial function contains a component of the true ground vibrational state χ_0 which is immediately filtered out by a Gram–Schmit orthogonalization. The resulting wave function is then propagated in imaginary time; only the component of $\chi_{0,1}$ will survive after a sufficiently long time. After normalizing, $\chi_{0,1}$ is obtained. $E_{0,1}$ may then be obtained as well.

This procedure may be continued up the ladder of vibrational wave functions. For each new wave function the component of all the lower energy wave functions must be filtered out by Gram–Schmidt orthogonalization before beginning the propagation. In principle, the necessary propagation time is $t = \hbar/\Delta E$, where ΔE is the energy difference between the exact wave function being sought and the next higher up. Since the energies of neither of these wave functions is known beforehand, the propagation, in practice, is continued until convergence is obtained. As one proceeds up the vibrational ladder the density of states increases. The propagation times consequently become longer in order to resolve the state of interest from the states of just slightly higher energy.

This procedure was used to obtain all the bound state wave functions, as well as several long lived resonances, for the potential energy surface shown in Fig. 1. There are seven bound states in total. The wave functions and several long-lived resonances are displayed in Figs. 19(a)–19(k).

[1] D. J. Tannor and S. A. Rice, J. Chem. Phys. **83**, 5013 (1985).
[2] E. J. Heller, J. Chem. Phys. **62**, 1544 (1975).
[3] E. J. Heller, J. Chem. Phys. **68**, 2066 (1978).
[4] E. J. Heller, Acc. Chem. Res. **14**, 368 (1981).
[5] S. -Y. Lee and E. J. Heller, J. Chem. Phys. **71**, 4777 (1979).
[6] D. J. Tannor and E. J. Heller, J. Chem. Phys. **77**, 202 (1982).
[7] E. J. Heller, R. L. Sundberg, and D. J. Tannor, J. Chem. Phys. **86**, 1822 (1982).
[8] D. J. Tannor, M. Blanco, and E. J. Heller, J. Phys. Chem. **88**, 6240 (1984).
[9] A. Messiah, *Quantum Mechanics* (Wiley, New York, 1958), Vol. I.
[10] A. Askar and A. S. Cakmak, J. Chem. Phys. **67**, 2017 (1977).
[11] D. Kosloff and R. Kosloff, J. Comput. Phys. **52**, 35 (1983).
[12] R. Kosloff and D. Kosloff, J. Chem. Phys. **79**, 1823 (1983).
[13] F. T. Wall and R. N. Porter, J. Chem. Phys. **36**, 3256 (1962).
[14] (*210) Channel 2, 10.5% product formed at 2400 a.u (*410) Channel 1, 14.4% product formed at 2400 a.u. (*1010) Channel 2, 31.5% product formed at 3200 a.u.
[15] E. J. Heller, J. Chem. Phys. **65**, 1289 (1977).
[16] E. T. Sleva and A. H. Zewail (private communication).
[17] S. Mukamel and K. Shan, Chem. Phys. Lett. **117**, 489 (1985).
[18] M. Shapiro and P. Brumer, J. Chem. Phys. **84**, 4103 (1986), P. Brumer and M. Shapiro, Chem. Phys. Lett. **126**, 54 (1986).
[19] T. A. Holme and J. S. Hutchinson, Chem. Phys. Lett. **124**, 181 (1986); J. Chem. Phys. (submitted).

Reprinted from The Journal of Physical Chemistry, 1986, 90, 3470

Bottlenecks to Unimolecular Reactions and an Alternative Form for Classical RRKM Theory

Stephen K. Gray, Stuart A. Rice,*

Department of Chemistry and The James Franck Institute, The University of Chicago, Chicago, Illinois 60637

and Michael J. Davis

Chemistry Division, Argonne National Laboratory, Argonne, Illinois 60439 *(Received: January 9, 1986)*

Bottlenecks to the flow of phase points in the classical phase space of a triatomic molecule are discussed and approximated for the example of van der Waals predissociation of HeI_2. An alternative form for the usual transition-state theory of unimolecular reactions, RRKM theory, is developed by approximating the intermolecular (separatrix) bottleneck and using it as a basis for the transition-state surface. The rates obtained with the theory are in surprisingly good accord with dynamical rates from classical trajectory studies.

I. Introduction

The standard, highly successful, statistical theory of unimolecular reactions is due to Rice, Ramsperger, Kassel, and Marcus (RRKM).[1] The present form of the theory is due mostly to Marcus and Rice,[2] who took the more primitive RRK description of unimolecular reactions, reformulated it using a transition-state analysis, including zero-point energy effects, and thereby arrived at a proper quantum mechanical transition-state theory of unimolecular reactions. The work of Eyring and co-workers[3] along similar lines should also be noted. Actually, the transition-state concept is more easily and generally understood within the framework of a classical mechanical description of the reaction, where it refers to a dividing surface in the classical phase space of the system. A theory of unimolecular reactions based on the classical transition-state concept can be formulated using, for example, the pioneering ideas of Wigner.[4] Such a classical transition-state theory is often referred to in the literature as classical RRKM theory. It is the classical version of RRKM theory that is the primary subject of this paper.

The usual formulation of classical RRKM theory involves a configuration space definition of the transition state.[5] We will show that an alternative version of classical RRKM theory can be formulated in terms of phase space bottlenecks, and that in certain situations this new version can give superior results. Much of our work is based on an earlier paper by Davis and Gray,[6] which in turn was based on developments in the theory of the nonlinear dynamics of area-preserving mappings;[7] we briefly review this earlier work in the following paragraphs.

The last decade has seen remarkable advances in our understanding of the dynamics associated with the iteration of an area-preserving map.[7] One of the driving forces for the study of area-preserving mappings has been the wish to understand when they are quasi-periodic and when they are partly or wholly chaotic, and to determine the nature of "flow", or successive iterations of the map, particularly in the chaotic regime. Mackay, Meiss, and Percival,[8] and independently but to a lesser extent Bensimon and Kadanoff,[9] have developed a theory of flow in area-preserving mappings in the chaotic regime. The idea they exploit it that KAM tori, which are defined by and therefore "support" quasi-periodic motion, serve as natural boundaries between chaotic regions so that, as such tori disappear, phase points may leak from one region to another. Indeed, the broken remnants of a KAM torus, called a cantorus by Mackay, Meiss, and Percival,[8] serves as a barrier, or perhaps better put as a bottleneck, to the flow of phase points. The investigators mentioned use this definition of a barrier to develop a theory of transport of phase points in area-preserving mappings. The cantorus can be identified as an intramolecular bottleneck or partial barrier to internal energy flow for unimolecular reactions.[10] A related but different and very important bottleneck is one identified with the remnants of a separatrix,[7] which is a special structure in the phase space separating different kinds of tori; a key paper of Channon and Lebowitz[11] clearly discusses flow across separatrices. Certain separatrices can be identified as intermolecular bottlenecks,[6] or partial barriers to unimolecular fragmentation, and we will base our alternative formulation of RRKM theory on them.

The dynamics of a Hamiltonian system can be related to iterations of an area-preserving mapping (e.g., the Poincaré surface of section of a two-degree-of-freedom Hamiltonian system is an area-preserving mapping). Davis[10] was the first to exploit the analysis of intramolecular bottlenecks in phase space using the methods and ideas of Mackay, Meiss, and Percival[8] and Bensimon and Kadanoff[9] to provide an interpretation of intramolecular energy transfer in a nonrotating collinear model for OCS. More recently, Davis and Gray[6] have developed an approach to calculating unimolecular reaction rates based on a precise identification of both intramolecular *and* intermolecular bottlenecks in the classical phase space, and the calculation of fluxes across these bottlenecks. In its most rigorous form the theory was shown to describe very accurately the classical fragmentation rate for a two-degree-of-freedom model of HeI_2 vibrational predissociation, an example for which standard RRKM theory is grossly in error. Figure 1 summarizes the results of ref 6 of relevance to the present paper. Figure 1a shows the surface of section for several trajectories of the T-shaped HeI_2 model, with the pertinent intramolecular and intermolecular bottlenecks drawn in as dashed lines. Only one intramolecular bottleneck is relevant for this system at the particular total energy chosen for the surface of section, but it is possible in other situations to have more than one important intramolecular bottleneck. There are two stochastic (by which we mean wandering) trajectories shown in the figure. One stochastic trajectory, at least for the time scale investigated, appears confined within the intramolecular bottleneck (the closed dashed curve). Notice also that within this bottleneck are quasi-periodic

---

(1) (a) Forst, W. *Theory of Unimolecular Reactions*; Academic: New York, 1973. (b) Robinson, P. J.; Holbrook, K. A. *Unimolecular Reactions*; Wiley: New York, 1972. (c) Hase, W. L. In *Modern Theoretical Chemistry*; Miller, W. H., Ed.; Plenum: New York, 1976; Vol. 2, p 121.

(2) (a) Marcus, R. A.; Rice, O. K. *J. Phys. Colloid Chem.* **1951** *55*, 894. (b) Marcus, R. A. *J. Chem. Phys.* **1952**, *20*, 355, 359, 364.

(3) (a) Rosenstock, H. M.; Wallenstein, M. B.; Wahrhaftig, A. L.; Eyring, H. *Proc. Natl. Acad. Sci. U.S.A.* **1952**, *38*, 667. (b) Giddins, J. C.; Eyring, H. *J. Chem. Phys.* **1956**, *22*, 538.

(4) (a) Wigner, E. P. *J. Chem. Phys.* **1937**, *5*, 720. (b) *Ibid.* **1939**, *7*, 646.

(5) E.g.: Doll, J. D. *J. Chem. Phys.* **1980**, *73*, 2760.

(6) Davis, M. J.; Gray, S. K. *J. Chem. Phys.* **1986**, *84*, 5389.

(7) Lichtenberg, A. J.; Lieberman, M. A. *Regular and Stochastic Motion*; Springer: New York, 1983.

(8) Mackay, R. S.; Meiss, J. D.; Percival, I. C. *Physica D*, **1984**, *13*, 55.

(9) Bensimon, D.; Kadanoff, L. P. *Physica D* **1984**, *13*, 82.

(10) Davis, M. J. *J. Chem. Phys.* **1985**, *83*, 1016.

(11) Channon, S. R.; Lebowitz, J. *Ann. N.Y. Acad. Sci.* **1980**, *357*, 108.

0022-3654/86/2090-3470$01.50/0

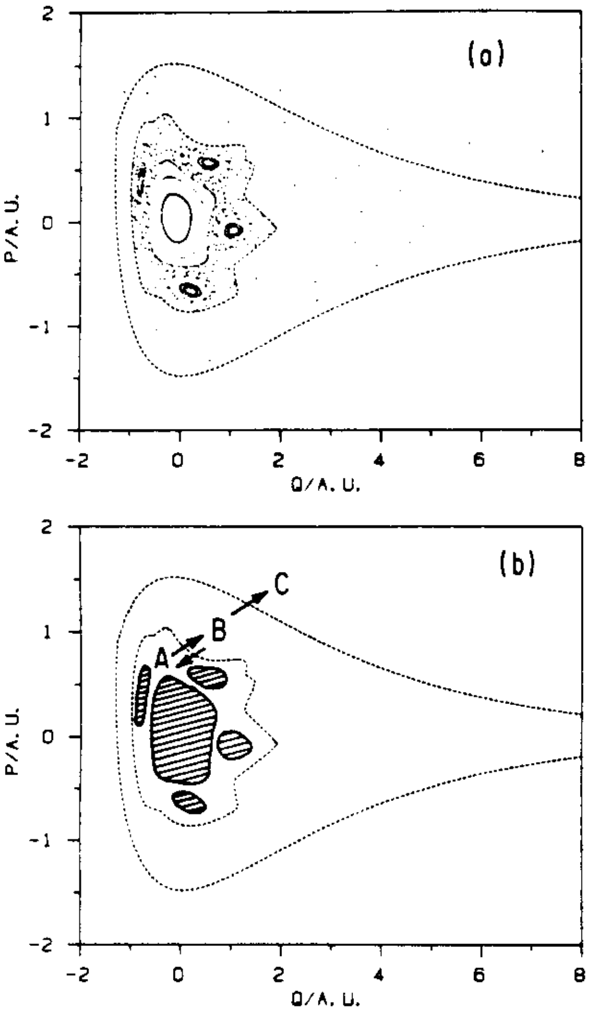

Figure 1. (a) Composite surface of section for the nonrotating T-shaped HeI_2 model of ref 6. Q is proportional to the translational coordinate, $Q = R - R$, where R is the He to center of mass of I_2 distance and R is given in Table I. P is th momentum conjugate to Q and a trajectory is plotted whenever $r = r_{BC}$ and $p > 0$ in the I_2 canonical coordinates. The intramolecular (inner, closed dashed curve) and intermolecular (outer, open dashed curve) bottlenecks are drawn in. The total energy of all the trajectories is $E = -2662$ cm^{-1}. (b) Idealization of Figure 1a indicating flow out of various phase space regions discussed in the text. The hatched areas represent regions of quasi-periodic motion.

trajectories, indicated by sequences of points forming closed curves. The other stochastic trajectory lies between the intramolecular and intermolecular (outer dashed curve) bottlenecks for much of the time. Actually, both these trajectories can in principle leak across the intramolecular bottleneck and enter the other's domain, and ref 10 discusses how the rate of flow across such bottlenecks may be obtained. The outer stochastic trajectory can also leak across the intermolecular bottleneck, and indeed the upper sequence of dots above the intermolecular bottleneck shows that it has done so. The feature that distinguishes the intermolecular from the intramolecular bottleneck is that once a phase point crosses the intermolecular bottleneck from the inside it cannot return and instead continues on to the product asymptote (He + I_2). The intermolecular bottleneck is thus literally the best transition state.[12] Figure 1b gives a clearer representation of these results. In this figure the phase space is divided into four regions corresponding to quasi-periodic motion (hatched), stochastic motion (A and B), and product formation (C). Actually, only the upper half of region C corresponds to "products", or separating fragments He and I_2; the lower half represents approaching fragments and is of relevance to bimolecular scattering, which is not the subject of this paper (see, however, ref 6). Arrows indicate the possibility of flow into and out of the regions defined. Note that the region corresponding to quasi-periodic motion is inaccessible to trajectories in the stochastic regions. While the use of a segregated phase space is far from new in unimolecular reaction rate theory—see, for example, ref 13–15—an explicit construction of all the phase space dividing curves for a unimolecular reaction was first reported in ref 6.

At present, however, the precise construction of the relevant bottlenecks to flow in phase space is only practical for systems with just two degrees of freedom. It is also fair to say that the method of analysis given in ref 6, while relatively straightforward, can be quite lengthy. In ref 6 the intermolecular bottleneck was constructed on a Poincaré surface of section via the propagation in time of about a hundred phase points. However, it is noteworthy that in the limit of zero coupling the intermolecular bottleneck can be identified with a separatrix or "last bound phase curve" of some zero-order Hamiltonian. Thus an obvious and, as we shall see, surprisingly successful approximation is to simply identify some appropriate zero-order Hamiltonian for the critical degree of freedom and use the associated separatrix as the intermolecular bottleneck. The flux across this bottleneck is then easily determined by propagating the entire separatrix one iteration on the surface of section, as discussed in ref 6. A related idea for approximating the intramolecular bottlenecks, however, will be shown to be less successful.

The success of the zero-order separatrix approximation to the intermolecular bottleneck leads us to construct a simple alternative form for classical RRKM theory. The critical configuration, or transition state, in RRKM theory, is now represented not by a configuration space surface, as is most commonly done, but rather by a phase space surface involving the zero-order separatrix. When applied to T-shaped HeI_2 dissociation this form of RRKM theory will be seen to yield rates within a factor of five of the exact classical rates, a remarkable improvement over standard RRKM theory for this example. The alternative RRKM theory, like standard RRKM theory, can be applied to molecules with several degrees of freedom, and this is illustrated with a study of HeI_2 fragmentation in three dimensions. Actually, our "alternative form" of unimolecular reaction rate theory is not really new in the sense that Wigner, in his original formulation of transition-state theory,[4] explicitly had in mind what we now call separatrices. Thus one view of the statistical theory presented in this paper is that it is an application to unimolecular reactions of Wigner's version of transition-state theory. Finally, it must be emphasized that the theory presented here is not intended to be a replacement for standard RRKM theory, which after all is very successful. Rather, the alternative transition-state theory presented here is to be used when the dynamics is such that certain of the simplest assumptions of RRKM theory about the nature of the transition state are incorrect, but a transition state can nonetheless be defined based on phase space bottlenecks. The fragmentation of a van der Waals molecule such as HeI_2 is a particularly good example of such a situation.

In section II we discuss zero-order approximations to the inter- and intramolecular bottlenecks, and the corresponding unimolecular rates for the two degree of freedom HeI_2 predissociation example discussed in ref 6. In section III we discuss our simple alternative form for RRKM theory and in section IV applications of the alternative RRKM theory to the simple two-degree-of-freedom HeI_2 model (section IVA) and also a three-degree-of-freedom HeI_2 model (section IVB). Section V contains some remarks on further extensions of the ideas presented in this paper.

II. Zero-Order Approximations to Phase Space Bottlenecks

A. Intermolecular Bottlenecks. The zero-order approximation of intermolecular bottlenecks will be illustrated with the T-shaped

---

(12) Pechukas, P. *Annu. Rev. Phys. Chem.* **1981**, *32*, 159 and references therein.

(13) Kay, K. G. *J. Chem. Phys.* **1976**, *65*, 3813.

(14) Marcus, R. A.; Hase, W. L.; Swamy, K. N. *J. Phys. Chem.* **1984**, *88*, 6717.

(15) Hase, W. L.; Buckowski, D. G.; Swamy, K. N. *J. Phys. Chem.* **1983**, *87*, 2754.

TABLE I: Potential Parameters for HeI_2[a,b]

$\mu = 3.8779$ amu	$m = 63.5$ amu	
$D_{XB} = 18$ cm^{-1}	$\alpha_{XB} = 0.6033$ au	$\bar{R}_{XB} = 7.5589$ au
$D_{BC} = 4911$ cm^{-1}	$\alpha_{BC} = 0.9380$ au	$\bar{r}_{BC} = 5.6994$ au
$D = 36$ cm^{-1}	$\alpha = 0.5587$ au	$\bar{R} = 7.0012$ au

[a] The reduced mass μ used in this paper is 1.5% lower than the more precise value based on current atomic masses; rates calculated with the more precise value differ negligibly from those with the above mass. [b] Our calculations were performed in atomic units (au). The above masses and energies may be converted to au by multiplication by 1823 and 4.5563×10^{-6}, respectively.

two-degree-of-freedom HeI_2 model studied in detail in ref 6 and also in ref 16 and 17. The full Hamiltonian is taken to be

$$H = \frac{P^2}{2\mu} + \frac{p^2}{2m} + V(R,r) \qquad (1)$$

with

$$V(R,r) = 2V_{XB}(R_{XB}) + V_{BC}(r) \qquad (2)$$

In eq 2 R_{XB} is the distance between He and either of the iodine atoms and is related to the chosen canonical coordinates through

$$R_{XB} = (R^2 + r^2/4)^{1/2} \qquad (3)$$

where V_{XB} and V_{BC} are Morse potentials for the He–I and I–I interactions, respectively. Throughout this paper we will use the same Morse parameters as in ref 6 and 16; these are listed in Table I. The Appendix of ref 16 shows, by linearization of eq 3 about the T-shaped equilibrium geometry ($\bar{R}$, $\bar{r}_{BC}$), that a reasonable zero-order approximation to the full Hamiltonian is given by

$$H_0 = \frac{P^2}{2\mu} + \frac{p^2}{2m} + V_R(R) + V_{BC}(r) \qquad (4)$$

where V_R is an effective Morse potential for the van der Waals interaction, the parameters of which are also listed in Table I. Since R, the He–I_2 distance, is clearly the critical degree of freedom, we introduce the zero-order Hamiltonian associated with R and its canonically conjugate momentum P:

$$h_R(P,R) = \frac{P^2}{2\mu} + V_R(R) \qquad (5)$$

Equation 5 is the Hamiltonian for a one-dimensional Morse oscillator and the separatrix, or last bound phase curve, is simply obtained as the curve in (P,R) space satisfying

$$h_R = 0 \qquad (6)$$

where it has been assumed that $V_R \rightarrow 0$ as $R \rightarrow \infty$. Figure 2 displays the resulting separatrix curve (dashed line) and compares it to the exact intermolecular bottleneck (solid line) determined in ref 6 for the case of a total energy corresponding to approximately $v = 10$ in the I_2 bond and zero-point energy in the He–I_2 van der Waals interaction, $E = -3683$ cm^{-1}. It is clear that the zero-order approximation is very close to the actual bottleneck. Note that eq 6 implies that the zero-order approximation is energy-independent, but the actual intermolecular bottleneck does depend on the energy. This is a peculiarity of how we chose to define the approximate bottleneck and need not always be the case. Comparison of the separatrix determined by eq 6 with the intermolecular bottlenecks at higher energies (not presented) shows there is only a slight variation of the exact bottleneck with energy in this case and that the zero-order approximation is still reasonably good between the energies -3683 cm^{-1} ($v = 10$) and -573 cm^{-1} ($v = 50$).

It is now possible to estimate the flux across the intermolecular bottleneck on a surface of section. Consider again energy $E = -3683$ cm^{-1} and define an initial ensemble of, say, 500 (P,R) points satisfying eq 6. The other two canonical variables, corresponding to the I_2 momentum and internuclear separation (p,r), are obtained by noting that on the surface of section $r = \bar{r}_{BC}$. Then the condition $p > 0$, coupled with energy conservation, uniquely determines p. We proceed by propagating each of the 500 (P,R,p,r) points using Hamilton's equations and the full Hamiltonian (eq 1) until each trajectory crosses the surface of section again. The resulting curve, corresponding to propagation of the entire initial curve one iteration on the surface of section, and the initial curve, are displayed in Figure 3a. The flux out of the approximate intermolecular bottleneck is the area of the propagated curve that lies outside the original area. Most of the flux is within the upper left lobe of Figure 3a and may be thought of as passing through a turnstile, just as in the rigorously defined intermolecular bottleneck case.[6] However, a distinguishing feature of the approximate intermolecular bottleneck is that flux can also escape from other parts of the initial curve. Figure 3b–d displays the results of calculations similar to those just described but now for $E = -2662$ cm^{-1} ($v = 20$), -1807 cm^{-1} ($v = 30$), and -573 cm^{-1} ($v = 50$). Notice that Figure 3d illustrates clearly that flux leaks out from regions other than the main turnstile, which is to be contrasted with the flux across the exact intermolecular bottleneck, Figure 10 of ref 6.

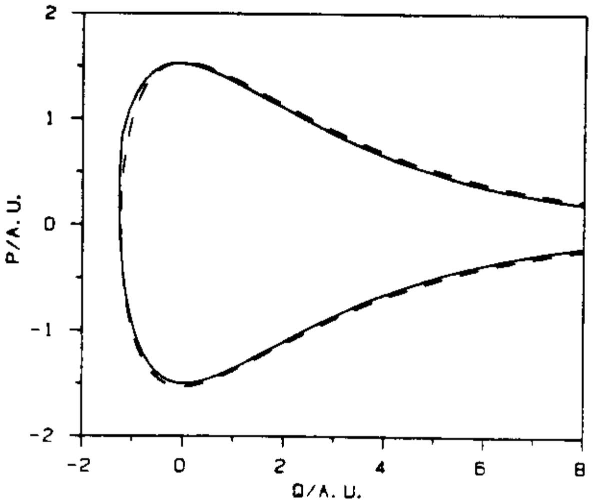

Figure 2. Comparison of exact (solid) and zero-order (dashed) intermolecular bottlenecks. The exact intermolecular bottleneck is for $E = -3683$ cm^{-1}.

We may obtain the flux of phase points by simple graphical means; Table II tabulates the fluxes and intermolecular bottleneck crossing rates defined by

$$k = \frac{F}{A}\frac{\bar{\omega}}{2\pi} \qquad (7)$$

where $\bar{\omega}$ is the hopping frequency through the surface of section, F represents the flux out, and A is the total area of the intermolecular bottleneck. As discussed in ref 6, $\bar{\omega}$ can be reasonably approximated in this case by the Morse oscillator frequency for I_2, calculated for the corresponding value of v. There are three different rates given in Table II and it is important to understand how they differ. Under the heading $\hbar k$ we have the approximate intermolecular bottleneck crossing rate, calculated as described above. In parentheses under this heading we also give the exact intermolecular bottleneck crossing rate calculated in ref 6. In this latter calculation the exact intermolecular bottleneck, not the zero-order separatrix, was used. Finally, under the heading $\hbar k^{frag}$ we give the exact classical fragmentation rate, calculated from an ensemble of classical trajectories.[6] Since the fragmentation rate has been calculated making no assumptions about bottlenecks, the difference between it and the intermolecular bottleneck crossing rate may be taken as a measure of the importance of the intramolecular bottlenecks that lie within the intermolecular bottleneck. Table II shows clearly that our approximate intermolecular bottleneck crossing rates are within a factor of 2 of the exact intermolecular bottleneck crossing rates, which is quite good agreement. Furthermore, it will be noted that for $E \geq -2662$ cm^{-1} the intermolecular crossing rate is also reasonably close to the

---

(16) Gray, S. K.; Rice, S. A.; Noid, D. W. *J. Chem. Phys.* **1986**, *84*, 2649.
(17) Beswick, J. A.; Delgado-Barrio, G. *J. Chem. Phys.* **1980**, *73*, 3653.

TABLE II: Intermolecular Bottleneck Rate Data[e]

E, cm^{-1}	v[a]	A, au	F, au	$\bar{\omega}$,[b] cm^{-1}	$\hbar k^{\text{inter}}$,[c] cm^{-1}	$\hbar k^{\text{frag}}$,[d] cm^{-1}
−3683	10	17.3 (16.6)	0.23 (0.18)	110.5	0.23 (0.19)	0.007
−2662	20	17.3 (16.6)	0.75 (0.42)	93.8	0.65 (0.37)	0.17
−1807	30	17.3 (16.4)	1.09 (0.83)	77.1	0.77 (0.63)	0.56
−574	50	17.3 (15.7)	3.08 (2.92)	43.8	1.24 (1.33)	1.57

[a] v is the zero-order vibrational quantum number in I_2. The total energy $E = E_r(v) + E_R(n=0)$ except for $E = -574$ cm^{-1}, where it is only $E_r(v)$. [b] We approximate $\bar{\omega} = \omega_r(v) = \omega_{BC} - (2v + 1)x_{BC}$, where ω_r is the uncoupled I_2 vibration frequency. From ref 16, $\omega_{BC} = 128$ cm^{-1} and $x_{BC} = 0.834$ cm^{-1}. [c] Numerical values for rates are given in terms of the corresponding decay widths, $\hbar k$. To obtain a rate in ps^{-1}, for example, multiply the above numbers by 0.1884. [d] Dynamically determined fragmentation rates from ref 6. In the case $E = -574$ cm^{-1}, we have taken the numerical rate calculated by eliminating the direct dissociation component, as discussed in section IIIC of ref 6. [e] The precise dynamical values from ref 6 are in parentheses for comparison.

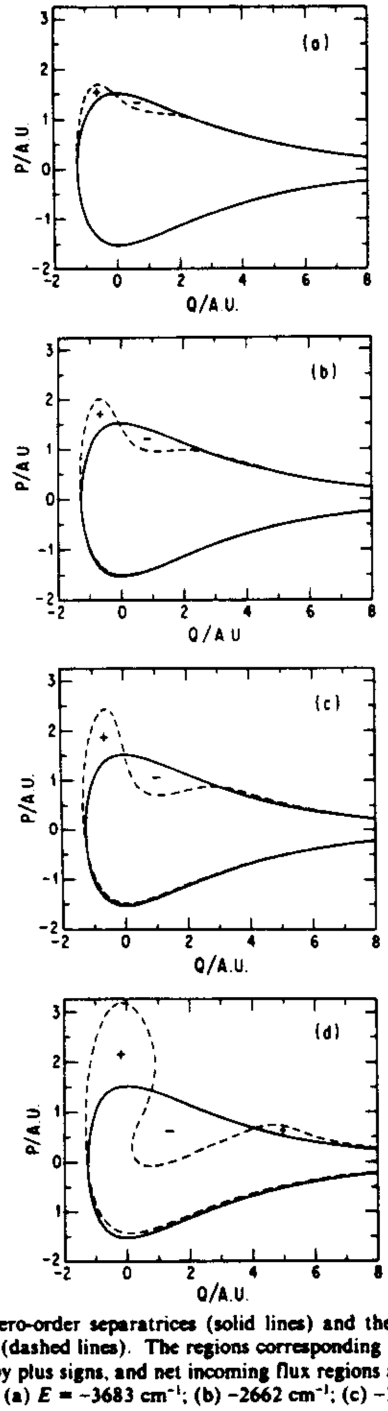

Figure 3. Zero-order separatrices (solid lines) and their propagated counterparts (dashed lines). The regions corresponding to net flux out are marked by plus signs, and net incoming flux regions are marked by minus signs. (a) $E = -3683$ cm^{-1}; (b) −2662 cm^{-1}; (c) −1807 cm^{-1}; (d) −573 cm^{-1}.

actual fragmentation rate. This observation is very important because it allows us, as a first approximation, to simply ignore the dynamics of energy exchange within the intermolecular bottleneck, and to calculate an approximate fragmentation rate based solely on the intermolecular bottleneck crossing rate. Of course this is a very bad approximation for low energies, such as $E = -3683$ cm^{-1}, where there is a large difference between intermolecular bottleneck crossing and fragmentation rates due to the presence of intramolecular bottleneck effects, as is discussed in more detail in ref 6.

B. Intramolecular Bottlenecks. An approximation to intramolecular bottlenecks similar in spirit to the approximation to intermolecular bottlenecks can easily be generated. As before we will deal with the HeI$_2$ model. Recall[6,8,10] that an intramolecular bottleneck is identified with the remnants (cantorus) of a robust torus with frequency ratio related to the golden mean. Therefore the simplest approximation to the cantorus is a zero-order torus with frequency ratio

$$\frac{\omega_r(v)}{\omega_R(n)} = j + g \tag{8}$$

where j is a positive integer and $g = 0.618\,033\,9...$ is the golden mean. The torus is parameterized by the vibrational actions v and n, as well as the associated angles q_v and q_n. If one uses eq 4 as the zero-order Hamiltonian, the Appendix of ref 16 shows that

$$H_0 = E_R + E_r \tag{9}$$

where

$$E_R = (n + \tfrac{1}{2})\omega - (n + \tfrac{1}{2})^2\frac{\omega^2}{4D} - D \tag{10}$$

$$E_r = (v + \tfrac{1}{2})\omega_{BC} - (v + \tfrac{1}{2})^2\frac{\omega_{BC}^2}{4D_{BC}} - D_{BC}$$

and

$$\omega_R(n) = \partial E_R/\partial n$$

$$\omega_r(v) = \partial E_r/\partial v \tag{11}$$

The values of the parameters ω, D, etc. may be found in Table I.

The approximation to the intramolecular bottleneck proceeds as follows. Suppose one is interested in an intramolecular bottleneck corresponding to eq 8 with $j = 4$. Reference 6 showed that this is the main intramolecular bottleneck when $E = -2662$ cm^{-1}. If one assumes $E = H_0$, eq 8 and 9 can be solved for v and n. One may then generate (P,R) points on the surface of section that lie on (actually near to, see remarks below) the zero-order torus by simply determining P and R from the well-known relations between (P,R) and the action-angle variables (n,q).[16] Thus n is held fixed at its previously determined value and q is varied over its entire $(0, 2\pi)$ range to generate an ensemble of (P,R) points. r and p are determined in the same fashion as in section IIA above. Note, of course, because of the coupling in the full system the vibrational action in the r degree of freedom will be slightly different than the value v previously determined, so that the points (P,R,p,r) are only near, not precisely on, the torus with actions n and v. One may propagate the points on the surface of section generated above by one unit on the surface of section, as was done in section IIA, and then estimate the flux out.

Figure 4 shows the approximate (dashed line) and exact (solid line) intramolecular bottleneck or cantorus for an energy $E =$

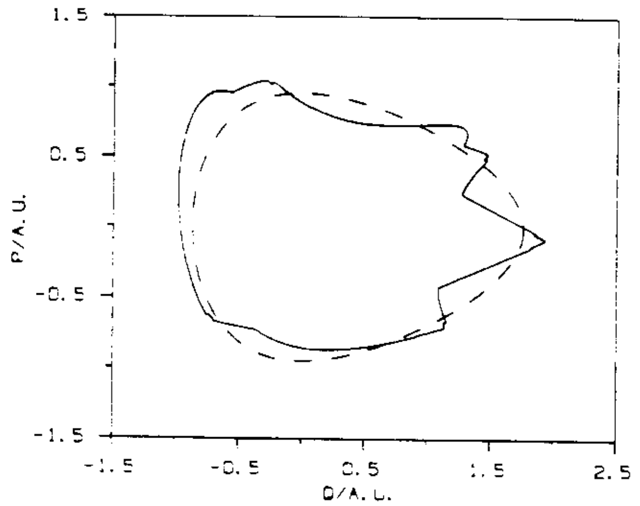

Figure 4. Comparison of exact (solid) and zero-order (dashed) intramolecular bottlenecks for $E = -2662$ cm^{-1}.

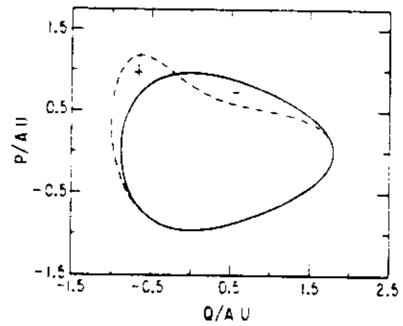

Figure 5. Zero-order intramolecular bottleneck and its propagated counterpart for $E = -2662$ cm^{-1}.

-2662 cm^{-1}, which is the energy corresponding to approximately $v = 20$ and $n = 0$. While the zero-order approximation is in the same general area of the phase space, it does not accurately reproduce the shape of the actual cantorus. This observation is significant because the actual cantorus closely defines one region of stochastic motion. If the zero-order approximation cannot accurately define this structure then it will probably not lead to very good fluxes. Figure 5 displays the result of such a flux calculation for $E = -2662$ cm^{-1}. The results for other energies are similar and are not shown. The fluxes and rates obtained for the relevant energies are given in Table III. It is clear that in all cases the fluxes and rates are overestimated. It appears that, unlike the intermolecular bottlenecks, intramolecular bottlenecks are harder to adequately approximate accurately. Perhaps higher order perturbative schemes, or an adaptation of the Solevev method,[18] will be more successful; we are currently investigating these possibilities.

TABLE III: Intramolecular Bottleneck Rate Data[a]

E, cm^{-1}	v	j[b]	A,[c] au	F, au	$\hbar k^{\text{intra}}$, cm^{-1}
−3683	10	5	4.3 (0.96)	0.15 (0.007)	0.61 (0.12)
−2662	20	4	3.9 (2.2)	0.31 (0.033)	1.19 (0.22)
−1807	30	3	3.2 (2.2)	0.52 (0.050)	1.99 (0.27)

[a] The precise dynamical values of ref 6 are given in parentheses for comparison. [b] The value of j used is based on a knowledge of the actual intramolecular bottlenecks that are of relevance at a given energy.[6] An a priori estimate of j is, however, possible by taking the ratio of $\omega_v(v)$ and $\omega_R(n)$ with van der Waals effective quantum number $n = 0$, say. [c] The exact areas A in brackets have the quasi-periodic area within the cantorus subtracted out. There is no simple a priori way of predicting the quasi-periodic area and so it has not been subtracted out of the zero-order cantorus area. This leads, through cancellation of errors, to zero-order intramolecular rates at lower energies (where there is more quasi-periodic motion) that are better than the corresponding higher energy rates.

III. An Alternative Form for RRKM Theory: A Separatrix-Based Transition State

In view of the success of the zero-order intermolecular bottleneck crossing calculations of section IIA, we now construct a purely statistical theory of unimolecular fragmentation based on such bottlenecks. In section IIIA we present a classical derivation of the general transition-state unimolecular rate constant and then specialize to standard RRKM theory. Section IIIB presents our alternative form for classical RRKM theory.

A. The Transition-State Unimolecular Rate. We present here a classical mechanical derivation of the transition state unimolecular rate constant similar in spirit to treatments by Keck[19] and Wigner.[4] However, one difference between this and earlier work is that to obtain a true variational rate constant a more careful analysis of the nature of the phase space of the unimolecular reactant is required. In this respect the analysis below has borrowed much from Kay's[13] quantum transition-state treatment of unimolecular rate theory. While Kay's derivation was purely quantum mechanical, he inferred a classical mechanical formula, via a correspondence principle argument, that agrees well with our result below.

We define a volume of classical phase space V_A associated with reactants. It is imagined that the initial classical density of points is

$$\rho_0(\mathbf{p},\mathbf{x}) \geq 0, \quad (\mathbf{p},\mathbf{x}) \in V_A \tag{12}$$
$$\rho_0(\mathbf{p},\mathbf{x}) = 0, \text{ otherwise}$$

This distribution function is then assumed to evolve in time, as described by the classical Liouville equation, until a steady-state distribution ρ is reached in the relevant portions of phase space.

Imagine now a closed surface S in the phase space, defined by the equation

$$S(\mathbf{p},\mathbf{x}) = 0 \tag{13}$$

We require that the volume enclosed by S, V_S, includes, but not necessarily equals, the reactant volume V_A. The quantity

$$N_S = \int_{V_S} \mathbf{dp}\,\mathbf{dx}\,\rho \tag{14}$$

is then proportional to the number of phase points inside volume V_S. An alternative way of expressing the above volume integral is

$$N_S = \int \mathbf{dp}\,\mathbf{dx}\,\theta(-S)\rho \tag{15}$$

where it has been assumed S is defined such that when $S(\mathbf{p}, \mathbf{x}) < 0$ the point $(\mathbf{p}, \mathbf{x})$ is inside V_S, and θ is the usual step function

$$\theta(z) = 1, \quad z \geq 0$$
$$\theta(z) = 0, \quad z < 0 \tag{16}$$

If one assumes a first-order rate relation, the total rate of flow of points out of N_S is

$$k = -\frac{\dot{N}_S}{N_S} \tag{17}$$

where the dot above N_S indicates a total time derivative. The time derivative in eq 17 is evaluated as follows

$$\begin{aligned} -\dot{N}_S &= -\int \mathbf{dp}\,\mathbf{dx}\,\dot{\theta}\rho + \dot{\rho}\theta \\ &= -\int \mathbf{dp}\,\mathbf{dx}\,\dot{\theta}\rho \\ &= -\int \mathbf{dp}\,\mathbf{dx}\,\frac{\mathbf{d}\theta}{\mathbf{d}S}\dot{S}\rho \\ &= \int \mathbf{dp}\,\mathbf{dx}\,\delta(S)\,\dot{S}\rho \end{aligned} \tag{18}$$

---

(18) (a) Skodje, R. T.; Borondo, F.; Reinhardt, W. P. *J. Chem. Phys.* **1985**, *82*, 4611. (b) Johnson, B. R. *J. Chem. Phys.* **1985**, *83*, 1204.
(19) Keck, J. C. *Adv. Chem. Phys.* **1967**, *13*, 85.

where the second step follows from Liouville's theorem[20] and the last step is the usual step function/δ function relation.[21] Equation 18 is the basis for deriving Wigner's[4] transition-state rate expression.

While eq 18 is the most useful form for us, it is worthwhile pointing out how the notion of fluxes explicitly comes out of this equation. Equation 18 is mathematically equivalent to a surface integral[22]

$$-\dot{N}_S = \int_{S=0} \mathrm{d}s \, \|\nabla S\|^{-1} \dot{S} \rho \tag{19}$$

where

$$\nabla = \hat{x}_1 \frac{\partial}{\partial x_1} + \hat{x}_2 \frac{\partial}{\partial x_2} + \ldots + \hat{p}_1 \frac{\partial}{\partial p_1} + \ldots \tag{20}$$

and $\mathrm{d}s$ is an element of surface area. Upon introducing

$$\mathbf{v} = \hat{x}_1 \dot{x}_1 + \hat{x}_2 \dot{x}_2 + \ldots + \hat{p}_1 \dot{p}_1 + \ldots \tag{21}$$

and noting that the unit normal to surface S is

$$\mathbf{n} = \|\nabla S\|^{-1} \nabla S \tag{22}$$

eq 19 is seen to be equivalent to

$$-\dot{N}_S = \int_{S=0} \mathrm{d}s \, \mathbf{n}\cdot\mathbf{v}\rho \tag{23}$$

i.e., the flux of points out of surface S. Equation 23 is the starting point for Keck's derivation[19] of the transition-state rate.

Equations 17 and 18 imply the rate of reaction is

$$k = N_S^{-1} \int \mathrm{d}\mathbf{p} \, \mathrm{d}\mathbf{x} \, \delta(S) \, \dot{S} \rho \tag{24}$$

We now specify the steady-state distribution, inspired by Kay's analysis,[13] to be

$$\rho = F_A(\mathbf{p},\mathbf{x}) \, \delta(E - H) \tag{25}$$

where F_A is a characteristic function that is unity if at some time $-T$ in the past the phase point $(\mathbf{p},\mathbf{x})$ was within the reactant volume V_A, and is zero otherwise. T is the time required to establish the steady state and is irrelevant in the sense that it will disappear from the final transition-state expressions.

The inclusion of F_A in eq 25 ensures that the steady state will be consistent with eq 12; i.e., if some region of phase space is inaccessible to the initial reactant, then obviously the steady-state distribution ρ must be zero in this region. More physically, F_A excludes from consideration phase points that lie on scattering trajectories that are direct, and hence do not proceed at all through complexes (i.e., through volume V_A). As applied to a chemical activation study, the introduction of F_A also formally removes from consideration those trajectories lying on quasi-periodic orbits which correspond to complexes but which cannot actually be formed via direct collisions. DeLeon and Berne,[23] as well as Hase, Buckowski, and Swamy,[15] have used similar approaches to remove quasi-periodic motion from consideration in the calculation of a reaction rate. The introduction of F_A is also consistent with the idea of reactant and transition state being in equilibrium, but no products being present in the equilibrium.[24]

There is a simplification that occurs for N_S. Consider the quantity

$$N_A = \int_{V_A} \mathrm{d}\mathbf{p} \, \mathrm{d}\mathbf{x} \, \delta(E - H) \tag{26}$$

which may be written as

$$N_A = \int_{V_S} \tilde{\theta}(\mathbf{p},\mathbf{x}) \, \delta(E - H)$$

where $\tilde{\theta} = 1$ if $(\mathbf{p},\mathbf{x})$ is inside V_A and 0 otherwise. The range of integration may be any volume that includes V_A and we have chosen it to be V_S. Now change the variables to $(\mathbf{p}',\mathbf{x}')$, where $(\mathbf{p}',\mathbf{x}')$ is the phase point that $(\mathbf{p},\mathbf{x})$ evolves to after a time T. Because the nature of Hamiltonian dynamics is such that

$$\frac{\partial(\mathbf{p},\mathbf{x})}{\partial(\mathbf{p}',\mathbf{x}')} = 1 \text{ and } H(\mathbf{p},\mathbf{x}) = H(\mathbf{p}',\mathbf{x}')$$

we have

$$N_A = \int_{V_S} \mathrm{d}\mathbf{p}' \, \mathrm{d}\mathbf{x}' \, \tilde{\theta}(\mathbf{p}(\mathbf{p}',\mathbf{x}'),\mathbf{x}(\mathbf{p}',\mathbf{x}')) \, \delta(E - H)$$

But since $\mathbf{p}(\mathbf{p}',\mathbf{x}')$ and $\mathbf{x}(\mathbf{p}',\mathbf{x}')$ represent the phase point that $(\mathbf{p}',\mathbf{x}')$ evolves to when integrated backwards to a time $-T$, we see that θ in the above equation is precisely $F_A(\mathbf{p}',\mathbf{x}')$ as defined after eq 25. We may then drop the primes in the above equation and conclude that

$$N_A = \int_{V_S} \mathrm{d}\mathbf{p} \, \mathrm{d}\mathbf{x} \, F_A(\mathbf{p},\mathbf{x}) \, \delta(E - H) = N_S$$

The fact that N_S may be replaced by N_A is significant because the latter quantity does not depend on S.

Equation 24 for the rate thus becomes

$$k = N_A^{-1} \int \mathrm{d}\mathbf{p} \, \mathrm{d}\mathbf{x} \, \delta(S) \, \dot{S} F_A \, \delta(E - H) \tag{27}$$

The final vestige of dynamics is removed by assuming

$$F_A(\mathbf{p},\mathbf{x}) \approx \theta(\mathbf{n}\cdot\mathbf{v}) = \theta(\dot{S}) \tag{28}$$

for all points on the critical surface S, which implies that every point with its flow vector pointing outward is assumed to come from the reactant volume V_A. The final, general, unimolecular transition-state rate expression is then

$$k = N_A^{-1} \int \mathrm{d}\mathbf{p} \, \mathrm{d}\mathbf{x} \, \delta(S) \, \dot{S} \theta(\dot{S}) \, \delta(E - H) \tag{29}$$

The rate given by eq 29 is a variational limit in the following sense. The fundamental transition-state approximation, replacing F_A by a step function θ, ensures that the rate given by eq 29 will be an overestimate of the actual rate given by eq 24. Now although the actual rate does not depend on the choice of surface S, as long as S contains V_A, the approximate rate of eq 29 does depend on S. Since eq 29 always overestimates the rate, it follows that S should be chosen so as to minimize the approximate rate. Notice that while eq 29 is an upper bound to eq 24 it may not be an actual upper bound to a dynamically calculated rate, because both eq 24 and 29 have assumed that a certain steady-state distribution (specifically, eq 25) exists. The actual situation may include nonstatistical components such as arise from directly dissociating trajectories and intramolecular bottlenecks. Section IIIC discusses these points further.

Equation 29 takes on a familiar RRKM-like form when the critical surface is given by a condition on coordinates alone. For the sake of argument, and for application later to $\mathrm{HeI_2}$, let us examine a four-dimensional phase space (P,p,R,r) and assume that the coordinates have been chosen so that R is in fact already the critical or reaction coordinate: $S = R - R^\ddagger = 0$ defines the critical surface. Equation 29 is then

$$k_{\mathbf{RRKM}} = N_A^{-1} \int \mathrm{d}P \, \mathrm{d}R \, \mathrm{d}p \, \mathrm{d}r \, \delta(R - R^\ddagger) \frac{P}{\mu} \theta(P) \, \delta(E - H) \tag{30}$$

which is essentially equivalent to Kay's,[13] classical transition-state rate expression. We will refer to eq 30 as the standard RRKM rate although, as noted by Kay,[13] there is a difference in the denominator factor, N_A. Many microcanonical RRKM expressions have a denominator factor N, instead of N_A, that depends on the choice of the critical surface. N is usually taken to be eq 26 with V_A replaced by V_S. Strictly speaking, $k_{\mathbf{RRKM}}$ in this case will not lead to a sensible rate constant because if one takes $R^\ddagger$ to ∞, N will also tend to ∞ and the rate to zero. Thus a variational determination of the rate, as noted by Hase,[25] for example, will

---

[20] Goldstein, H. *Classical Mechanics*; Addison-Wesley: Reading, MA, 1980.

[21] E.g.: Messiah, A. *Quantum Mechanics*; Wiley: New York, 1961; Vol. 1, p 469.

[22] Simple proofs of this are given by: Khinchin, A. I. *Mathematical Foundations of Statistical Mechanics*; Dover: New York, 1949; p 34–35; and also Keck, ref 19.

[23] DeLeon, N.; Berne, B. J. *J. Chem. Phys.* **1981**, *75*, 3495.

[24] Anderson, J. B. *J. Chem. Phys.* **1973**, *58*, 4684.

not lead to a sensible, nonzero rate. Actually it is the flux Nk_{RRKM} that can be minimized in this case and the hope, probably justified for a multidimensional system, is that small variations in $R^{\ddagger}$ about the saddle point position will lead to a minimum in the flux and that N is relatively constant for such variations.

To summarize the results of this section, we have derived, via purely classical mechanical arguments, an expression for the general transition-state unimolecular rate. Equation 30 is what we define to be the standard RRKM rate within this formulation and eq 29 is the more general transition-state rate for an arbitrary surface in phase space.

B. The Separatrix as Basis for the Critical Surface. In view of the success of the intermolecular bottleneck crossing calculations of section IIA and ref 6 in estimating the rate of decay of $\mathrm{HeI_2}$ complexes, we suspect that in many applications the best critical surface S should not be based on a simple configuration space condition such as $R - R^{\ddagger} = 0$ (standard RRKM theory, eq 30), but rather on the intermolecular bottleneck. The simplest approach is to use the zero-order separatrix of section IIA as the critical surface

$$S = h_R(P,R) \tag{31}$$

where h_R is given by eq 5. Thus the condition $S = 0$ determines a $(2N - 1)$-dimensional surface in phase space, where N is the number of degrees of freedom; in the two-dimensional (P,R) plane this surface projects a separatrix curve. For a related problem, remarkably, Wigner[4b] sketched out such a surface almost 50 years ago.

If we now consider a phase space (P,R,p,r) as we did in section IIIA, and insert eq 31 into eq 29, we obtain

$$k = N_A^{-1} \int \mathrm{d}P\, \mathrm{d}R\, \mathrm{d}p\, \mathrm{d}r\, \delta(h_R)\, \dot{h}_R \theta(\dot{h}_R)\, \delta(E - H) \tag{32}$$

$\dot{h}_R$ may be evaluated by the Poisson–Bracket relation[20]

$$\dot{h}_R = \{h_R,H\} = \frac{\partial h_R}{\partial R}\frac{\partial H}{\partial P} - \frac{\partial h_R}{\partial P}\frac{\partial H}{\partial R} \tag{33}$$

If we assume the Hamiltonian has the form of eq 1, we obtain

$$k = N_A^{-1} \int \mathrm{d}P\, \mathrm{d}R\, \mathrm{d}p\, \mathrm{d}r\, \delta(h_R)\, \theta(P)\frac{P}{\mu}|f|\, \delta(E - H) \tag{34}$$

with

$$f(R,r) = \frac{\partial V_R(R)}{\partial R} - \frac{\partial V(R,r)}{\partial R} \tag{35}$$

and where we have used the fact that

$$\int_{-\infty}^{\infty} \mathrm{d}P\, \theta(Pf)\, fPg(P) = \int_{-\infty}^{\infty} \mathrm{d}P\, \theta(P)\, P|f|\, g(P)$$

with $g(P)$ being an even function of P. Actually, utilizing the δ function relation

$$\int \mathrm{d}x\, \delta(y(x)) = \int \mathrm{d}x \sum_k \frac{\delta(x - x_k)}{|y'(x_k)|} \tag{36}$$

where $y(x_k) = 0$ defines the x_k, the integrals over P and p may be evaluated so that eq 34 becomes

$$k = N_A^{-1} \int \mathrm{d}R\, \mathrm{d}r \frac{(2m)^{1/2}|f(R,r)|}{(E + V_R - V)^{1/2}} \tag{37}$$

Equation 37 is the alternative RRKM rate for the case of a two-dimensional system with diagonal kinetic energy.

The above expression may be contrasted with the standard RRKM theory expression which results from evaluating the R, P, and p integrals in eq 30. The result is

$$k_{\mathrm{RRKM}} = N_A^{-1} 2 \int \mathrm{d}r\, [2m(E - V(R^{\ddagger},r))]^{1/2} \tag{38}$$

In this case we see that $N_A k_{\mathrm{RRKM}}$ is a classical action integral[20] along a vibration of the coordinate r, which is normal to the assumed reaction coordinate R. This vibration may be thought of as an elementary (straight) periodic orbit dividing surface (pods).[12] It is important to note that eq 38 can be reexpressed into the more familiar Marcus–Rice[1,2] form

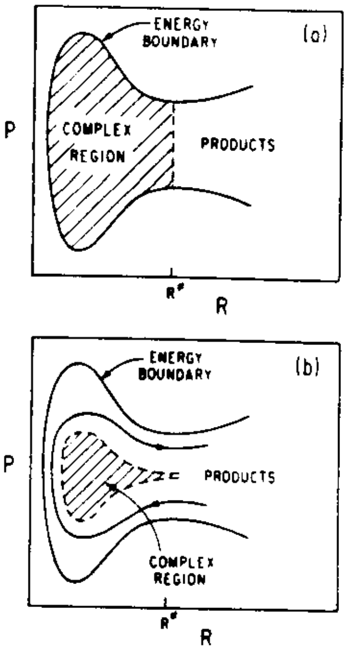

Figure 6. (a) The usual qualitative picture of classical RRKM theory. (b) The alternative view. See section IIIC for further discussion.

$$k_{\mathrm{RRKM}} = \frac{N_{\mathrm{TS}}}{h\rho_{\mathrm{react}}} \tag{39}$$

where

$$N_{\mathrm{TS}} = h^{-1} \int \mathrm{d}r\, \mathrm{d}p\, \theta\left(E - \frac{p^2}{2m} - V(R^{\ddagger},r) \right)$$

$$\rho_{\mathrm{react}} = h^{-2} \frac{\mathrm{d}}{\mathrm{d}E} \int_{V_A} \mathrm{d}P\, \mathrm{d}R\, \mathrm{d}p\, \mathrm{d}r\, \theta(E - H)$$

are the semiclassical sum of states at the transition state and density of states for the reactant. Equation 39 is still purely classical, since it is merely a different form for eq 38. The significance of eq 39, however, is that it leads to the well-known and simple quantum RRKM theory when one replaces, via correspondence principle arguments, N_{TS} and ρ_{react} with their purely quantum mechanical equivalents. While the alternative classical RRKM rate, eq 37, can also be interpreted by an equation like eq 39, the explicit form for N_{TS} in this case is not as easily and unambiguously quantized. However, this should not deter use of eq 37 and related multidimensional analogues in a variety of classical studies, since the required integrals can be evaluated by straightforward numerical methods.

C. Qualitative Discussion of Ordinary and Alternative RRKM Statistical Theories. At this point it is useful to discuss in a qualitative fashion the differences between the ordinary and alternative forms of RRKM theory that are the subjects of this paper. Figure 6 summarizes clearly the major qualitative features. Figure 6a represents a frequently used qualitative picture of RRKM theory.[1c] In this picture complexes exist for $R < R^{\ddagger}$ and all phase space consistent with energy conservation. (Of course in a two-degree-of-freedom problem, Figure 6 could be a surface of section; for higher dimensionalities it is a schematic representation of motion in the reduced phase space of the critical degree of freedom.) One difficulty with this assumption concerning the critical surface is that in reality complexes do not exist merely for $R < R^{\ddagger}$, but rather in a more restricted portion of phase space. What we define to be ordinary RRKM theory (eq 30)

---

(25) Hase, W. L. *Acc. Chem. Res.* **1983**, *16*, 258.

partly accounts for this fact by having a density of states factor N_A that is evaluated only in this restricted part of phase space. However, as we shall see later in section IVB, this does not necessarily lead to a better rate. In many situations, of course, it is expected that there is not a significant difference between all phase space consistent with energy conservation and $R < R^{\ddagger}$, and the restricted portion of phase space. The realization of this expectation accounts for some of the great success of classical RRKM theory.

Figure 6b shows what is closer to the real situation in certain problems, such as van der Waals molecule fragmentation. Complexes exist only within the separatrix branches (dashed curve). Now imagine arbitrary critical surfaces $S(P,R) = 0$ that are closed and contain at least all of the complex region. Then the standard RRKM surface defined by drawing a vertical line at $R = R^{\ddagger}$ and connecting to the energy boundary to form a closed surface will overestimate the forward flux (and rate, if N_A is held constant for variations in S) because it includes direct scattering trajectories, such as the solid line with the arrow on it. Such direct scattering trajectories have nothing to do with the complexes. If we assume that the intermolecular bottleneck is the only bottleneck to flow in the classical phase space then the rate calculated from the flux across this bottleneck is the minimum for any surface that encloses the intermolecular bottleneck. Furthermore, in this very idealized limit the corresponding rate constant would be exact. However, it is important to stress the word "idealized" in the sentence for two reasons. First, our statistical theory in practice is not based on the exact intermolecular bottleneck but on an approximation to it. Second, and more fundamentally, the actual classical dynamics can exhibit additional bottleneck effects. For example, if there is an intramolecular bottleneck within the intermolecular bottleneck, and if the characteristic rate of flow of points across the intramolecular bottleneck is smaller than the intermolecular bottleneck crossing rate, then ensembles of phase points with appreciable density within the intramolecular bottleneck will exhibit a much *smaller* rate of fragmentation than that predicted by the intermolecular bottleneck crossing rate alone.[6] Thus the statistical rate is not necessarily an upper bound to the dynamic rate, a point that was also made in section IIIA.

IV. Applications of the Alternative RRKM Rate Expression

A. T-Shaped HeI$_2$ Predissociation. We now apply eq 37 to the T-shaped model for HeI$_2$ predissociation, previously discussed in section II and ref 6 and 16. V_R is then the effective He–I$_2$ interaction (Appendix, ref 16)

$$V_R(R) = D\{e^{-2\alpha(R-R)} - 2e^{-\alpha(R-R)}\} - D \tag{40}$$

and V is the full coupled oscillator potential given by eq 2.

The N_A factor of eq 37, essentially the reactant density of states, is approximated analytically by noting that

$$N_A = \int_{V_A} \mathrm{d}P\,\mathrm{d}R\,\mathrm{d}p\,\mathrm{d}r\,\delta(E - H)$$

$$= \frac{\mathrm{d}}{\mathrm{d}E}\int_{V_A} \mathrm{d}P\,\mathrm{d}R\,\mathrm{d}p\,\mathrm{d}r\,\theta(E - H)$$

$$= \frac{\mathrm{d}}{\mathrm{d}E}\int \mathrm{d}P\,\mathrm{d}R\,\mathrm{d}p\,\mathrm{d}r\,\theta(-h_R(P,R))\,\theta(E - H) \tag{41}$$

Equation 41 is still exact, but we now let H be represented by its separable approximation, eq 4, to obtain

$$N_A \approx \frac{\mathrm{d}}{\mathrm{d}E}\int \mathrm{d}P\,\mathrm{d}R\,\mathrm{d}p\,\mathrm{d}r\,\theta(-h_R)\,\theta\left(E - h_R - \frac{p^2}{2m} - V_{\mathrm{BC}}\right) \tag{42}$$

Finally, since the first step function restricts (P,R) to energies between $-D$ and 0, where D is the van der Waals dissociation energy, and these energies are small compared to E and the I$_2$ energies of interest, we neglect the h_R term in the second step function to obtain

TABLE IV: Fragmentation Rates for the T-Shaped HeI$_2$ Model

E, cm^{-1}	v	standard RRKM, cm^{-1}	alt RRKM, cm^{-1}	dynamical,[a] cm^{-1}
−3863	10	66.0	0.52	0.007
−2662	20	110.5	0.80	0.17
−1807	30	135.7	1.09	0.56
−574	50	128.0	1.89	1.57

[a] From ref 6; see also footnote *d* under Table II.

$$N_A \approx \frac{\mathrm{d}}{\mathrm{d}E}\int \mathrm{d}P\,\mathrm{d}R\,\mathrm{d}p\,\mathrm{d}r\,\theta(-h_R)\,\theta\left(E - \frac{p^2}{2m} - V_{\mathrm{BC}}\right)$$

$$= \left[\int \mathrm{d}P\,\mathrm{d}R\,\theta(-h_R)\right]\left[\int \mathrm{d}p\,\mathrm{d}r\,\delta\left(E - \frac{p^2}{2m} - V_{\mathrm{BC}}\right)\right]$$

= area of the zero-order separatrix × $2\pi\hbar$ ×
I$_2$ semiclassical density of states

Employing the Morse oscillator relationships summarized in Appendix A, we then obtain

$$N_A \sim \frac{4\pi D}{\omega}\,\frac{2\pi}{\omega_{\mathrm{BC}}[1 - (E + D_{\mathrm{BC}})/D_{\mathrm{BC}}]^{1/2}} \tag{43}$$

In eq 43 it will be recalled that E is measured relative to the separated atoms as zero. Equation 43's validity has been checked by comparing its predictions with a direct Monte Carlo evaluation of the exact N_A, eq 26, and has been found to be within a few percent of the exact result for the energies of interest to us.

Having obtained N_A, we are left with the task of evaluating the two-dimensional integral over R and r, eq 37. This is trivially done via numerical integration, taking R to range from $R_{\min}$, the minimum value of R allowed by eq 31, to some large value, say $R = 20a_0$; the limits on r may be taken to be $r_{\min}$ and $r_{\max}$, the inner and outer tuning points when all the energy E is in the I$_2$ bond. In evaluating the integrals over momentum analytically to obtain eq 37, it has been implicitly assumed that the range of R and r is such that $V < E$. Thus any points (R,r) that lead to $V > E$ must be rejected as not lying in the range of integration. The results of these simple calculations are displayed in Table IV. We compare the rates obtained to the "exact" rates of fragmentation obtained from classical trajectory simulations[6] and also to what standard RRKM theory predicts.

The standard RRKM calculations were carried out by considering $R^{\ddagger}$ as a variational parameter, similar in spirit to Adams'[26] Monte Carlo RRKM calculations of van der Waals predissociation. When the rate is viewed in this fashion there is no difficulty with the fact that there is no saddlepoint on the potential energy surface for HeI$_2$. Simple numerical calculations showed that a minimum rate is achieved as $R^{\ddagger} \rightarrow \infty$. Equation 38 is then simply the ratio of an action integral for an I$_2$ Morse oscillator and N_A. The resulting analytical formula, inferred from the Morse oscillator relationships in Appendix A, is

$$k_{\mathrm{RRKM}} = \frac{D_{\mathrm{BC}}\omega}{2\pi D}(x(E) - x^2(E)) \tag{44}$$

with

$$x(E) = [1 - (E + D_{\mathrm{BC}})/D_{\mathrm{BC}}]^{1/2}$$

Equation 44 must be distinguished from other simple RRKM or RRK rate expressions that may be encountered in the literature. The main difference is that N_A, given by eq 43 and used in deriving eq 44, is appropriate to a van der Waals system where the phase space region associated with the van der Waals bond is much smaller than that associated with the I$_2$ bond. If one employs, for example, the simple RRK rate expression,[1] which ignores such

---

(26) Adams, J. E. *J. Chem. Phys.* 1983, *78*, 1275.

subtle points, one finds, keeping in mind that for the energies of interest to us the van der Waals dissociation energy $D \ll |E|$, that the rate is $\sim\omega/2\pi \sim 4$ cm^{-1}, i.e., approximately constant and equal to the van der Waals vibrational frequency. The reader should also not confuse this form of the theory with certain phenomenological versions of RRKM theory[1] that have been designed to describe complicated unimolecular reactions where the potential energy surface is only poorly known, if at all. Rather, what we mean by standard RRKM theory is an explicit evaluation of the fundamental classical RRKM expression, eq 30, and equivalent forms such as eq 44, using the full potential and a consistent definition of the density of states term N_A. This represents the essential approximation of RRKM theory, without any additional, simplifying assumptions. However, this does not mean that eq 44 will yield a better result than even simple RRK theory. Indeed, through cancellation of errors, the simple RRK result quoted above is better than the standard RRKM result, although not better than our alternative RRKM result.

Table IV makes it clear that the alternative RRKM rate, eq 37, leads to predictions in reasonable accord with the exact rates. Thus, although the fragmentation rate for the lowest energy studied is dominated by the influence of intramolecular bottlenecks, as noted in section IIA, and is poorly described by any simple rate theory, the alternative RRKM rate improves as energy is increased, and leads to very reasonable rates for energies between -2662 and -573 cm^{-1}. The predictions of standard RRKM theory, eq 44, are always grossly in error. Of course, for the example we have considered, van der Waals molecular fragmentation, it is not surprising that RRKM theory fails. However, it is surprising and very encouraging that simply by employing a different kind of transition state, one based on a separatrix, an alternative statistical theory can lead to a reasonable prediction of the predissociation rate for this system.

One way to understand the success of the alternative RRKM theory for HeI$_2$ predissociation is to note that the separatrix-based transition-state surface enforces naturally a dynamical "selection rule" that I$_2$ lose only a small amount of vibrational energy when the complex breaks up to form He + I$_2$. Quantum mechanically,[17] for example, it is known that there is a very high probability for I$_2$ to lose just one vibrational quantum. Classically, the amount of vibrational energy loss is even less.[6] The maximum van der Waals momentum $P_{\max}$ on the separatrix is just $(2\mu D)^{1/2}$, which corresponds to a translational energy of $D = 36$ cm^{-1}. If the flux out of the separatrix surface is not too large, then D provides a rough upper limit to the maximum product relative translational energy or the corresponding I$_2$ vibrational energy loss.

The remarks in the above paragraph suggest a simple amendment to standard RRKM theory that may improve its somewhat dismal performance in this example. One can incorporate the dynamical selection rule approximately by limiting the P integration in eq 30 to an upper limit $P_{\max} = (2\mu D)^{1/2}$. Actually, in this case it is easy to show that eq 30, with $R^{\ddagger} = \infty$, reduces to

$$k_{\rm RRKM}' = N_A^{-1}[I(E) - I(E - D)] \qquad (45)$$

where $I(E)$ is the action integral for an I$_2$ Morse oscillator, as given in Appendix A. A prime is used in eq 45 to remind the reader that an additional assumption, that the van der Waals momentum range be restricted, has been made. Equation 45 is trivially evaluated with the result that $k_{\rm RRKM}'$ is a slightly decreasing function with energy over the energy range of interest, which is of course incorrect. However, the decrease is only about 1% over the range of interest and one may take this rate to be approximately constant at $\hbar k_{\rm RRKM}' \sim 2.1$ cm^{-1}. Thus the magnitude, but not the functional behavior with energy, of the standard RRKM rate can be greatly improved by the simple amendment. The alternative RRKM rate of Table IV is always lower than $\hbar k_{\rm RRKM}'$ and shows a much more reasonable energy dependence. Thus it is clear that while the restriction on the momentum is an important component of the success of the alternative RRKM theory, the actual shape of the separatrix, which is not accounted for by $\hbar k_{\rm RRKM}'$, is important for obtaining the best results.

B. Three-Dimensional HeI$_2$ Predissociation Rates, $J = 0$. The alternative version of RRKM theory can be applied to systems with more than two degrees of freedom, which we illustrate with an application to HeI$_2$ predissociation with total angular momentum $J = 0$. We show in Appendix B that the exact classical Hamiltonian for a three atom system with $J = 0$ is given by

$$H(P,p,j,R,r,\gamma) = \frac{P^2}{2\mu} + \frac{p^2}{2m} + \frac{j^2}{2}\left(\frac{1}{\mu R^2} + \frac{1}{mr^2}\right) + V(R,r,\gamma) \qquad (46)$$

The new feature, relative to our previous considerations, is that there is another pair of canonically conjugate variables, namely (j, γ). j is the rotational action variable associated with the diatomic I$_2$ or equivalently, since $J = 0$, the orbital angular momentum l between He and I$_2$; γ is the angle between the vector connecting the center of mass of I$_2$ to He and the I$_2$ bond vector. The potential V is now given by

$$V = V_{\rm XB}(R_{\rm XB}) + V_{\rm XB}(R_{\rm XC}) + V_{\rm BC}(r) \qquad (47)$$

where, as before, $V_{\rm XB}$ denotes the Morse potential between He and an I atom, $V_{\rm BC}$ is the I$_2$ Morse potential, and now $R_{\rm XB}$ and $R_{\rm XC}$ are not equal but given by

$$R_{\rm XB} = (R^2 + r^2/4 + Rr\cos\gamma)^{1/2}$$
$$R_{\rm XC} = (R^2 + r^2/4 - Rr\cos\gamma)^{1/2} \qquad (48)$$

We use in this calculation the same Morse potential parameters as earlier (Table I) because Delgado-Barrio et al.[27] have calculated, via classical trajectories, rates of fragmentation for three-dimensional, $J = 0$, HeI$_2$ with these parameters.

We now choose an appropriate separatrix-based surface S and use the Wigner form for the rate, eq 29. Certain of the integrals involved may be evaluated analytically and the remaining ones can be evaluated via Monte Carlo integration.[26,28] Although the total angular momentum is zero it is important to realize that there is still diatomic (or orbital) rotation and the centrifugal term in eq 46 leads to a very different separatrix structure than previously studied by us.

We define an effective potential by

$$V_{\rm eff}(R;j,\gamma) = \frac{j^2}{2}\left(\frac{1}{\mu R^2} + \frac{1}{m\bar{r}_{\rm BC}^{\,2}}\right) + V(R,\bar{r}_{\rm BC},\gamma) \qquad (49)$$

Appendix C discusses the nature of $V(R,\bar{r}_{\rm BC},\gamma)$. Figure 7a depicts $V_{\rm eff}$ for $j = 10\hbar$ and $\gamma = \pi/2$. A centrifugal maximum is evident and if one defines an approximate Hamiltonian for the R degree of freedom as

$$h = \frac{P^2}{2\mu} + V_{\rm eff}(R;j,\gamma) \qquad (50)$$

the phase curves appear as shown in Figure 7b. The separatrix is given by the dashed line and is quite different from the nonrotating T-shaped HeI$_2$ separatrices in that there is a fixed point for $P = 0$ and a finite value of R corresponding to the barrier maximum position, $R = R^{\ddagger}$. For $j > 0$ the energy of the separatrix is no longer zero (as in the T-shaped model) but some positive value ϵ_s which is a function of j and γ. Of course for $j = 0$, $\epsilon_s = 0$ and the separatrices are like those for T-shaped HeI$_2$. Appendix C discusses a simple procedure for determining the approximate functional dependence of ϵ_s on j and γ, as well as a similar representation of the barrier height position, $R^{\ddagger}(j,\gamma)$. In the nonzero centrifugal barrier case not all branches of the separatrix bound complexes, rather only those branches with $R < R^{\ddagger}$. We are thus led to the separatrix surface

$$S(P,j,R,\gamma) = \frac{P^2}{2\mu} + V_{\rm eff}(R;j,\gamma) - \epsilon_s(j,\gamma) \qquad (51)$$

---

(27) Delgado-Barrio, G.; Villarreal, P.; Mareca, P.; Albelda, G. *J. Chem. Phys.* **1983**, *78*, 280.

(28) E.g.: Porter, R. N.; Raff, L. M. In *Modern Theoretical Chemistry*; Miller, W. H., Ed.; Plenum: New York, 1976; Vol. 2, p 1.

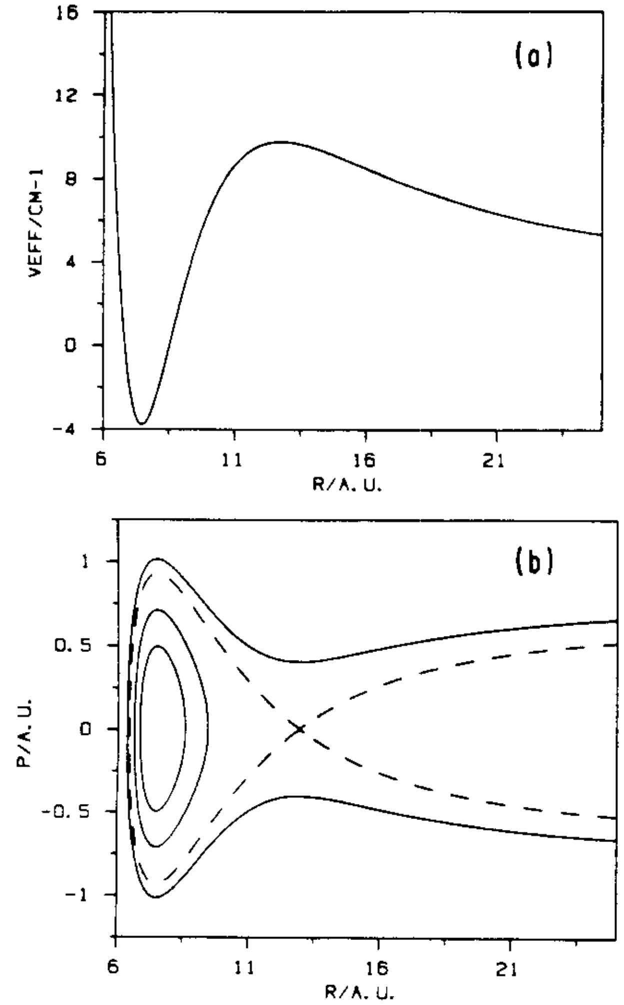

Figure 7. (a) Effective potential for $j = 10$ and $\gamma = \pi/2$. (b) Phase curves for the effective potential in (a). The separatrix is given by the dashed curve.

For fixed j and γ, the condition $S = 0$ determines a separatrix such as the dashed line shown in Figure 7b. We have not explicitly put the condition that complexes exist only for $R < R^{\ddagger}$ into eq 48, although we could have with a step function; rather, we choose to restrict the range of integration appropriately, as will be discussed below.

Equation 51 may be inserted into eq 29 and the integral over p evaluated. Using eq 36 we find

$$N_A k = \int \mathrm{d}P\, \mathrm{d}R\, \mathrm{d}r\, \mathrm{d}j\, \mathrm{d}\gamma \frac{(2m)^{1/2}\delta(S)\dot{S}\theta(\dot{S})}{\left[E - \frac{P^2}{2\mu} - \frac{j^2}{2}\left(\frac{1}{\mu R^2} + \frac{1}{mr^2}\right) - V(R,r,\gamma)\right]^{1/2}}$$

The integral over P may be evaluated similarly to yield

$$N_A k = \int \mathrm{d}R\, \mathrm{d}r\, \mathrm{d}j\, \mathrm{d}\gamma \sum_{k=1}^{2} \frac{(2m)^{1/2}\mu\dot{S}_k\theta(\dot{S}_k)}{|P_k|\left[E - \frac{P_k^{\,2}}{2\mu} - \frac{j^2}{2}\left(\frac{1}{\mu R^2} + \frac{1}{mr^2}\right) - V\right]^{1/2}} \qquad (52)$$

where

$$P_k = \pm[2\mu(\epsilon_s - V_{\mathrm{eff}})]^{1/2}$$

$$\dot{S}_k = \left[\frac{\partial S}{\partial R}\frac{\partial H}{\partial P} + \frac{\partial S}{\partial \gamma}\frac{\partial H}{\partial j} - \frac{\partial S}{\partial P}\frac{\partial H}{\partial R} - \frac{\partial S}{\partial j}\frac{\partial H}{\partial \gamma}\right]_{P=P_k}$$

N_A can also be evaluated partially by carrying out the integral over p, reducing eq 26 to

$$N_A = \int \mathrm{d}P\, \mathrm{d}R\, \mathrm{d}r\, \mathrm{d}j\, \mathrm{d}\gamma \frac{(2m)^{1/2}\theta(-S)}{\left[E - \frac{P^2}{2\mu} - \frac{j^2}{2}\left(\frac{1}{\mu R^2} + \frac{1}{mr^2}\right) - V\right]^{1/2}} \qquad (53)$$

For comparison, a standard RRKM rate can also be defined by introducing a critical surface

$$S = R - R^{\ddagger}(j,\gamma) \qquad (54)$$

into eq 29. The condition $S = 0$ then corresponds to the usual prescription that the transition state be at the barrier maximum position. However, as with the nonrotating T-shaped HeI$_2$ example, using $S = 0$ will lead to rates almost 2 orders of magnitude bigger than the alternative RRKM rates. While this represents a failure of classical RRKM theory in its most essential form, the simple amendment introduced in section IVA, that the van der Waals momentum be restricted to lie only within the values permitted by the separatrix branches, will improve the situation. Thus, insertion of eq 54 into eq 29, along with the above momentum restriction, leads to

$$N_A k_{\mathrm{RRKM}}' = \int \mathrm{d}P\, \mathrm{d}r\, \mathrm{d}j\, \mathrm{d}\gamma \frac{(2m)^{1/2}\dot{S}^{\ddagger}\theta(\dot{S}^{\ddagger})\theta(|P| - P_s(j,\gamma))}{\left[E - \frac{P^2}{2\mu} - \frac{j^2}{2}\left(\frac{1}{\mu R^{\ddagger 2}} + \frac{1}{mr^2}\right) - V(R^{\ddagger},r,\gamma)\right]^{1/2}} \qquad (55)$$

with

$$\dot{S}^{\ddagger} = \left[\frac{\partial S}{\partial R}\frac{\partial H}{\partial P} + \frac{\partial S}{\partial \gamma}\frac{\partial H}{\partial j} - \frac{\partial S}{\partial j}\frac{\partial H}{\partial \gamma}\right]_{R=R^{\ddagger}}$$

and where $P_s(j,\gamma)$ is the maximum momentum along the $R < R^{\ddagger}$ separatrix branches. The numerical approximation of P_s is discussed in Appendix C.

Equations 52, 53, and 55 are four- or five-dimensional integrals that can be conveniently evaluated by Monte Carlo integration.[26,28] For example, if we denote the argument of the integral in eq 52 as F, we have

$$\int \mathrm{d}R\, \mathrm{d}r\, \mathrm{d}j\, \mathrm{d}\gamma\, F \simeq (R_{\max} - R_{\min})(r_{\max} - r_{\min})j_{\max}\frac{\pi}{2}\,\frac{1}{L}\sum_{\mathbf{k}} F_{\mathbf{k}}$$

where $\mathbf{k}$ denotes a set of four random numbers $(\zeta_1,\zeta_2,\zeta_3,\zeta_4)$ between 0 and 1, and $F_{\mathbf{k}}$ is the argument of the integral evaluated for

$$R = R_{\min} + (R_{\max} - R_{\min})\xi_1$$

$$r = r_{\min} + (r_{\max} - r_{\min})\xi_2$$

$$j = j_{\max}\xi_3$$

$$\gamma = \frac{\pi}{2}\xi_4$$

and L is the number of different times the random number vector is evaluated.

The actual range of integration, as for the nonrotating T-shaped model, must be carefully considered. The minimum and maximum R values are given by the absolute minimum and maximum allowed by eq 51 with $S = 0$. These values turn out to be those for $j = 0$ and $\gamma = \pi/2$. $R_{\max}$ is actually infinity but may be taken to be a suitably large value, say $25a_0$. The minimum and maximum r values are as in the T-shaped case, section IVA. Of course, points that lead to negative square root arguments lie outside the integration range of interest. A new and very important feature in the present calculation is the existence of an upper limit on j for complexes to exist. Appendix C notes that a minimum in the effective potential, for a given value of γ, does not exist for j greater than a certain value. We associate complexes with the existence

TABLE V: Fragmentation Rates for Three-Dimensional HeI_2, $J = 0$

E,[a] cm^{-1}	v	$\hbar k'_{\mathrm{RRKM}}$, cm^{-1}	$\hbar k$,[b] cm^{-1}	dynamical,[c] cm^{-1}
−2662	20	1.79	1.52	0.06
−2213	25	1.82	1.89	0.10
−1807	30	1.83	2.39	0.16
−1442	35	1.81	2.82	0.24

[a] These energies were chosen to correlate with the two-dimensional case. The actual energies used by Delgado-Barrio et al.[27] were about 4 cm^{-1} higher, which is an insignificant difference for our purposes. [b] Both the alternative RRKM ($\hbar k$) and momentum-restricted RRKM ($\hbar k'_{\mathrm{RRKM}}$) rates are converged to about 10%. [c] From Figure 2 of ref 27. Note these authors present half-widths, not full widths, so their results have been multiplied by 2 for comparison with ours. The v = 20 result is an extrapolation.

of such a minimum. A simple parameterization of this upper limit to j is given by eq C4. We use $j_{\max} = 17.5\hbar$, which is slightly larger than the largest j_{complex} value, and points are rejected in the Monte Carlo integration if $j > j_{\mathrm{complex}}(\gamma)$. Note that the magnitude of j allowed solely by energy conservation, for the energies of interest to us, will be an order of magnitude larger than j_{complex}, which is typically $16\hbar$, so that the restriction noted above, which we will apply to both the standard and alternative RRKM rates, is very important. Complexes are also restricted to exist only within those branches of the separatrix for which $R < R^{\ddagger}$, thus excluding the portion of phase space within the separatrix but with $R > R^{\ddagger}$. This means that in all the integrals points that have $R > R^{\ddagger}$ are also omitted. It will be recalled that in the T-shaped case, $R^{\ddagger}$ was effectively infinity so that this final restriction never explicitly entered.

Equations 52, 53, and 55 were evaluated via the Monte Carlo procedure described above, and the results are displayed in Table V, where they are also compared with the classical trajectory results of Delgado-Barrio et al.[27] The entire calculation reported in Table V required 10 h of CPU time on a VAX 750 minicomputer. While this is not an excessive computational effort, it should be noted that evaluation of the alternative and momentum restricted standard RRKM rates required about the same computation effort, that the criterion of convergence used was stricter than might normally be required, and that no special effort to economize via use of alternative Monte Carlo sampling procedures was made. Table V shows that the three-dimensional HeI_2 fragmentation is not as well described by the alternative RRKM theory as is two-dimensional fragmentation. For example, even for energies as high as $E = -1442$ cm^{-1} there is about a factor of 10 discrepancy between the alternative RRKM and the trajectory determined fragmentation rates. The momentum-restricted RRKM results, as in the T-shaped HeI_2 model study, are approximately constant over the energy range of interest, which is qualitatively incorrect behavior. Somewhat fortuitously, the corresponding approximate value of $\hbar h_{\mathrm{RRKM}}'$ is slightly smaller than our alternative RRKM rates over most of the energy range studied here. There are a number of possible sources of difficulty that lead to the alternative RRKM rate being somewhat high in the example under discussion. For example, there could be strong intramolecular bottleneck effects, as were present in the $E = -3683$ cm^{-1} two-dimensional fragmentation studies. This would imply that the rate we calculate may well be a reasonable intermolecular bottleneck crossing rate, but that the intermolecular bottleneck rate itself is not sufficient to describe the fragmentation dynamics. It is also possible that our approximation to the separatrix surface in the three-dimensional case is not as accurate as that in the two-dimensional case. If our separatrix model is correct, and it is intramolecular bottleneck effects that are causing the discrepancy evident in Table V, we expect that there will be much better agreement between the alternative RRKM and dynamical fragmentation rates for higher energies. Unfortunately, Delgado-Barrio et al.[27] only carried out their calculations to about $E = -1442$ cm^{-1}. From the limited range of energies studied, however, the behavior of the dynamical rate constant is consistent with the dominance of a smaller intramolecular rate at low energy and the growing importance of a larger intermolecular rate as energy is increased. Indeed the rather fast variation of the dynamical rate over the small energy range studied may suggest that one is in fact passing through a transition point between these decay modes, which could account for the discrepancy between alternative RRKM and dynamical rates, since the alternative RRKM model assumes only an intermolecular decay mode.

V. Discussion

This paper has been concerned with how the rates of crossing of bottlenecks in the classical phase space determine the rate of unimolecular fragmentation. We have shown, with application to the problen of predissociation of the van der Waals molecule HeI_2, that the intermolecular bottleneck that separates complexes from fragments can be well approximated by a zero-order separatrix. The rate of crossing of this separatrix is in reasonable accord with that calculated from the rate of crossing of the precise bottleneck.[6] Furthermore, the intermolecular bottleneck crossing rate, particularly at higher energies, was found to be a good approximation to the actual fragmentation rate of HeI_2. A related approximation for the intramolecular bottlenecks that occur within the region of phase space associated with complexes proved less successful.

The success of the zero-order separatrix approximation to the intermolecular bottleneck suggests that a unimolecular transition-state theory, which we term alternative RRKM theory, can be developed by using the zero-order separatrix as transition state. This alternative RRKM theory predicts rates better than standard RRKM theory for both two- and three-dimensional models of HeI_2 predissociation. Consideration of the reasons for the success of the alternative RRKM rate also lead to a simple way of modifying the standard RRKM rate, by restricting appropriately the reaction coordinate momentum. The amended standard RRKM rate has the correct order of magnitude over the energy range of interest, but shows only a weak energy dependence, a result in contradiction with both the alternative RRKM and dynamical rate constants. This fact further serves to emphasize the role of the separatrix shape in determining the best approximation to the rate constant for the HeI_2 system.

The HeI_2 predissociation example is rather extreme. In other examples of unimolecular reactions it may be the case that a separatrix-based critical surface calculation would lead to rates comparable to those predicted by standard RRKM theory. This could happen, for example, when the separatrix branches are close to the energy boundary in Figure 6. Related to this situation is the case of strong coupling where most of the trajectories in the part of phase space within the unimolecular barrier are chaotic. The inner branches of the separatrix that define complexes may then be considered to have broken up. However, most trajectories that cross the barrier also have been within any approximate construction of the separatrix and therefore both alternative and standard RRKM approaches should yield similar results. The reader will recognize this latter situation as being the typical picture of standard RRKM theory which has proven to be so successful in describing such strongly coupled situations (Figure 6a). Therefore we emphasize again that the theory presented in this paper is not a replacement for RRKM theory, but is an alternative way of applying it when the problem at hand is such that the intermolecular bottleneck is a more severe restriction on the flow in phase space than is the energy conservation requirement. Just this situation occurs for the fragmentation of van der Waals molecules because the van der Waals bond dissociation energy is much smaller than the dissociation energy of the molecular partner. Thus the maximum possible momentum along the separatrix is much smaller than the upper limit based on energy conservation. For example, for HeI_2, if $E = -2662$ cm^{-1} the maximum separatrix momentum $(2\mu D)^{1/2}$ is a factor of 8 smaller than the energy conservation limit, leading to a severe restriction on the phase space.

We believe the theory presented in this paper is worthy of further study. In particular, we believe it worthwhile to study application of the theory to a greater variety of unimolecular reactions. An obvious criticism of the theory is that it depends

TABLE VI: Effective Potential Data

γ, deg	D_γ, cm^{-1}	α_γ, au	R_γ, au
0	19.2	0.6030	10.358
30	19.9	0.5924	9.808
60	24.7	0.5691	8.317
90	36.0	0.5589	7.002

TABLE VII: Portions of the R^1 and ϵ_j Grids

	γ, deg			
$j(\hbar)$	0	30	60	90
		R^1, au		
2	23.219	22.701	21.464	20.679
6	18.411	17.825	16.417	15.524
10	15.963	15.310	13.722	12.721
14	14.109	13.339	11.348	10.134
		ϵ_j, cm^{-1}		
2	0.21	0.22	0.23	0.24
6	2.39	2.47	2.69	2.85
10	7.69	8.04	9.05	9.86
14	17.14	18.17	21.41	24.16

on an incompletely designed zero-order analysis of the classical Hamiltonian, in the sense that there is no prescription for the optimum choice of zero-order approximation. Only through more applications will any sort of generic "algorithm" for choosing the optimum separatrix become apparent. It seems likely to be useful to couple our ideas with the reaction path Hamiltonian method of Miller and co-workers.[29] The reaction path Hamiltonian method provides a natural means of obtaining, from either ab initio data or possibly a complicated analytical potential form, the potential energy dependence along the reaction coordinate, which could provide a very useful means of obtaining reasonable zero-order separatrices.

Of even greater interest is the development of a quantum mechanical analogue of the classical theory we have discussed. The measure of success of standard RRKM theory is evident in the observation that its quantum mechanical version is now a routine tool of experimental kineticists. While the classical mechanical alternative RRKM rate theory yields rates within a factor of 5–10 of the exact classical mechanical fragmentation rates for HeI_2, the classical mechanical rates are themselves a factor of three[16] greater than the most accurate quantum mechanical rates.[17] But what is the proper quantum mechanical analogue of a separatrix? Furthermore, even a direct quantum analogue of the theory may not fully account for this discrepancy. For example, there may be difficulties with properly accounting for dynamical tunneling (or reflection) effects.[6,16] It should also be noted that the simple arguments used in deriving a practical quantum RRKM theory involve certain separability assumptions that cannot be made for the case of a separatrix-based surface; one may need to resort to using somewhat more sophisticated ideas such as those used by Miller[30] in deriving his nonseparable quantum transition-state theory for bimolecular reactions.

Acknowledgment. This research has been supported by the NSF and AFOSR (S.K.G. and S.A.R.) under NSF CHE 83 19163 and AFOSR -86-0006. One of us (M.J.D.) was supported by the Office of Basic Energy Sciences, Division of Chemical Sciences, U.S. Dept. of Energy, under contract No. W-31-109-ENG-38. S.K.G. thanks Dr. Frank Novak for helpful discussions.

Appendix A

Morse Oscillator Relationships. We summarize here the classical Morse oscillator relationships of relevance to the present paper. Consider a particle of mass m in a Morse oscillator potential

$$V_{BC} = D_{BC}\{\exp(-2\alpha_{BC}(r - r_{BC})) - 2\exp(-\alpha_{BC}(r - r_{BC}))\} \quad \text{(A1)}$$

where the zero of energy is the separated atoms. The classical action integral

$$I(E) = 2\int \mathrm{d}r[2m(E - V_{BC}(r))]^{1/2} \quad \text{(A2)}$$

may be evaluated analytically[31] and is

$$I(E) = \frac{4\pi D_{BC}}{\omega_{BC}}\{1 - [1 - (E + D_{BC})/D_{BC}]^{1/2} \quad \text{(A3)}$$

where, of course, $\omega_{BC} = (2D_{BC}\alpha_{BC}^2/m)$. The action variable v is given by

$$v + \tfrac{1}{2} = \frac{I(E)}{2\pi\hbar} \quad \text{(A4)}$$

where the $^1/_2$ term is inserted to make the correspondence principle connection with a quantum number but is negligible for large v (the classical limit). The semiclassical density of states is then

$$\frac{\mathrm{d}v}{\mathrm{d}E} = \frac{1}{\hbar\omega_{BC}[1 - (E + D_{BC})/D_{BC}]^{1/2}} \quad \text{(A5)}$$

In section IVA, eq A5 is used to obtain eq 42. Also required for that equation is the phase space area of the separatrix for a Morse oscillator corresponding to the van der Waals degree of freedom. This may be obtained from eq A3 by dropping the BC subscripts and setting $E = 0$.

Appendix B

Classical Hamiltonian for $J = 0$. In this Appendix we outline how the full classical Hamiltonian for an atom–diatom system reduces to eq 46 of the text when the total angular momentum $J = 0$. While it might be argued that eq 46 is rather obvious, it is curious that it has not been used very much in classical dynamics studies. This Appendix relies heavily on Appendix C of ref 32, where many useful transformation relations are given.

The full classical Hamiltonian in the center of mass system is

$$H = \mathbf{P}\cdot\mathbf{P}/2\mu + \mathbf{p}\cdot\mathbf{p}/2m + V(\mathbf{R},\mathbf{r}) \quad \text{(B1)}$$

where $\mathbf{R}$ denotes the vector connecting atom X to the center of mass of diatom BC, $\mathbf{r}$ is the vector connecting B to C, and $\mathbf{P}$ and $\mathbf{p}$ are the corresponding canonically conjugate momenta. The potential V actually depends only on the magnitudes of $\mathbf{R}$ and $\mathbf{r}$, R and r, and the angle γ between these vectors.

One now imagines a canonical transformation from $(\mathbf{R},\mathbf{r},\mathbf{P},\mathbf{p})$ to $(R,r,q_l,q_j,q_J,P,p,l,j,J)$, where the new momenta explicitly include the magnitudes of orbital ($l = |\mathbf{R} \times \mathbf{P}|$), diatomic rotational ($j = |\mathbf{r} \times \mathbf{p}|$), and total ($J = |\mathbf{R} \times \mathbf{P} + \mathbf{r} \times \mathbf{p}|$) angular momenta. It is easy to see from the transformation relations between old and new coordinates of ref 32 that for $J = 0$ (choosing $q_J = 0$ and setting $\lambda_1 = \lambda_2 = 0$) the classical Hamiltonian then has the form

$$H = \frac{P^2}{2\mu} + \frac{p^2}{2m} + \frac{1}{2}\left(\frac{l^2}{\mu R^2} + \frac{j^2}{mr^2}\right) + V(R,r,\gamma) \quad \text{(B2)}$$

It can also be seen (eq 7 of ref 32) that γ is related to the canonical coordinates through

$$\cos\gamma = -\cos(q_l + q_j) \quad \text{(B3)}$$

when $J = 0$.

We now introduce a new set of canonical coordinates

$$q_+ = q_l + q_j \quad \text{(B4)}$$

$$q_- = q_l - q_j$$

and perform a standard canonical transformation[20] to obtain

$$H = \frac{P^2}{2\mu} + \frac{p^2}{2m} + \frac{1}{2}\left[\frac{(j_+ + j_-)^2}{\mu R^2} + \frac{(j_+ - j_-)^2}{mr^2}\right] + V \quad \text{(B5)}$$

---

[29] (a) Miller, W. H.; Handy, N. C.; Adams, J. E. *J. Chem. Phys.* 1980, *72*, 99. (b) For a review, see: Miller, W. H. *J. Phys. Chem.* 1983, *87*, 3811.

[30] E.g.: Miller, W. H. *Acc. Chem. Res.* 1976, *9*, 306 and references therein.

[31] E.g.: Rankin, C. C.; Miller, W. H. *J. Chem. Phys.* 1971, *55*, 3150.

[32] Miller, W. H. *J. Chem. Phys.* 1971, *54*, 5386.

where the new canonical (angular) momenta are

$$j_+ = (l + j)/2 \qquad \text{(B6)}$$
$$j_- = (l - j)/2$$

But since H does not depend on q_-, j_- is a constant of the motion. Furthermore, since $J = 0$, we have $l = j$ and thus $j_- = 0$ and $j_+ = l = j$. If we further realize that eq A3 implies that $\gamma = q_+ + \pi$, and that π is an arbitrary phase factor, we may take as canonical momenta and coordinates (P,p,j,R,r,γ) with Hamiltonian

$$H = \frac{P^2}{2\mu} + \frac{p^2}{2m} + \frac{j^2}{2}\left[\frac{1}{\mu R^2} + \frac{1}{mr^2}\right] + V(R,r,\gamma) \qquad \text{(B7)}$$

which is the required result.

Appendix C

Approximation of the Barrier Maximum and Separatrix Energy. In section IVB an effective potential in the R degree of freedom was defined as

$$V_{\text{eff}}(R;j,\gamma) = \frac{j^2}{2}\left(\frac{1}{\mu R^2} + \frac{1}{m\bar{r}_{\text{BC}}{}^2}\right) + V(R,\bar{r}_{\text{BC}},\gamma) \qquad \text{(C1)}$$

To obtain an idea of the nature of $V(R,\bar{r}_{\text{BC}},\gamma)$, we have scanned rays of fixed γ and determined the potential minimum position, R_γ, the well depth D_γ, and the Morse potential curvature factor given by

$$\alpha_\gamma = \left[\frac{1}{2D_\gamma}\frac{\partial^2 V}{\partial R^2}\right]^{1/2}_{R=R_\gamma} \qquad \text{(C2)}$$

where the second derivative is estimated with finite differences. The results of these calculations are shown in Table VI. From the data in Table VI it is evident that the collinear geometry, $\gamma = 0°$, is the least stable of all possibilities.

Two other functions of interest to us are the barrier maximum position, $R^1(j,\gamma)$, and the height (or separatrix energy) $\epsilon_s(j,\gamma)$. Consider a rectangular grid of j,γ values (j_i,γ_j). For each pair (j_i,γ_j) one may search along R to find the maximum of eq C1 and thus $R^1(j_i,\gamma_j)$ and $\epsilon_s(j_i,\gamma_j)$. Now the most accurate approach would involve fitting some smooth analytical function to these data. However, for our purposes we simply employ reasonably dense grids of $j_i = 0, 1, 2, ..., 17\hbar$ and $\gamma_j = 0, 10, ..., 90°$ and rely on two-dimensional linear interpolation to define our approximations to R^1 and ϵ_s, and their corresponding derivatives. Table VII gives a small portion of the grids used to give the reader an idea of how the functions behave.

In defining the above grids, it will be noticed that j extends up to only $17\hbar$. Actually, for a given value of γ there is a certain value of j, j_{complex}, above which the potential barrier and minimum have fused together to yield a purely repulsive effective potential. Such a repulsive potential is inconsistent with our notion of complexes, so that the region in phase space where complexes exist (to within our approximations) includes j values only up to j_{complex}. By explicit calculation we find j_{complex} ranges from $14.69\hbar$ at $\gamma = 90°$ to $17.46\hbar$ at $\gamma = 0°$ and is in fact well described by the linear relationship (γ in radians)

$$j_{\text{complex}} = 17.46 - 1.763\gamma \qquad \text{(C3)}$$

Finally, the maximum momentum along the $R < R^1$ branches of the separatrix, $P_s(j,\gamma)$, is also easily evaluated for the above (j,γ) grid. For fixed j and γ the minimum in the effective potential, $V_{\text{eff}}^{\text{min}}(j,\gamma)$, may be found by direct search along R. The separatrix maximum is given by

$$P_s(j,\gamma) = [2\mu(\epsilon_s(j,\gamma) - V_{\text{eff}}^{\text{min}}(j,\gamma))]^{1/2} \qquad \text{(C4)}$$

It turns out that P_s is largest for $\gamma = 90°$ and $j = 0$, and decreases both for increasing j and decreasing γ. We employ linear interpolation to define the numerical approximation required for P_s in section IVB.

Registry No. HeI_2, 64714-28-9.

Phase space bottlenecks and statistical theories of isomerization reactions

Stephen K. Gray[a] and Stuart A. Rice
The James Franck Institute and the Department of Chemistry, The University of Chicago, Chicago, Illinois 60637

(Received 11 August 1986; accepted 13 November 1986)

We examine the dynamics of isomerization reactions and point out the existence of important phase space bottlenecks. A three-state statistical theory based on the behavior of trajectories and the properties of the phase space bottlenecks is proposed; this theory is better than standard two-state RRKM theory under some circumstances and offers a new way of conceptualizing isomerization. We test our ideas on the simple system, consisting of an equivalent double well coupled to a Morse oscillator, which was studied by DeLeon and Berne. Approximate methods of obtaining the required elementary rate constants in our theory are also discussed.

I. INTRODUCTION

In this paper we show that a physically appealing model of isomerization dynamics can be constructed using recently developed ideas concerning bottlenecks to the flow of energy and chemical reaction in phase space.[1-3] The model naturally leads to the definition of three phase space domains (generalized system states) corresponding to the two isomer geometries and an intermediate which does not coincide with either isomer geometry. Exact and approximate methods for defining the generalized system states and associated rate constants are presented, and application is made to a two degree of freedom double well system previously introduced by DeLeon and Berne.[4]

Since the three-state model presented here differs from the standard RRKM theory model,[4-6] which involves just two states, the remainder of this Introduction briefly reviews the RRKM approach and then motivates the present contribution by reviewing some recent work which illuminates the dynamical nature of unimolecular reactions.

For a unimolecular isomerization reaction, RRKM theory assumes the existence of isolated molecule (microcanonical) rate constants $k_{AB}(E)$ and $k_{BA}(E)$ for the forward and reverse elementary reactions

$$\begin{aligned} &A \rightarrow B, \\ &B \rightarrow A. \end{aligned} \tag{1}$$

Unless $k_{BA}^{-1} \gg k_{AB}^{-1}$, or the converse, both reactions must be considered, as discussed by Chandler,[6] for example. This leads to the familiar relaxation kinetics expression

$$A(t) = A_e + [A(0) - A_e]\exp(-kt), \tag{2}$$

where

$$\begin{aligned} A_e &= Nk_{BA}/k, \\ k &= k_{AB} + k_{BA}, \end{aligned} \tag{3}$$

and where the fact $A(t) + B(t) = \text{const} = N$ for a closed system has been used. Thus, a given initial displacement of the A concentration from equilibrium, $A(0) - A_e$, relaxes to A_e with rate constant k.

The RRKM analysis of the unimolecular reaction rate is completed by noting the classical phase space formula for k_{AB}, namely

$$k_{AB}(E) = \frac{F^\ddagger_{AB}}{N^\ddagger_A(E)}, \tag{4}$$

where $F^\ddagger_{AB}$ is the forward flux of phase points across some surface dividing phase space into regions associated with molecular species A and B, and $N^\ddagger_A$ is a measure of the concentration of phase points within the A part of phase space. There are two conditions which must be satisfied for Eq. (4) to be applicable to a given reaction. First, either a specific molecular excitation of total energy E must relax on a time scale short relative to the time scale for chemical reaction so that the entire phase space consistent with reactant A at total energy E is filled, or the rate constant of interest is an average[7] of all possible rate constants within some energy range about E. Second, once a classical phase point crosses the dividing surface in the direction of products it either never recrosses the dividing surface (fragmentation reaction) or it does not recross for a time which is much longer than the typical vibrational period of either the A or B isomers (isomerization reaction). This second condition is the famous "point of no return" requirement of transition state theories[8] such as RRKM theory. Notice that there is no absolute point of no return for isomerization unless one has an extreme difference in the time scales k_{AB}^{-1} and k_{BA}^{-1}. The dividing surface is almost always taken to be defined by the condition that some reaction coordinate y be at its critical or transition state value, $y^\ddagger$, which leads to the explicit expressions for the flux

$$F^\ddagger_{AB} = \int d\mathbf{p}\, d\mathbf{x}\, \delta(E-H)\delta(y-y^\ddagger)\frac{p_y}{\mu}\theta(p_y) \tag{5}$$

and the effective concentration

$$N^\ddagger_A(E) = \int d\mathbf{p}\, d\mathbf{x}\, \delta(E-H)\theta(y^\ddagger - y), \tag{6}$$

where the integrals are over all the molecular phase space, y is a particular reaction coordinate, p_y is the momentum conjugate to y, μ is the mass associated with the y degree of freedom, and θ is the Heaviside step function which has the

---

[a] Present address: Department of Chemistry, Northern Illinois University, DeKalb, Illinois 60115.

0021-9606/87/042020-16$02.10

properties $\theta(x>0) = 1, \theta(x<0) = 0$. An analogous expression exists for k_{BA}. Equations (4)–(6) reduce to the more familiar Marcus–Rice rate constant expression,[5] involving a sum of states at the transition state and a reactant density of states, when the numerator and denominator of Eq. (4) are divided by factors of Planck's constant h and semiclassical arguments are used to define the sums and densities of states.[3]

There is a substantial body of literature concerned with those dynamical features of unimolecular reactions that are inconsistent with the above, simple, form for RRKM theory. Significant regions of trapped quasiperiodic motion[4,9] have been noted, for example. Hase and co-workers[10,11] introduced a kinetic scheme involving transitions among undefined intramolecular intermediates to phenomenologically model their classical trajectory results for C_2H fragmentation. Interestingly, recent experiments by Borchardt and Bauer[12] are consistent with a different, but related, intramolecular mechanism. Clearly, both of these studies hint at the existence of important phase space bottlenecks to reaction.

The intramolecular intermediates noted above may be thought of as different regions of the molecular phase space, with a bottleneck separating them. Very recently Davis[1] exploited some important developments in nonlinear dynamics[13,14] to define precisely the intramolecular bottlenecks in a collinear model of vibrational energy redistribution in OCS. Often, as in Davis' work, an intramolecular intermediate can be associated with the temporary trapping of phase points by partially destroyed resonance zones[15] and/or the remnants of particularly resilient tori (which support quasiperiodic motion). Davis[1] was also able to calculate *a priori* the corresponding intramolecular vibrational redistribution rate constants, which is an advance over purely phenomenological approaches.

Gray, Rice, and Noid[16] studied the phase space dynamics of a T-shaped model for HeI_2 fragmentation and saw a variety of nonlinear behavior including strong evidence for the existence of intramolecular bottlenecks. Subsequently, Davis and Gray[2] explicitly calculated some of the intramolecular bottlenecks of this model system but, more importantly for this paper, discovered a new type of barrier to the flow of phase points, termed an intermolecular bottleneck. Whereas intramolecular bottlenecks are associated with energy transfer within a single chemically identifiable species, intermolecular bottlenecks are associated with the energy transfer required for the formation of different chemical species. In the case of fragmentation, Davis and Gray[2] showed that the exact intermolecular bottleneck had the no-return property[8] of a transition state. The calculation of the location of the exact intermolecular bottleneck requires dynamical propagation of trajectories; it cannot at present be obtained exactly for systems with three or more degrees of freedom. However, as noted by Davis and Gray,[2] the intermolecular bottleneck, in the limit of small dynamical coupling, becomes a simple phase space separatrix.[15] In particular, Fig. 21 of Ref. 2 anticipates the isomerization separatrix structure we will see in this paper. Gray, Rice, and Davis[3] were then able to construct a purely statistical theory for fragmentation. This theory[3] is identical to RRKM theory except that the transition state condition is no longer a simple specification of a critical configurations,[5] but is a condition involving the reaction coordinate and momentum inferred from the separatrix approximation to the intermolecular bottleneck. The theory is particularly useful for weakly bound systems, such as van der Waals complexes, where ordinary RRKM theory fails. Additional aspects of this theory have been discussed by Gray and Rice.[17]

The existence of permanently trapped quasiperiodic motion, and temporary trapping associated with classical nonlinear resonances and the remnants of tori, are generic features of Hamiltonian dynamics.[15] DeLeon and Berne,[4] in an excellent and thorough study of the phase space dynamics of a two degree of freedom isomerization model, have noted such phenomena. Their work preceded the recent developments concerning the influence and nature of intra/intermolecular phase space bottlenecks and one goal of this paper is to reinterpret some of their results within the new framework. We will show, for example, that although the standard RRKM theory tends to break down when the total energy becomes significantly greater than the barrier to isomerization, a result usually attributed to a widening of the bottleneck,[4] certain intermolecular phase space bottlenecks can still be defined and a simple rate mechanism coupled with statistical assumptions can account for much of the observed behavior.

Section II below presents surface of section plots, as well as standard RRKM theory results, and discusses the phase space structure of the two well DeLeon–Berne model for several energies.[4] Most of our results are new; we look at higher energies than did DeLeon and Berne and we also offer some remarks on the influence of resonances on the isomerization rate. Section III rationalizes some of the results of Sec. II in terms of phase space bottleneck ideas and introduces a simple kinetic scheme for describing some features of the isomerization dynamics. Section IV discusses simple methods for obtaining the elementary rate constants required in Sec. III. Section V concludes by discussing possible extensions, as well as complications, of the methods presented in this paper.

II. THE DELEON–BERNE ISOMERIZATION MODEL

The DeLeon–Berne model[4] model consists of an equivalent double well potential, V_y, coupled to a Morse oscillator potential, V_x. Rather than follow the original formulation, which expressed the Hamiltonian in terms of velocities and coordinates and numerically integrated Lagrange's equations of motion to generate trajectories, we prefer to define canonically conjugate[15] momentum-coordinate pairs (p_y, y) and (p_x, x). The corresponding Hamiltonian is

$$H = \frac{p_y^2}{2\mu} + \frac{p_x^2}{2m} + V_y + V_x + W(y,x), \tag{7}$$

where the potentials are

$$V_y = 4y^2(y^2 - 1) + \epsilon_s, \tag{8a}$$

$$V_x = D_x[1 - \exp(-\lambda x)]^2, \tag{8b}$$

and

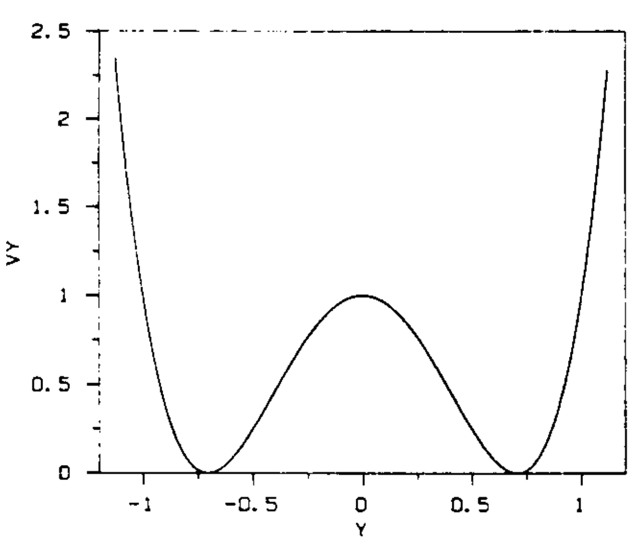

FIG. 1. Double well potential, Eq. (8a).

$$W = 4y^2[y^2 - 1][1 - \exp(-z\lambda x)]. \qquad (8c)$$

Our Hamiltonian is the same as that of DeLeon and Berne[4] when $\mu = m = 8$, $D_x = 10$, and $\epsilon_s = 1$. The potential defined by Eq. (8a) is displayed in Fig. 1. It will be noted that an energy $E = H > 1$ (measured in units of the barrier height) is required for isomerization to be classically allowed. Since we are uninterested in energies $E > 10$ for which dissociation of the Morse oscillator is allowed, we will concentrate attention on energies in the range $1 < E < 10$. Hamilton's equations of motion,

$$\dot{p}_y = \frac{-\partial H}{\partial y}, \quad \dot{y} = \frac{\partial H}{\partial p_y},$$
$$\dot{p}_x = \frac{-\partial H}{\partial x}, \quad \dot{x} = \frac{\partial H}{\partial p_x}, \qquad (9)$$

are then solved numerically for various fixed energies and a variety of initial conditions to generate classical trajectories $[p_y(t), p_x(t), y(t), x(t)]$. Composite surfaces of section are constructed by plotting $[y(t), p_y(t)]$ each time $x(t)$ passes through 0 and $p_x > 0$ for a variety of trajectories. Note that if $[p_y(t), p_x(t), y(t), x(t)]$ is a trajectory, then Eq. (9) coupled with the potentials in Eq. (8) imply that $[-p_y(t), p_x(t), -y(t), x(t)]$ is also a trajectory, hence the surface of section has inversion symmetry.

DeLeon and Berne studied many different systems defined by specifying different potential coupling parameters z and λ. We choose to study in detail one particular system, $z = 1$, $\lambda = 1.5$, as a function of energy. Figures 2(a)–2(e) show composite surface of section plots for energies $E = 1.02$, 1.25, 2, 3, and 6, respectively. Since we will be discussing the rate constants at all these energies it is essential to have these surfaces of section for reference. DeLeon and Berne studied the present potential coupling system for only one (the lowest) energy so that most of the results presented here are new.

Figure 2(a), corresponding to $E = 1.02$, an energy just 2% above the isomerization barrier $y^{\ddagger} = 0$, shows very noticeable regions of permanently trapped quasiperiodic motion on either side of the barrier. Consider, for example, the $y < 0$ side of the barrier. Because of the inversion symmetry noted for this system, similar remarks will hold for $y > 0$. Quasiperiodic trajectories fill out the islands of closed curves. Trajectories started on any of the central set of closed curves centered at about $y \approx -0.7$, $p_y \approx 0$, forever evolve on the corresponding closed curve. On the other hand, trajectories started on either the upper or lower set of closed curves repeatedly hop from top to bottom island structure, eventually filling out two closed curves. This behavior is consistent with the existence of a 2:1 resonance condition[13] between the two frequencies of oscillation,

$$2\omega_y \approx \omega_x, \qquad (10)$$

in the relevant portions of phase space. Actually, by setting $W = 0$ in Eq. (7), which defines a zero-order Hamiltonian, it is possible, via determination of the zero-order vibrational periods which depend on the amount of energy in each oscillator, to predict the importance of the 2:1 resonance in this case. Note that the 2:1 resonance traps trajectories on one or the other side of the barrier. Furthermore, the trajectories starting near one of the 2:1 island structures may lie in the stochastic layer associated with the destruction of the separatrix[15] between the two island structures. The existence of such a stochastic layer, as found, for example, in the studies of T-shaped HeI_2 fragmentation,[16] can also hinder reaction if there are significant bottlenecks between this layer and the remaining parts of phase space. Thus the mere fact that a 2:1 resonance condition exists is not at all sufficient to guarantee resonance enhancement of an isomerization reaction, as some work might imply.[18] Quite the contrary, a resonance can also hinder isomerization and one can only be certain of the true role of resonances by inspection of actual classical trajectories and, whenever possible, surfaces of section. The chaotic splotch of points in Fig. 2(a) is due to a single trajectory wandering throughout the phase space where quasiperiodic motion does not exist; such trajectories are responsible for meaningful classical isomerization. Finally, we note that at this energy ($E = 1.02$) there is only a small configuration space bottleneck at $y = 0$. The configuration space bottleneck should not be confused with the phase space bottlenecks which are the primary focus of this paper. By configuration space bottleneck we mean the surface defined by the condition $y = 0$. On the surface of section this bottleneck will be a straight line defined by $y = 0$ and all momenta p_y up to the energy conservation limit. Since chaotic trajectories can take a long time to pass through such a small configuration space bottleneck, and there can be severe trapping by the 2:1 stochastic layer, one observes relatively long trapping times at this energy and, therefore, a rate constant consistent with Eqs. (1) and (2) exists.

Consider, now, the results for $E = 1.25$ plotted in Fig. 2(b). It will be noted that the proportion of quasiperiodic motion has decreased (**Table I**, discussed later in this section, quantifies such observations). The standard RRKM theory configuration space bottleneck has also considerably widened. Although reduction of the amount of quasiperiodic motion can imply an increase in the rate of energy exchange, which is in agreement with one of the assumptions of RRKM theory, the widening of the configuration space

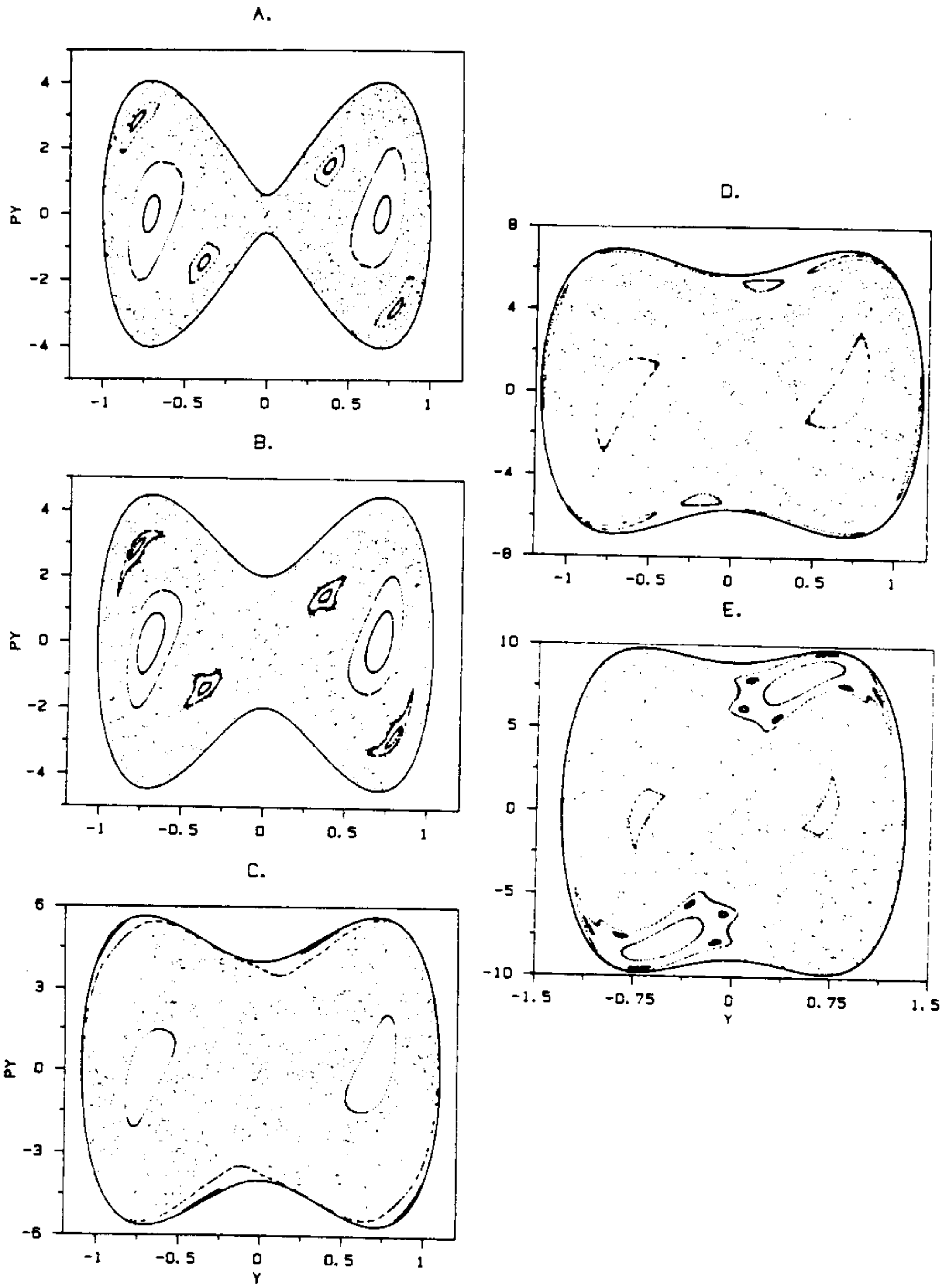

FIG. 2. Surfaces of section for the DeLeon–Berne system with $z = 1$ and $\lambda = 1.5$. (a) $E = 1.02$, (b) $E = 1.25$, (c) $E = 2$, (d) $E = 3$, and (e) $E = 6$.

bottleneck leads to more trajectories recrossing the transition state on a time scale comparable to or even smaller than the vibrational periods of the isomers. This violation of the no return concept leads one to question the existence of a rate scheme such as suggested by Eqs. (1) and (2). DeLeon and Berne,[4] in fact, noted that the time-dependent reactive flux function defined by Chandler[6] starts to exhibit increasingly severe oscillations as E is increased above the barrier; such oscillations are symptomatic of a breakdown of the rate scheme of Eqs. (1) and (2). Figures 2(c) and 2(d) show a continuation of the trends observed between Figs. 2(a) and 2(b). For this range of increase in energy the proportion of quasiperiodic motion decreases while the configuration space bottleneck increases in size. Figure 2(e), corresponding to $E = 6$, shows an interesting break in the trend of decreasing quasiperiodic motion. Significant islands of quasiperiodic motion have actually grown in; these correspond to another 2:1 resonance consistent with Eq. (10). The 2:1 resonance at the low energy is due to coupling between a y vibration in one of the wells (zero-order motion below the barrier) and an x degree of freedom vibration. The new 2:1 resonance in Fig. 2(e) is due to coupling between a circulating y degree of freedom motion (zero-order motion above the barrier) and an x degree of freedom vibration, which implies that trajectories perpetually hop from the upper right-hand side island structure to the lower left-hand side island structure. Note that such resonant motion also occurs near the edges of energy contour at $E = 2$ and 3 in Figs. 2(c) and 2(d), but to a much lesser extent than at $E = 6$. In one sense this resonance leads to enhancement of the isomerization rate on a time scale comparable to or less than the period of the resonance. However, unless there is some means of stabilizing trajectories that reach the product side (e.g., removal of energy via additional degrees of freedom or solvent interactions) then for a time scale greater than the 2:1 resonance period the effect of the resonance on the rate constant cancels out.

To further discuss the validity of the simple RRKM analysis of isomerization reaction dynamics, we will examine the temporal behavior of the fraction of A systems,

$$\begin{aligned} A^{\ddagger}(t) &= \int dx\, dp_x\, dy\, dp_y \rho(x,p_x,y,p_y)\theta(y^{\ddagger} - y_t) \\ &\equiv \langle \theta(y^{\ddagger} - y_t \rangle_{\rho}. \end{aligned} \tag{11}$$

The symbol ‡ on A is to remind the reader that the standard RRKM theory definition of isomer A has been employed, namely that a phase point counts as an A point at time t if the reaction coordinate $y_t < y^{\ddagger}$. ρ is any appropriate normalized distribution. The integral in Eq. (11) is over all initial conditions $[x,p_x,y,p_y]$. Equation (11) is easily related to the Chandler reactive flux function[6] employed by DeLeon and Berne.[4] Choose an initial distribution such that all initial points are in A:

$$\rho(x,p_x,y,p_y) = \rho_A(x,p_x,y,p_y)\theta(y^{\ddagger} - y). \tag{12}$$

It is then easy to see that $A^{\ddagger}(t)$ is a time correlation function with respect to the ensemble ρ_A:

$$A^{\ddagger}(t) = \langle \theta(y^{\ddagger} - y)\theta(y^{\ddagger} - y_t)\rangle_{\rho_A}.$$

Microscopic reversibility implies that

$$\begin{aligned} -\frac{dA^{\ddagger}}{dt} &= -\langle \theta(y^{\ddagger} - y)\dot{\theta}(y^{\ddagger} - y_t)\rangle_{\rho_A} \\ &= \langle \theta(y^{\ddagger} - y)\dot{\theta}(y^{\ddagger} - y_{-t})\rangle_{\rho_A} \\ &= \langle \theta(y^{\ddagger} - y_t)\dot{\theta}(y^{\ddagger} - y)\rangle_{\rho_A}. \end{aligned} \tag{13}$$

When written as a phase space average, Eq. (16) assumes the form

$$-\frac{dA^{\ddagger}(t)}{dt} = \int dx\, dp_x\, dy\, dp_y\, \rho_A \theta(y^{\ddagger} - y_t)\frac{p_y}{\mu}\delta(y^{\ddagger} - y), \tag{14}$$

which is essentially the reactive flux function of Chandler.

Figures 3(a)–3(e) display $A^{\ddagger}(t)$ for energies consistent with Fig. 2. In all cases, for simplicity, the initial ensembles were random samplings on the A-half of the surface of section. Thus, $N = 1000$ points (y_k,p_{yk}) were selected randomly on the $y < y^{\ddagger} = 0$ portion of the (y,p_y) plane, and for each such point we set $x_k = 0$, with $p_{xk} > 0$ chosen by energy conservation. Equation (14) becomes

$$A^{\ddagger}(t) \cong N^{-1}\sum_k \theta(y^{\ddagger} - y_{kt}).$$

Figure 3(a) shows $A^{\ddagger}(t)$ for $E = 1.02$. The solid, somewhat jagged, curve is the result of numerically integrating 1000 trajectories with initial conditions defined as described above. At first glance there appears to be a glaring deviation from the standard RRKM theory prediction, Eq. (4). If one assumes any (energy allowed) point in phase space is on a trajectory which can lead to isomerization, then the expected equilibrium fraction $A_e = 1/2$ if the initial sample is characterized by $A(0) = 1$. However, Fig. 3(a) shows that the A population tends to a value much greater than 1/2. In fact, this is a trivial consequence of there being certain quasiperiodic trajectories in the A part of phase space that cannot lead to isomerization. RRKM theory, following DeLeon and Berne,[4] is easily modified to take account of these quasiperiodic trajectories. The dashed curve in Fig. 3(a) is the function

$$A^{\ddagger\mathrm{RRKM}}(t) = \tfrac{1}{2}(1 + f^{\ddagger}_{\mathrm{QP}}) + \tfrac{1}{2}(1 - f^{\ddagger}_{\mathrm{QP}})\exp(-k't), \tag{15}$$

where $f^{\ddagger}_{\mathrm{QP}}$ is the fraction of quasiperiodic trajectories trapped on one side or the other of $y = y^{\ddagger}$ on the surface of section and k' is a modified RRKM rate constant. The modification to the rate constant, introduced by DeLeon and Berne,[4] accounts for the fact that if quasiperiodic motion exists in the phase space it must be subtracted out of the RRKM theory formulas. Equation (15) is just an extension of Eq. (2), where a constant term for the trapped quasiperiodic fraction, $f^{\ddagger}_{\mathrm{QP}}$, has been added and $A(0)$ and A_e have been replaced by values appropriate to the stochastic part of the A phase space, $1 - f^{\ddagger}_{\mathrm{QP}}$ and $\tfrac{1}{2}(1 - f^{\ddagger}_{\mathrm{QP}})$, respectively. The rate constant k' in Eq. (15) is given by

$$\begin{aligned} k' &= \frac{k}{(1 - f^{\ddagger}_{\mathrm{QP}})} \\ &= \frac{2k_{AB}}{(1 - f^{\ddagger}_{\mathrm{QP}})} \\ &= \frac{2F^{\ddagger}_{AB}}{(1 - f^{\ddagger}_{\mathrm{QP}})N^{\ddagger}_{A}}, \end{aligned} \tag{16}$$

where $k, k_{AB}, F^{\ddagger}_{AB}$, and $N^{\ddagger}_{A}$ are given by Eqs. (3)–(6) and the fact that $k_{AB} = k_{BA}$ for an equivalent double well potential has been used. Equation (16) can be further simplified, using the standard rules of delta function integration,[3] to read

$$k' = \frac{4\int dx\{2m[E - V(x,y = y^{\ddagger})]\}^{1/2}}{(1 - f_{\mathrm{QP}})\int dx\, dy\, dp_x\{2m/[E - p_y^2/2\mu - V(x,y)]\}^{1/2}}. \tag{17}$$

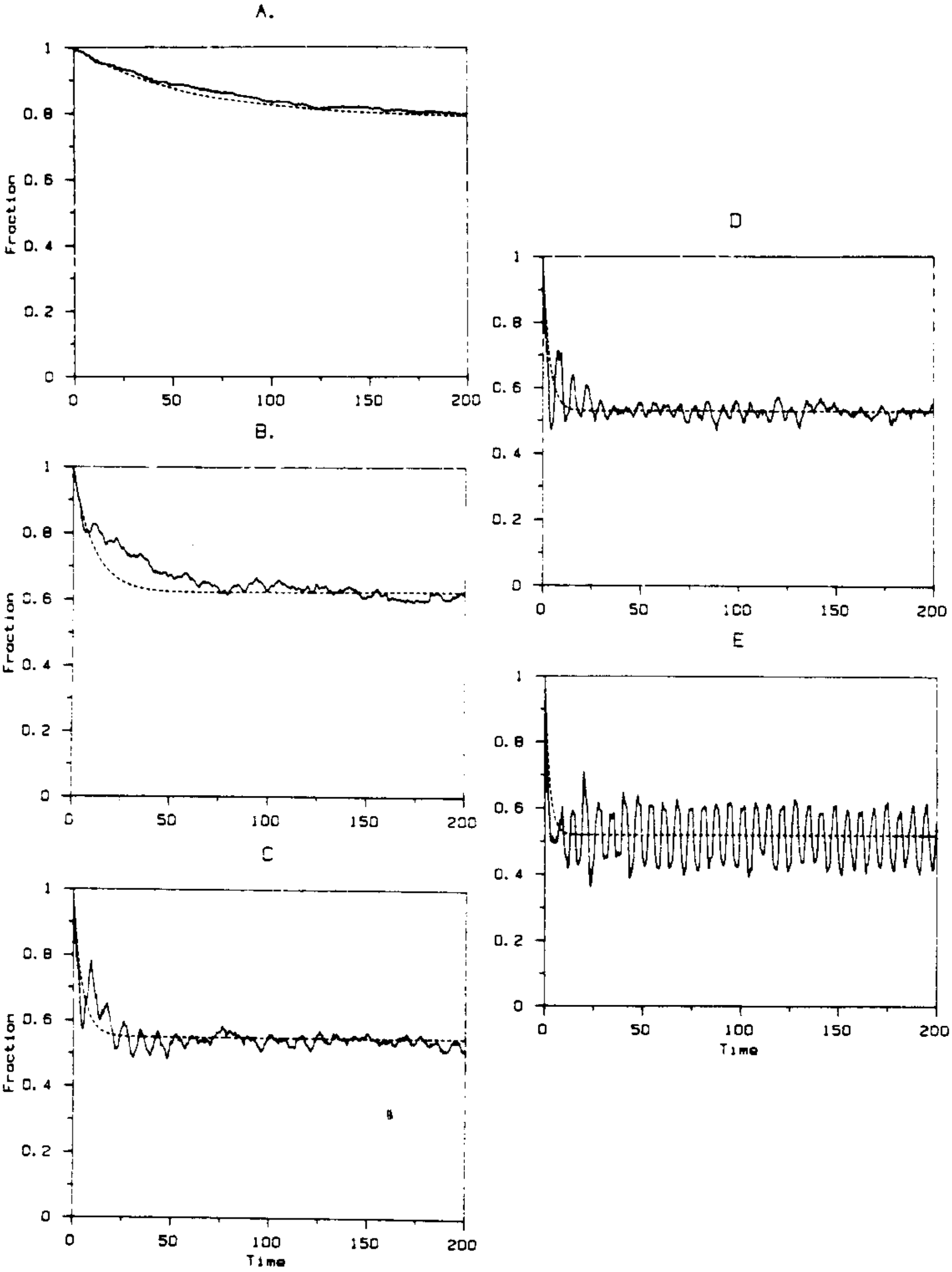

FIG. 3. Fraction of A systems, Eq. (14), defined in the standard RRKM manner. Solid lines are the result of propagating 1000 trajectories in time and the dashed curves are the RRKM predictions suitably modified for the presence of quasiperiodic motion. (a) $E = 1.02$, (b) $E = 1.25$, (c) $E = 2$, (d) $E = 3$, and (e) $E = 6$.

Table I lists the fraction of quasiperiodic trajectories trapped on one side of the surface of section, the standard RRKM theory rate constant k, and the quasiperiodic motion corrected rate constant k' for the energies of interest. Table I also lists the total fraction of quasiperiodic motion, including such motion as the 2:1 resonance at $E = 6$ discussed in Sec. II, which is not trapped on one side or the other of $y = y^{\ddagger}$. As is evident from Fig. 3(a), Eq. (15) is indeed a reasonable description of the behavior of the double well system when $E = 1.02$. DeLeon and Berne[4] also examined this particular system and energy and, on the basis of a trajectory approximation to the reactive flux function, also observed approximate exponential decay. However, the rate constant inferred from the reactive flux was about a factor of

TABLE I. RRKM theory data for DeLeon–Berne system with $z = 1$, $\lambda = 1.5$.

E	f^{t}_{QP} [a]	f^{tot}_{QP} [a]	k [b]	k [c]
1.02	0.57	0.57	0.0075	0.017
1.25	0.24	0.24	0.073	0.096
2.00	0.099	0.156	0.196	0.217
3.00	0.058	0.169	0.280	0.297
6.00	0.038	0.269	0.405	0.421

[a] f^{t}_{QP} is an estimate of the fraction of quasiperiodic motion trapped on one side or the other of the surface of section. f^{tot}_{QP} is the total fraction of quasiperiodic motion, including quasiperiodic trajectories that are not trapped on one side.

[b] Standard RRKM theory relaxation rates.

[c] Quasiperiodic corrected RRKM theory relaxation rates, Eq. (20).

2 lower than from RRKM theory, which is worse agreement than our Fig. 2(a) would suggest. There are several possible sources for this discrepancy. First, judging from the 25% error bars on DeLeon and Berne's rate constant, their analysis may simply have been a little more approximate than ours. Second, the DeLeon and Berne rate constant was probably inferred from a fit to the long time ($t > 200$) reactive flux so that some long time correlations may be more evident in their result. Indeed, we expect that at such low energies intramolecular bottlenecks[1,2] can lead to lower rate constants. Nonetheless, we find here that RRKM theory, suitably modified for the existence of some quasiperiodic motion, and without adjustable parameters, describes accurately the entire $0 < t < 200$ behavior of the reactant population.

Figure 3(b), corresponding to $E = 1.25$, shows more serious discrepancies between the quasiperiodic fraction corrected RRKM theory and the trajectory results [note the vertical axis scale is different from that in Fig. 3(a)]. In particular, only the short and long time limits seem adequately described by Eq. (15). The agreement in these two limits is not surprising. In the short time limit there are no trajectory recrossings of the dividing surface, so one expects Eq. (15) to be exact. One also expects the trajectory results to oscillate about the long time limit of Eq. (15), and the degree of oscillation is a measure of the adequacy of the assumed rate mechanism. The main point, however, is that the simple RRKM-type expression, Eq. (15), is not a very good description of the trajectory results when the energy is increased to a value 25% above the classical barrier. Figure 3(c), corresponding to $E = 2$, shows oscillations that are particularly severe for intermediate values of the time. Figures 3(d) and 3(e), corresponding to $E = 3$ and 6, respectively, show increasingly dominant oscillations for all time. The $E = 6$ result is particularly striking in that even in the very long time limit very large oscillations occur, implying that simple RRKM theory, even modified to account for the trapped quasiperiodic trajectories, cannot easily account for the observed behavior. Actually, the large amplitude long time oscillations when $E = 6$ are due to a large portion of the initial sample lying in the 2:1 resonance zone discussed above in relation to Fig. 2(e). One expects, in general, that an equation such as Eq. (15) would at best only describe the average of the oscillations.

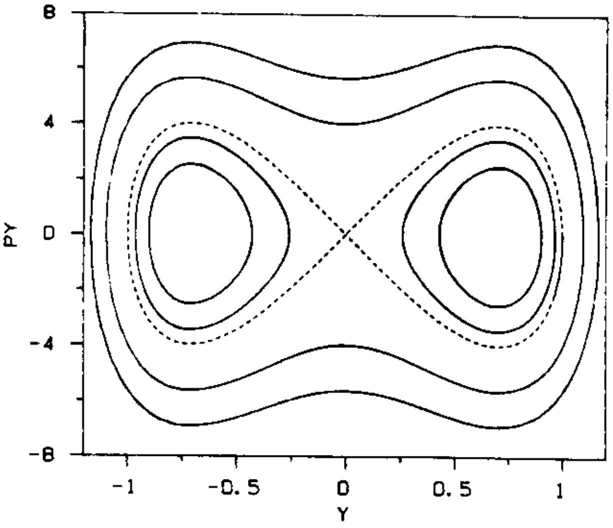

FIG. 4. Phase plane trajectories for the zero-order Hamiltonian, Eq. (21). The dashed curve is the separatrix.

III. AN ALTERNATIVE STATISTICAL THEORY FOR UNIMOLECULAR ISOMERIZATION

In Sec. II we showed that the standard form for RRKM theory, even when the presence of trapped quasiperiodic motion is accounted for, does not adequately describe the DeLeon–Berne isomerization model as energy is increased significantly above the classical barrier height. Section III A below motivates an alternative description of isomerization dynamics in phase space that involves three, as opposed to two, different regions. Section III B outlines more technical details associated with the actual division of phase space and Sec. III C presents numerical results that verify these ideas for the DeLeon–Berne model.

A. A three-state isomerization reaction picture

Figure 4 displays phase space trajectories for the Hamiltonian

$$h_y = \frac{p_y^2}{2\mu} + V_y, \tag{18}$$

where V_y is the double well potential of Eq. (8a) and $\mu = 8$ as before. Notice that there are three types of trajectories: A-type trajectories are bound vibrations to the left of the barrier at $y = y^{\ddagger} = 0$ and are indicated by closed concentric curves centered on $y = -2^{-1/2}$; B-type trajectories are vibrations on the right-hand side of the barrier centered on $y = 2^{-1/2}$; and C-type trajectories, which forever circulate between the left and right parts of the phase plane and envelope the A and B families of trajectories. A separatrix S is drawn in as a dashed curve. The separatrix is a special phase space structure, emanating from the fixed point at $y = p_y = 0$, that rigorously separates the three different types of motion.

When classical mechanical motion is integrable, i.e., when F constants of the motion exist in a $2F$-dimensional phase space, meaningful isomerization does not exist. Note that all one-dimensional conservative Hamiltonian systems such as Eq. (18) are integrable. We do not consider C-type (circulating) trajectories to lead to meaningful isomerization because the species A and B do not have vibrational identities during the course of a C trajectory. Only through the introduction of a nonintegrable coupling, W, to another degree of freedom, as in Eq. (7), will one be able to have classical transitions between the different types of classical motion.

If one considers the two degree of freedom Hamiltonian of Eq. (7) and sets $W = 0$, the surfaces of section as defined in the previous section will all look exactly like Fig. 4. If one introduces a nonzero, nonintegrable, perturbation W, one still expects some of the structure of Fig. 4 to remain. The perturbation W has the effect of creating the classical equivalent of superposition states: some trajectories will appear to display, as time goes on, features consistent with A-type trajectories, then C-type trajectories, then possibly B-type trajectories, and so on, in complicated sequences. In the language of Reinhardt and co-workers,[19] one is observing transitions from one type of vague torus to another. Quantum mechanically, of course, one can have superposition states without there being a nonintegrable coupling term. For example, one can imagine a one-dimensional problem with an A-type wave packet corresponding to mean energy below the classical barrier that subsequently tunnels to form a B-type wave packet. Such differences between classical and quantum mechanics are very important, but are not the subject of the present paper. Figure 5 illustrates an occupancy sequence for a typical trajectory of the full Hamiltonian, Eq. (7), when $E = 2$. In Fig. 5 we mark a 1 each time the trajectory is in the A part of phase space, a 2 if it is in the B part of phase space and a 3 if it is in the C part of phase space. The way we decide which region the trajectory is in at a given time t is to examine its (y,p_y) point and determine whether or not it lies within the appropriate separatrix branches. The explicit construction of the separatrix branches for the full problem is a little more difficult than for the zero-order problem discussed above and is outlined in detail in Sec. III B following. The average period of vibration in the other (x) degree of freedom is about three time units, so Fig. 5 shows that there can be very long sequences where the trajectory is inside the A, B, or C parts of phase space; this figure lends support to the notion that the trajectory undergoes transitions among A, B, and C types of motion.

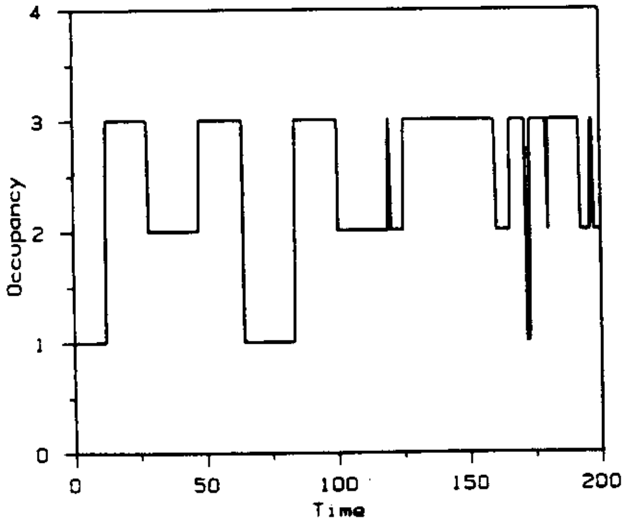

FIG. 5. Occupation sequence for an arbitrary trajectory of the full system. A 1 on the vertical axis implies the system is in A, a 2 implies B, and a 3 implies C. The trajectory displayed has $E = 2$.

Actually, it is worthwhile to emphasize that the most correct partitioning of the phase space, following, e.g., Davis and Gray,[2] involves introducing subdomains within the main A, B, and C regions corresponding to intramolecular bottlenecks and other dynamical features within these regions. For example, the trapping effects associated with either of the 2:1 resonance zones discussed in Sec. II can then be accounted for. The present notion of just three phase space regions is an idealization and simplification of the full description. The significance of this partitioning, in our opinion, is that it is the simplest and most natural description of the phase space because it is based on the phase space structure of a generic uncoupled Hamiltonian for a system which has two isomers.

The idea behind the alternative statistical approach is that, on average, the occupancy sequence of ensembles of trajectories can be better described by the three-state rate mechanism,

$$\dot{A} = -k_{AC}A + k_{CA}C, \tag{19a}$$

$$\dot{B} = -k_{BC}B + k_{CB}C, \tag{19b}$$

$$\dot{C} = k_{AC}A + k_{BC}B - (k_{CA} + k_{CB})C, \tag{19c}$$

than by the simpler two-state mechanism of Eq. (1) and (2). Dynamical and statistical methods for estimating the required elementary rate constants will be discussed in Secs. III C and IV.

Equations (19) admit analytical solution. The case of interest to us is that of a symmetric double well potential in which $k_{AC} = k_{BC}$ and $k_{CA} = k_{CB}$. If one assumes the normalisation $A + B + C = 1$, then the substitution $C = 1 - A - B$ allows Eqs. (19a) and (19b) to be easily solved by standard methods.[20] We readily find the particular solution corresponding to the initial condition $A(0) = 1, B(0) = C(0) = 0$ to be

$$\begin{aligned} A(t) &= (\tfrac{1}{2} - A_e)e^{-\lambda_1 t} + \tfrac{1}{2}e^{-\lambda_2 t} + A_e, \\ B(t) &= (\tfrac{1}{2} - B_e)e^{-\lambda_1 t} - \tfrac{1}{2}e^{-\lambda_2 t} + B_e, \\ C(t) &= 1 - A(t) - B(t), \end{aligned} \tag{20}$$

where

$$\begin{aligned} A_e &= B_e = k_{CA}/\lambda_1, \\ \lambda_1 &= k_{AC} + 2k_{CA}, \\ \lambda_2 &= k_{AC}. \end{aligned} \tag{21}$$

Other multistate reaction dynamics models have been proposed in the literature.[21,22] The difference here is that we will employ, in Secs. III C and IV, ideas and methods from nonlinear dynamics to define the corresponding states and elementary rate constants.

B. Generation of the separatrix and the elementary rate constants

In this paper we define the separatrix in two ways. In this subsection we discuss the "exact" separatrix, the computation of which requires the propagation of classical trajectories. Readers who wish to ignore these details may skip to the last three paragraphs of this subsection for a discussion of essential properties, or to Sec. IV where a more practical—but approximate—separatrix is defined.

The methods employed to generate the exact separatrix (or intermolecular bottleneck) that divides phase space into regions A, B, and C, and the relevant rate constants k_{AC}, etc., that occur in Eqs. (19), are similar to those employed by Davis and Gray[2] for a fragmentation problem. It should also be noted that the methods used by Davis and Gray were in turn based on earlier work by Channon and Lebowitz[23] for a particular nonlinear mapping problem. The case of isomerization is actually much closer to the problem studied by Channon and Lebowitz. We feel it useful, however, to give a careful discussion of the explicit method used since there are a number of technical features that are different than in the above cited references. Also, the properties of the isomerization separatrix are somewhat different from the fragmentation separatrix and deserve to be carefully outlined.

The dynamics in the reactive $y-p_y$ phase plane of the full phase space is determined by the surface of section mapping[15]

$$\begin{aligned} y_{k+1} &= T_y(y_k, p_{yk}), \\ p_{yk+1} &= T_{p_y}(y_k, p_{yk}). \end{aligned} \tag{22}$$

Given some point (y_k, p_{yk}) on a surface of section like one of those discussed in Sec. II, the next time the corresponding trajectory passes through the surface of section the point it hits will be (y_{k+1}, p_{yk+1}), determined by the smooth continuous mapping functions T_y and T_{p_y} in Eq. (22).

The construction of the full separatrix involves generating the global stable and unstable manifolds of a relevant fixed point of the mapping given by Eq. (22), and finding those that separate the two isomer regions. A fixed point (y^*, p_y^*) of the mapping is a periodic classical trajectory whose surface of section intersections satisfy

$$\begin{aligned} y^* &= T_y(y^*, p_y^*), \\ p_y^* &= T_{p_y}(y^*, p_y^*). \end{aligned} \tag{23}$$

The "relevant" fixed point must be unstable and its manifolds must be such that appropriate unions of portions of them generate the desired separatrix structure. For a general problem it is usually necessary to search, via Newton–Raphson or other such procedure, to find the fixed points.[1] Furthermore, the desired separatrix structure is one that encompasses most or all of the relevant intramolecular dynamics in the two isomer halves of phase space and some trial and error may be involved in finding the appropriate fixed point. However, with the DeLeon–Berne model the symmetry is such that $y^* = p_y^* = 0$ is always a fixed point and we have found empirically that it generates suitable separatrices.

Linearization of Eq. (22) about the fixed point of Eq. (23) yields

$$\Delta\Gamma_{k+1} = \mathbf{A}\Delta\Gamma_k, \tag{24a}$$

where

$$\Delta\Gamma_k = \begin{bmatrix} (y_k - y^*) \\ (p_{yk} - p_y^*) \end{bmatrix} \tag{24b}$$

and

$$\mathbf{A} = \begin{bmatrix} \left(\frac{\partial T_y}{\partial y}\right)_* & \left(\frac{\partial T_y}{\partial p_y}\right)_* \\ \left(\frac{\partial T_{py}}{\partial y}\right)_* & \left(\frac{\partial T_{py}}{\partial p_y}\right)_* \end{bmatrix}. \tag{24c}$$

The local dynamical behavior about the fixed point is determined by the eigenvalues and eigenvectors of $\mathbf{A}$.[15,24] Since the relevant fixed point is unstable, all the matrix elements are real. In practice the required derivatives in Eq. (24c) are determined numerically by propagating additional trajectories on the surface of section in the vicinity of (y^*, p_y^*) because, of course, T_y and T_{p_y} are not known analytically. Let Ψ_u and Ψ_s denote the two eigenvectors of A. Positive and negative multiples of these eigenvectors then determine four lines emanating from and forming an X at the fixed point. We take Ψ_u to be an eigenvector with positive components. One global manifold, which is termed the unstable global manifold, is formed using Ψ_u as follows. One takes a small step away from the fixed point along Ψ_u. This point is propagated once on the surface of section to determine another point near it and still essentially on Ψ_u because the original step away was small. A line of points is defined by connecting the initial step and its propagated point with a straight line and choosing a suitable number (in practice 100 or 200) of evenly spaced points along the line. Each such point is propagated in time on the surface of section. At the end of each propagation step a curve is drawn through the 100 or 200 propagated points by connecting the point that was originally the last point on the initial line (i.e., originally furthest from the fixed point) to the point that was originally next to last on the original line and so on. The result is a good approximation to the global unstable manifold: if one takes any point on this structure it will map to another point on it as time goes on. The manifold is called unstable because points on it move asymptotically towards the fixed point only when integrated backward in time. Figure 6(a) shows the resulting global unstable manifold after just a few propagation steps on the surface of section. Further iterations yield an ever more convoluted structure.[2,15,17]

A stable manifold may be formed from Ψ_s, whose components may be taken to be positive in the y direction and negative in the p_y direction. By definition, points on the stable manifold always approach the fixed point when integrated forward in time, the opposite situation compared to the unstable manifold, so it is necessary to integrate the equations of motion *backward* in time to generate it. This is easily accomplished by using a negative time step in the numerical integrator used. Following a procedure identical to that in the above paragraph, but with a negative time step in the integrator and Ψ_s instead of Ψ_u, one generates the stable manifold displayed in Fig. 6(b) as a dashed curve. In Fig. 6(b) we have also superimposed on the stable manifold the unstable manifold of Fig. 6(a). We noted earlier that there are four directions associated with a linear analysis about the fixed point, corresponding to positive and negative multiples of the eigenvectors Ψ_s and Ψ_u. Two other global stable and unstable manifolds, associated with $-\Psi_s$ and $-\Psi_u$ may easily be found by inverting the two manifolds in Fig. 6(b) about the fixed point origin.

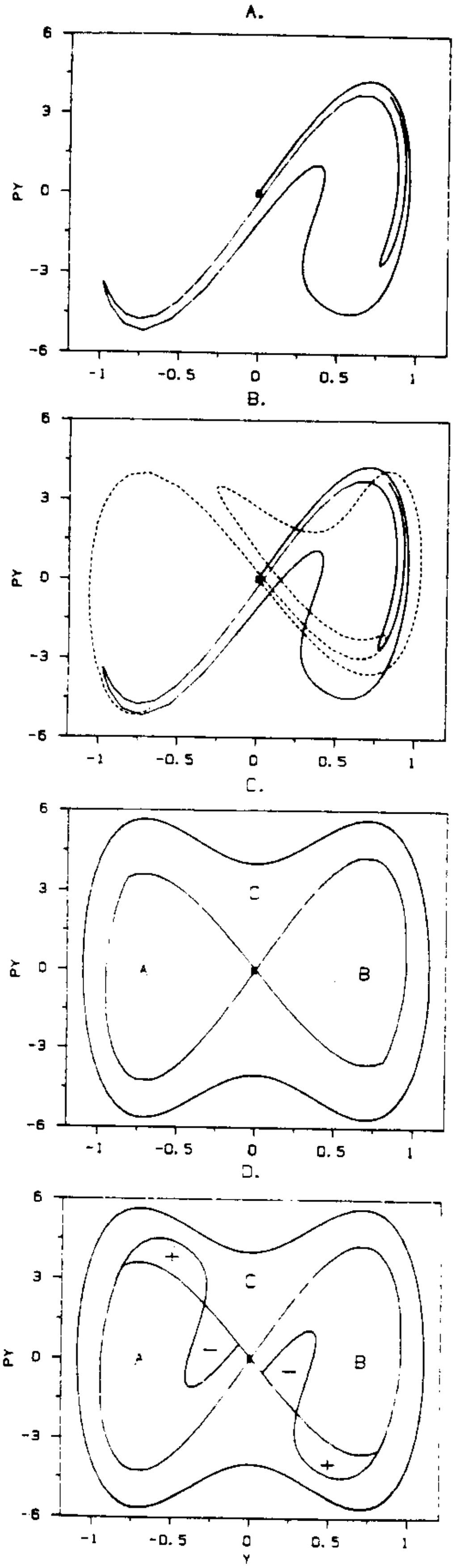

FIG. 6. Construction of exact separatrix on the surface of section for $E = 2$. (a) The unstable manifold, (b) superposition of the stable (dashed) and unstable (solid) manifolds, (c) the exact separatrix, which is a union of portions of the above manifolds. Note by inversion symmetry there is a related structure for $y = 0$. (d) Turnstiles superimposed on the separatrix.

The separatrix is obtained by taking a union of portions of the two manifolds shown in Fig. 6(b). One such union is shown in Fig. 6(c), along with its inverted partner. Close inspection of Fig. 6(c) shows cusps where the two manifold portions were united. The union we chose led to a separatrix that appears similar to the zero-order separatrix of Fig. 4. This is not necessary, as discussed in Ref. 2 in more detail. The separatrix in Fig. 6(c) has some very useful properties. If one imagines turning off the coupling W the separatrix structure of Fig. 6(c) becomes the zero-order separatrix. The separatrix as defined above has the property that phase points within its branches can only enter or exit it through certain localized regions called turnstiles.[13] For example, Fig. 6(d) shows the result of propagating the entire separatrix in Fig. 6(c) one step on the surface of section. Note that the superposition of Figs. 6(c) and 6(d) defines lobes. Phase space area is seen to leave the inside of the separatrix only through the small areas labeled +, and phase space area enters the separatrix only through the small areas labeled −. Each +/− pair in Fig. 6(d) is a turnstile.

There is another property of the separatrix for isomerization worth mentioning. Consider a phase point that maps out of one of the separatrix lobes. For the sake of argument let us imagine a point exits the B lobe (right-most lobe) through the + part of the turnstile on the lower right of Fig. 6(d). Notice it is necessarily in region C and cannot directly hop into A. Thus only after one or more time steps in region C might a phase point that exited region B either enter into region A (via the − part of the turnstile in the upper left) or return to region B. Unlike the fragmentation separatrix, there is no absolute point of no return here: a point leaving one region can always return to it later on.

The elementary rate constants required by Eq. (19) are easily found if the separatrix has been constructed. Let F_A^+ be the area of the outgoing + part of the turnstile for the A-separatrix lobe. This is the phase space area that leaves A per iteration on the surface of section. Thus the rate constant for A → C is

$$k_{AC} = \frac{F_A^+}{A'}\frac{\overline{\omega}}{2\pi}, \tag{25}$$

where A' is the area of the A separatrix lobe (with any quasiperiodic area subtracted out) and $2\pi/\overline{\omega}$ is the average time between successive surface of section iterations. In the present equivalent double well problem, $k_{BC} = k_{AC}$. Similarly, the rate constant for C → A transitions is

$$k_{CA} = \frac{F_A^-}{C'}\frac{\overline{\omega}}{2\pi}, \tag{26}$$

where C' is the area of region C less any quasiperiodic area in that region. Conservation of phase space area implies $F_A^- = F_A^+$, and for an equivalent double well potential $k_{CB} = k_{CA}$. All the relevant areas may be estimated from figures such as Fig. 6(d) by, e.g., graphical means or numerical integration. Table II lists the relevant quantities and elementary rate constants for the DeLeon–Berne model with $E = 1.25$, 2, 3, and 6.

A final comment is in order about the separatrix discussed in this section; it was constructed for the surface of

TABLE II. Elementary rate constants and related data.

E	$2\pi\sqrt{\omega}$	$f_{\rm QP}^A$	F_A^*	A'	C'	k_{AC}	k_{CA}
1.25	2.65	0.31	0.25	3.64	3.38	0.0259	0.0279
2.00	2.72	0.18	0.54	4.12	9.70	0.0481	0.0205
3.00	2.84	0.16	0.69	4.24	15.07	0.0572	0.0161
6.00	3.30	0.17	1.15	3.48	25.72	0.0999	0.0140

section mapping [Eq. (22)]. Such a surface of section corresponds to looking at the y and p_y values each time x and p_x pass through a particular phase of vibration. Usually one chooses the phase such that $x = 0$ and $p_x > 0$. Let this phase be denoted by $q_x = q_x^{\rm sos}$. In general one can construct a different surface of section for any fixed x value and sign choice for p_x which corresponds, say, to some phase value $0 < q_x < 2\pi$. Thus the surface of section is really parametrized by q_x. One could construct separatrices as a function of q_x and the most precise separatrix criterion is really some requirement

$$S(y,p_y,q_x) = 0. \tag{27}$$

Thus, given any arbitrary point (x,y,p_x,p_y), Eq. (27) should be used to determine whether or not the point is inside regions A, B, or C. It is probably clear that this involves a lot of work because at each energy one must then carry out the separatrix determination procedure outlined above for a series of q_x values in order to determine some approximation to $S(y,p_y,q_x)$. We do not carry out this procedure, but rather approximate

$$S(y,p_y,q_x) \simeq S(y,p_y,q_x = q_x^{\rm sos}). \tag{28}$$

There are three reasons why this approximation is reasonable. First, we have found it to always be the case that the fluxes in Table II are invariant to q_x. Thus k_{AC}, k_{BC}, etc., do not depend strongly on q_x and are properties that can be obtained from any portion, such as $q_x = q_x^{\rm sos}$, of the full separatrix structure. Second, while the exact shape of the separatrix is a function of q_x, we have found the separatrix to be qualitatively the same for most q_x values. Finally, if there is a reasonable time scale separation (x motion faster than y motion) the approximation [Eq. (28)] should lead to high frequency oscillations that are not relevant.

C. Application to the DeLeon–Berne model

The theory of Secs. III A and III B is now applied to the DeLeon–Berne system (with $z = 1$ and $\lambda = 1.5$ as before). To compare with the three-state model predictions we carry out trajectory calculations. For each energy we take an initial ensemble of 1000 points randomly distributed within the A lobe of the separatrix of Sec. III B and otherwise on the surface of section such that $x = 0$ and $p_x > 0$. Each such point is propagated in time, and trajectory based $A(t)$, $B(t)$, and $C(t)$ populations are obtained by determining, at a given time t, the fraction of trajectories within the three parts of phase space. For ease of calculation we have assumed the approximation [Eq. (28)], so that the above fractions are determined solely from the y and p_y variables, although in principle the x and p_x variables should also enter into the determination through their phase q_x.

The ensembles defined above will naturally contain a certain fraction $f_{\rm QP}^A$ of phase points lying on quasiperiodic islands within A; the three-state model is easily modified to allow for this behavior. One need only replace Eq. (20) with

$$A(t) = f_{\rm QP}^A + (1 - f_{\rm QP}^A)\left[\left(\tfrac{1}{2} - A_e\right)e^{\lambda_1 t} + \tfrac{1}{2}e^{-\lambda_2 t} + A_e\right],$$

$$B(t) = (1 - f_{\rm QP}^A)\left[\left(\tfrac{1}{2} - B_e\right)e^{-\lambda_1 t} - \tfrac{1}{2}e^{-\lambda_2 t} + B_e\right],$$

$$C(t) = 1 - A(t) - B(t). \tag{29}$$

Alternatively, of course, one could use the original Eq. (20) but compare its predictions with renormalized trajectory results where the quasiperiodic fraction has been subtracted out.

Figures 7(a)–7(d) show the three-state statistical model results (dashed line) and trajectory ensemble results (solid line). Notice first that oscillations in the trajectory results are not as severe as the comparable results when only two states were assumed to exist (Fig. 3). It might be argued, however, that if one somehow averages over the oscillations in Fig. 3 that RRKM theory would lead to about the same kind of agreement with the trajectory results as is observed in Fig. 4 for our three-state model. While we have not explicitly made this calculation, we believe this to be the case, with perhaps the occasional discrepancy as we will note in the next paragraph. Adopting the point of view of an experimental kineticist, however, we have still shown the three-state mechanism to be a viable alternative to the two-state one.

A disadvantage of a multistate theory is that no single number characterizes the rate of decay or lifetime of a complex. An arbitrary, but instructive, lifetime definition is the time it takes for the initial relative excitation to decay by a factor of $1/e$, denoted τ_e:

$$\frac{A(\tau_e) - A(t = +\infty)}{A(0) - A(t = +\infty)} = \frac{1}{e}. \tag{30}$$

If just a single exponential decay constant exists, as in the case of the simplest RRKM model, then $\tau_e^{-1} = k$. Otherwise we simply interpret τ_e as a rough measure of the lifetime of excited A complexes. τ_e can be readily determined from our trajectory data and model formulas for $A(t)$. The first two columns of Table III compare the trajectory and three-state model values of τ_e. Table III shows that our model generally provides a reasonable approximation to the trajectory lifetime, predicting between 1.4–2 times the observed trajectory values. We also show in Table III the two individual lifetimes, λ_1^{-1} and λ_2^{-1}, that enter into Eq. (20). As expected, the values of τ_e tend to lie between these two individual lifetimes, with the difference between λ_1^{-1} and λ_2^{-1} not being large enough for the longer lifetime to dominate. We can also estimate τ_e from the two-state trajectory ensemble results and corresponding RRKM model predictions, as given by Eqs. (11) and (15). For $E = 1.25$ we obtain $\tau_e = 20$ from the trajectory results and $\tau_e = 10$ from Eq. (15). This confirms our expectations that the RRKM model can overestimate the rate constant (underestimate τ_e), and that because many initial points lie within the A lobe of the separatrix

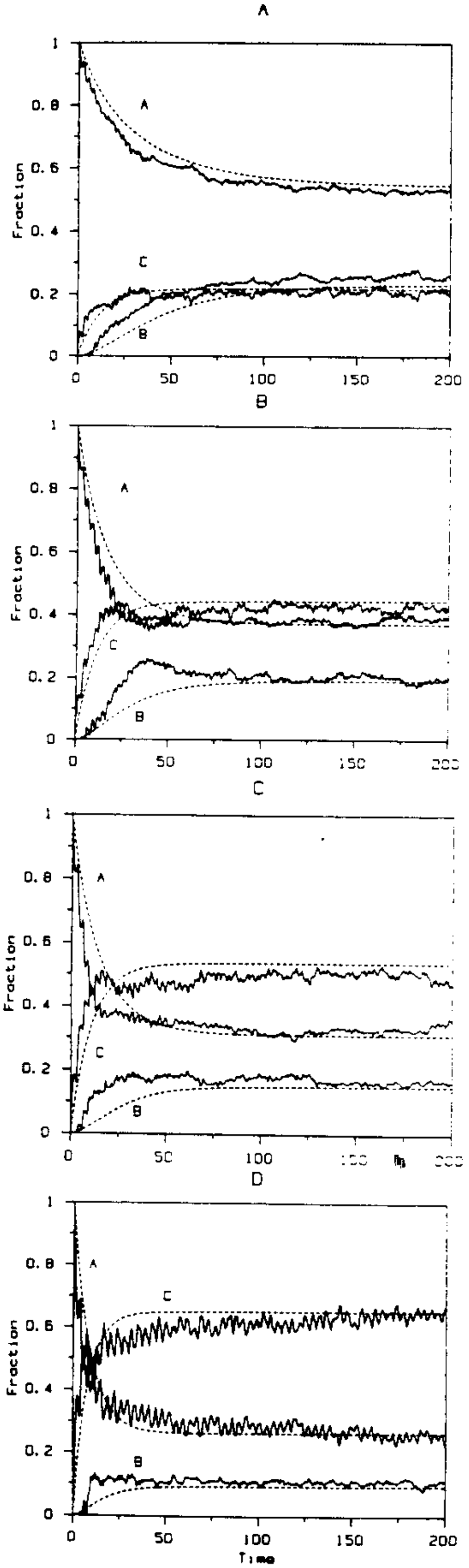

FIG. 7. Fraction of A, B, and C populations as a function of time inferred from propagating 1000 trajectories (solid), along with theoretical predictions based on Eq. (29) with rate constants from Table II. (a) $E = 1.25$, (b) $E = 2$, (c) $E = 3$, and (d) $E = 6$.

TABLE III. Approximate lifetimes τ_e and related data.

E	Trajectory ensemble results	Eq. (30)	$\lambda_1^{-1} = (k_{AC} + 2k_{CA})^{-1}$	$\lambda_2^{-1} = k_{AC}^{-1}$
1.25	21	30	12	39
2.00	11	17	11	21
3.00	7	15	11	17
6.00	6	9	8	10

(even for the two-state model calculation) the two-state trajectory lifetime is closer to the three-state lifetime in Table III than is the RRKM theory prediction. For the higher energies a precise determination of τ_e from the two-state trajectory results is a little more difficult due to the oscillations in Fig. 3. However, Eq. (15), which is roughly the average of the trajectory results, predicts lifetimes consistently 2–2.5 times smaller than those in Table III, which is still consistent with our interpretation above. While the three-state model can thus be slightly more accurate than the two-state RRKM model, it must be said that the differences are more subtle than in the case of van der Waals molecule fragmentation,[2,3] where very dramatic differences were observed. The point of these calculations is really to demonstrate that our three-state model is a useful way to conceptualize isomerization dynamics. Indeed, in the following two paragraphs we wish to explicitly point out how the simple three-state theory does omit certain important dynamical features.

Despite the success of the three-state model in describing certain features of the observed dynamics, inspection of Table III and Fig. 7 shows that the model is not perfect. For example, the A population tends to decrease somewhat more quickly than the statistical prediction. We believe this is probably due to the existence of a direct component[2] in the dynamics: a portion of the A part of phase space tends to leave quickly before it has time to equilibrate, in violation of our statistical assumption. Therefore C, and a little later B, tend to gain more population than the statistical model predicts. Another discrepancy noticeable from Fig. 7 is that the trajectory results do not quite reach the predicted asymptotic values, particularly for the case shown in Fig. 7(c). We believe this to be merely an artifact due to slight errors in our estimates of the relevant areas.

A more serious difficulty in the three-state model is that for some systems it may not be possible to construct an exact separatrix as defined in Sec. III B. This does not prevent the construction of certain approximate separatrices as discussed in Sec. IV, and we still believe that this latter approach will prove to be very useful, especially since it is also much easier. Nonetheless, we were unable to obtain an exact separatrix for $E = 1.02$ because the manifolds of Sec. III B became entwined so quickly that no sensible appearing separatrix structure could be constructed. We note that at this energy, just 2% above the classical barrier height, the standard RRKM theory (appropriately modified for quasiperiodic motion) is adequate for the time range $0 < t < 200$. There may also be cases where intramolecular bottlenecks should be included. Unlike fragmentation, such effects can occur both inside and outside the separatrix. Indeed, even at high energies a correct model of the phase space dynamics would include trapping effects that occur in region C due to resonances such as the 2:1 resonance at $E = 6$.

In summary, we have presented a three state model of isomerization dynamics that, while certainly not a complete description of the dynamics, is at least a plausible and physically appealing analysis that can be better than ordinary RRKM theory, particularly at energies noticeably above the barrier.

IV. APPROXIMATE METHODS FOR DETERMINING THE SEPARATRIX AND ELEMENTARY RATE CONSTANTS

The theory outlined in Sec. III makes statistical assumptions with regard to the behavior of phase points within the two isomer regions A and B, and the intermediate or circulating region C of phase space. However, the construction of the surface that separates these regions, the separatrix surface, involves considerable calculation. For this reason the theory of Sec. III is really of more pedagogical than practical use. It is possible to develop a completely statistical theory of the elementary rate constants, involving no dynamical calculations. This theory is easy to apply and may be thought of as an application of our alternative version of RRKM theory[3,17] to unimolecular isomerization.

In the spirit of the standard RRKM theory one defines the required elementary rate constants to be

$$k_{AC} = \frac{F_{AC}}{N_A} \tag{31}$$

and

$$k_{CA} = \frac{F_{CA}}{N_C}, \tag{32}$$

etc., as required by the problem at hand. F_{AC} is the forward flux of phase points from region A into region C and F_{CA} is the corresponding flux from C into A. Generally, $F_{AC} = F_{CA}$, and we have

$$F_{AC} = \int d\mathbf{p}\, d\mathbf{x}\, \delta(E - H)\dot{S}_A \theta(\dot{S}_A), \tag{33}$$

which is a generalization of Eq. (7) to correspond to the flux across an arbitrary phase space surface

$$S_A(\mathbf{p},\mathbf{x}) = 0 \tag{34}$$

defining region A. $\dot{S}_A$ in Eq. (33) is a time derivative which can be easily evaluated via a Poisson Bracket[3,15] relation. The concentrations N_A and N_C in Eqs. (31) and (32) are defined by expressions such as

$$N_A = \int d\mathbf{p}\, d\mathbf{x}\, \delta(E - H)\theta(-S_A), \tag{35}$$

where it is assumed that if $S_A < 0$ a phase point is inside A.

Equations (31)–(35) could be applied using the "exact" separatrix surface of Sec. III. However these equations can also be used to obtain more approximate, but much easier to evaluate, expressions. For example, the zero-order Hamiltonian in the reactive degree of freedom, Eq. (18), can be used to approximate the separatrix. One then has, for $y < y^{\ddagger}$,

$$S_A = \frac{p_y^2}{2\mu} + V_y - \epsilon_s = 0, \tag{36}$$

approximating the A lobe of the separatrix, along with an analogous expression for $y > y^{\ddagger}$ defining the B lobe. ϵ_s in Eq. (36) is the isomerization barrier height. Insertion of Eq. (36) into Eq. (33) leads, following some standard manipulations,[3,17] to

$$F_{AC} = \int dx \int dy\, \theta(y^{\ddagger} - y) \times \mathrm{Re}\left(\frac{2m}{E - \epsilon_s - V + V_y}\right)^{1/2} \left|\frac{\partial(V - V_y)}{\partial y}\right|. \tag{37}$$

Notice Eq. (37) is a straightforward two-dimensional integral involving the double well potential V_y and the full potential $V(x,y)$, which can be easily evaluated numerically or, if desired, further approximated analytically.[17] In the present application we evaluate Eq. (37) numerically with a trapezoidal rule procedure.

It is also easy to see that

$$N_A = \int dp_y\, dx\, dy\, \theta(y^{\ddagger} - y) \times \mathrm{Re}\left(\frac{2m}{E - p_y^2/2\mu - V}\right)^{1/2} \theta(-S_A) \tag{38}$$

and

$$\begin{aligned} N_C &= 2(N_A^{\ddagger} - N_A) \\ &= 2\int dp_y\, dx\, dy\, \theta(y^{\ddagger} - y)\mathrm{Re}\left(\frac{2m}{E - p_y^2/2\mu - V}\right)^{1/2} \\ &\quad \times [\theta(y^{\ddagger} - y) - \theta(-S_A)], \end{aligned} \tag{39}$$

both of which can also be evaluated numerically. We recommend using a Monte Carlo method for integrals involving more than two integration variables.[3]

Table IV presents the results of a straightforward evaluation of the above equations for the DeLeon–Berne model. Note that, consistent with the notion of a purely statistical theory, it is implicitly assumed here that there is no quasiperiodic motion in the phase space. Table IV shows that the rate constants inferred from the above purely statistical model tend to be about a factor of 2 larger than the exact rate constants determined in Sec. III. The main source of this error is not the omission of the quasiperiodic motion, which would

TABLE IV. Comparison of exact elementary rate constants (upper) with the approximate statistical theory rate constants (lower).

E	k_{AC}	k_{CA}
1.25	0.026[a]	0.028
	0.038[b]	0.060
2.00	0.048	0.020
	0.077	0.040
3.00	0.057	0.016
	0.108	0.033
6.00	0.100	0.014
	0.180	0.030

[a] Exact sparatrix.

[b] Statisical theory (i.e., phase average of zero-order separatrix).

lead to relatively small corrections of factors 1.2–1.4. The error really arises for two other reasons.

First, as we have mentioned elsewhere,[17] the flux in Eq. (37) is an instantaneous value whereas the exact flux of, say, Eq. (25), is calculated via the propagation of trajectories for a nonzero period of time.

The second and most important reason for the factor of two discrepancy in this case is that F_{AC} given by Eq. (37) can be thought of as a phase average of flux out of an approximation to the true phase-dependent separatrix, Eq. (37). To be more explicit, let us reexpress Eq. (33) in terms of canonical action-angle variables[25] (n_x, q_x) for the x degree of freedom instead of the Cartesian variables (x, p_x):

$$F_{AC} = \int dn_x \, dq_x \, dp_y \, dy \delta(E-H) \dot{S}_A \theta(\dot{S}_A). \qquad (40)$$

For simplicity, we adopt the approximation

$$\delta(E-H) \simeq \delta(E-H-W),$$

where the term $H-W$ will be recognized as the zero-order approximation to the full Hamiltonian, Eq. (7). Standard manipulations[3,17] lead to

$$F_{AC}(E) = \frac{1}{2\pi} \int_0^{2\pi} dq_x \, f(q_x, E), \qquad (41)$$

where the function $f(q_x, E)$ is the phase dependent flux out of the zero-order separatrix given by Eq. (36). The explicit form for f is given in the Appendix and involves a simple one-dimensional integral over y. Table V shows the result of evaluating f for a series of vibrational phases q_x with the energy fixed at $E = 1.25$. The result of a full 500 point numerical integration of Eq. (44) in this case is 0.53, which leads to $k_{AC} = 0.038$ in agreement with the entry in Table IV. This result supports the delta function approximation used since the results displayed in Table IV did not involve any approximation to the delta functions. Table V shows that f can vary substantially with q_x. Note that for $q_x = 1.2$, which is very close to the value of q_x such that $x = 0$ from the action-angle formulas in the Appendix, the value of f is about 0.2, which is in good agreement with the exact separatrix result displayed in Table II. Had we somehow used the exact phase-dependent separatrix in the calculation of f, we would have found f to be independent of phase, as discussed in Sec. III B. However, by using a phase-independent approximation to the separatrix, f turns out to be phase dependent.

One could, of course, define a better zero-order separatrix that depended on the phase and achieve better agreement with the exact rate constant results of Sec. III C. It is amusing to note, however, that the approximate rate constants of Table IV, when coupled with the three-state model population equations (32), yield better agreement with the trajectory results. Figure 8 illustrates this for $E = 2$ and one should keep in mind that similar results obtain for the other energies not shown. In particular, note that the population $B(t)$ is much better described with the phase-averaged, zero-order rate constants, in comparison with Fig. 7(b). The reason for this result is that the factor of 2 overestimate of the rate constant by our purely statistical theory compensates for omission of the "direct component" to the dynamics discussed in Sec. III C. In a sense this result is encouraging too, because the success of a statistical theory often relies on cancellation of errors.

TABLE V. Phase dependence of the zero-order separatrix flux for $E = 1.25$.

q_x	$f(q_x, E)$
0	0.84
0.4	0.75
0.8	0.51
1.2	0.18
1.6	0.16
2.0	0.46
2.4	0.68
2.8	0.81
3.2	0.84

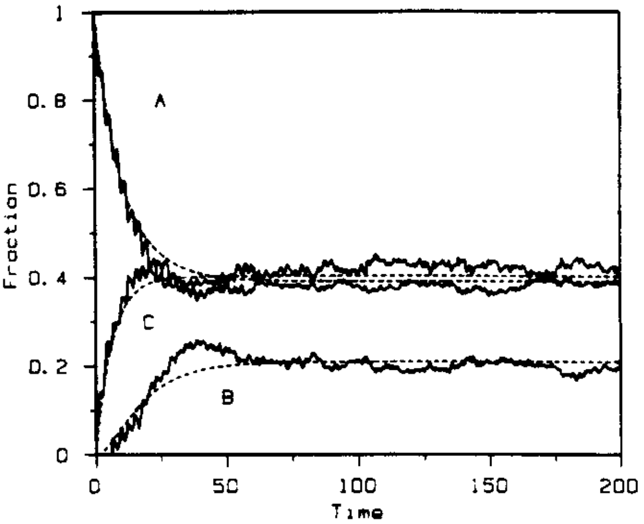

FIG. 8. Fraction of A, B, and C populations for $E = 2$. The solid curves are the trajectory results and the dashed curves are from Eq. (29) with rate constants from Table V, based on the zero-order separatrix and simple methods of Sec. IV.

V. DISCUSSION

We have presented a three-state model for isomerization reaction dynamics. The methods for obtaining the required elementary rate constants in the model involve applications and extensions of our previous work on phase space bottlenecks.[2,3,17] The results of the model using the exact (Sec. III) and approximate (Sec. IV) divisions of phase space show that a three-state mechanism is a plausible alternative to the two-state RRKM model. As emphasized in Sec. IV, we have definitely not included all possible dynamical effects, and future work could be directed towards developing a theory which accounted for these omitted effects. However, we believe the three-state model alone will be useful, not only for semiquantiative calculations, but as a conceptual foundation for future work.

It will be of interest to apply the ideas presented in this paper to other isomerization problems. In some cases, as noted in Sec. III B, it may not be possible to obtain exact separatrices. However the zero-order separatrix, as defined in Sec. IV, or perhaps better approximations that may include other variables aside from the reaction coordinate and its momentum, can still be used. Since much or all of the relevant intramolecular dynamics corresponding to an A or B isomer occurs within the region defined by the approximate separatrix, we believe that this method will yield interesting and useful results. Extensions to many degrees of freedom problems, as also discussed in Ref. 3, are quite feasible with this approach since only integrals are required.

The present paper has been concerned solely with the isomerization of isolated molecules. The conventional thermal gas phase rate constants can, of course, be obtained via Boltzman–weighted integration over the microcanonical rate constants.[5] A more interesting extension of our work would be to the study of isomerization dynamics in liquids. The existence of frictional and fluctuating forces on the reactant, due to the solvent, will undoubtedly lead to a breakdown of some or most of the isolated molecule phase space structure. However, the low friction limit of the rate of isomerization is a subject of current experimental interest,[26] and it is in this limit that the remnants of the isolated molecule phase space, including phase space bottlenecks, may be important. We plan to investigate such possibilities in future work.

ACKNOWLEDGMENTS

This research was supported by grants from the NSF and AFOSR. We also acknowledge helpful comments by M. J. Davis.

APPENDIX

In this Appendix we: (i) introduce canonical action-angle variables[25] for the x degree of freedom of the DeLeon–Berne system, (ii) derive the explicit form for the phase-dependent flux out of the zero-order separatrix $f(q_x,E)$.

Let standard Morse oscillator action-angle variables[25] (n_x,q_x) replace the Cartesian variables (p_x,x). In terms of these new canonical variables the full Hamiltonian of Eqs. (7) and (8) may be written as

$$H = H_y(p_y,y,n_x,q_x) + H_x(n_x), \tag{A1}$$

where

$$H_y = \frac{p_y^2}{2\mu} + 4y^2(y^2-1)(2-e^{-2\lambda x(n_x,q_x)}) + \epsilon_s \tag{A2}$$

and (with $\hbar = 1$ for simplicity)

$$H_x = (n_x + \tfrac{1}{2})\omega_x^0 - (n_x + \tfrac{1}{2})^2\omega_x^{02}/4D_x. \tag{A3}$$

The relation between the old position variable and the new action and angle variables required above is

$$x = \ln\{c^{-2}[1-(1-c^2)^{1/2}\cos q_x]\}/\lambda, \tag{A4}$$

where

$$c = 1-(2n_x+1)\lambda/(2mD_x)^{1/2} \tag{A5}$$

and D_x, λ, m and

$$\omega_x^0 = (2D_x\lambda^2/m)^{1/2} \tag{A6}$$

characterize the x degree of freedom Morse oscillator.

We now derive an explicit form for the phase-dependent flux out of the zero-order separatrix. The full phase-averaged flux, is from Eq. (40),

$$F_{AC} = \int dn_x\, dq_x\, dp_y\, dy\, \theta(y^{*}-y)\theta(p_y)\delta(h_y-\epsilon_s) \times \frac{p_y}{\mu}\left|\frac{\partial(V-V_y)}{\partial y}\right|, \tag{A7}$$

where the first step function is used to continue the integration to the A part of the separatrix and the second step function, as well as the term in absolute value signs, arises from evaluation of the time derivative of the separatrix and manipulations similar to those in our previous work. The condition $h_y = \epsilon_s$ enforced by one of the δ functions in Eq. (A7) is, of course, the zero-order separatrix condition, where h_y is given by Eq. (18) in the text. Evaluating the integral over p_y by writing

$$\delta(h_y-\epsilon_s) = \frac{\mu}{p_{yk}}\delta(p_y-p_{yk}),$$

where $p_{yk} = +[2\mu(\epsilon_s-V_y)]^{1/2}$, and then evaluating the integral over n_x by approximating

$$\delta(E-\epsilon_s-H_x-W) \approx \delta(E-\epsilon_s-H_x),$$

and using the identity

$$\delta(E-\epsilon_s-H_x) = \delta(n_x-n_{xk})/\omega_x(n_{xk}),$$

leads finally to Eq. (41) where

$$f(q_x,E) = \frac{\pi}{2}\int_{-1}^{0} dy \left|\frac{\partial(V-V_y)}{\partial y}\right| \frac{1}{\omega_x(n_{xk})}. \tag{A8}$$

In Eq. (A8) one has

$$n_{xk} = \frac{2D_x}{\omega_x^0}\{1-[1-(E-\epsilon_s)/D_x]^{1/2}\} \tag{A9}$$

for the action n_{xk}. The value of x, which enters Eq. (A8) through the full potential $V(x,y)$ is determined from Eq. (A4) with the action given by Eq. (A9).

[1] M. J. Davis, J. Chem. Phys. **83**, 1016 (1985).

[2] M. J. Davis and S. K. Gray, J. Chem. Phys. **84**, 5389 (1986).

[3] S. K. Gray, S. A. Rice, and M. J. Davis, J. Phys. Chem. **90**, 3470 (1986).

[4] N. DeLeon and B. J. Berne, J. Chem. Phys. **75**, 3495 (1981).

[5] See, for example, W. Forst, *Theory of Unimolecular Reactions* (Academic, New York, 1973).

[6] D. Chandler, J. Chem. Phys. **68**, 2959 (1978).

[7] See, for example, B. A. Waite and W. H. Miller, J. Chem. Phys. **73**, 3713 (1980).

[8] See, for example, P. Pechukas, in *Dynamics of Molecular Collisions, Part B*, edited by W. H. Miller (Plenum, New York, 1976), p. 269.

[9] R. J. Wolf and W. L. Hase, J. Chem. Phys. **73**, 3779 (1980).

[10] W. L. Hase, D. J. Duchovic, K. N. Swany, and R. J. Wolf, J. Chem. Phys. **80**, 714 (1984).

[11] R. A. Marcus, W. L. Hase, and K. N. Swany, J. Phys. Chem. **88**, 6717 (1984).

[12] D. B. Borchardt and S. H. Bauer, J. Chem. Phys. **85**, 4980 (1986).

[13] R. S. Mackay, J. D. Meiss, and I. C. Percival, Physica D **13**, 55 (1984).

[14] D. Bensimon and L. P. Kadanoff, Physica D **13**, 82 (1984).

[15] A. J. Lichtenberg and M. A. Lieberman, *Regular and Stochastic Motion* (Springer, New York, 1983).

[16] S. K. Gray, S. A. Rice, and D. W. Noid, J. Phys. Chem. **84**, 5389 (1986).

[17] S. K. Gray and S. A. Rice, Faraday Discuss Chem. Soc. **82**, paper 15 (1986).

[18] T. Uzer and J. T. Hynes, Chem. Phys. Lett. **113**, 483 (1985).

[19] C. Jaffe and W. P. Reinhardt, J. Chem. Phys. **77**, 5191 (1982); R. B. Shirts and W. P. Reinhardt, *ibid.* **77**, 5205 (1982).

[20] See, for example, M. Braun, *Differential Equations and Their Applications: An Introduction to Applied Mathematics* (Springer, New York, 1978).

[21] S. H. Northrup and J. T. Hynes, J. Chem. Phys. 73, 2700 (1980); R. F. Grote and J. T. Hynes, *ibid.* 73, 2715 (1980).

[22] A. F. Vorter and J. D. Doll, J. Chem. Phys. **82**, 80 (1983).

[23] S. R. Channon and J. Lebowitz, Ann. N.Y. Acad. Sci. **357**, 108 (1980).

[24] See, for example, I. Percival and D. Richards *Introduction to Dynamics* (Cambridge University, Ithaca, 1982).

[25] C. C. Rankin and W. H. Miller, J. Chem. Phys. **55**, 3150 (1971).

[26] See, for example, S. H. Courtney and G. R. Fleming, Chem. Phys. Lett. **103**, 443 (1984), and references therein.